UNIVERSITY OF SOUTHAMPTON

Slitted leading-edge profiles for the reduction of broadband interaction noise

by

Marine Cannard

A thesis submitted in fulfillment of the requirements
for the degree of Doctor of Philosophy

in the
Faculty of Engineering and Physical Sciences
Institute of Sound and Vibration Research - ISVR

March 2020

This thesis I dedicate
to my loving parents and my brother

UNIVERSITY OF SOUTHAMPTON

ABSTRACT

FACULTY OF ENGINEERING AND PHYSICAL SCIENCES
INSTITUTE OF SOUND AND VIBRATION RESEARCH - ISVR

Doctor of Philosophy

SLITTED LEADING-EDGE PROFILES FOR THE REDUCTION OF BROADBAND INTERACTION NOISE

by Marine Cannard

Aerofoil Turbulence Interaction (ATI) noise is an inviscid phenomenon generated by the impingement of turbulent flows onto the leading-edge of an aerofoil. This thesis deals with a novel leading-edge serration geometry, composed of narrow slits, to reduce ATI noise. These profiles have been recently found to provide significantly better noise reductions than conventional leading edge geometries. A numerical and analytic investigation is performed into the mechanism and performance of its noise reduction. The far-field radiation is shown to be influenced by a system of induced vortices affecting the distribution of sources on the flat-plate and by destructive interference between the two sources generated at both ends of the slit. A simple two-source model is developed to predict the far-field noise reduction obtained and compared to straight leading-edge aerofoils. A numerical parametric study is also performed, aimed at providing greater insight and understanding into the sensitivity of noise reductions to variations in the slit geometrical parameters. In particular, this thesis investigates the effect on source strength distribution to variations in slit length, width and wavelength and elucidates the reason for this effect on source distribution in terms of the fundamental vortex dynamics. This thesis concludes with an extensive experimental study into the effect on control performance due to variation in slit geometry, aimed at validating the numerical findings and providing guidelines for optimising slitted leading-edge profiles.

Contents

List of Figures

List of Tables

Nomenclature

c	Sound speed
e_t	Total energy per unit mass
f	Frequency
f^*	Normalized frequency ($f^* = fL/c$)
G	Green's function
h	Slit height
i	Imaginary unit
J	Jacobian
k	Wavenumber
L_z	Aerofoil span
M	Free-stream Mach number
p	Fluctuating pressure
p_∞	Free-stream pressure
Pr	Prandtl number
Q	Q-criterion
Re	Reynolds number
S	Sponge zone forcing term
S_{pp}	Acoustic pressure PSD
S_{qq}	Source strength
t	Time
t^*	Normalized time ($t^* = tc/L$)
T	Period
U_∞	Free-stream velocity
(u, v, w)	Streamwise, vertical and spanwise velocities
w	Slit width
x_0	Initial position of the vortex
x_{LE}	Location of the flat-plate leading-edge
(x_1, x_2, x_3)	Cartesian coordinates
ΔPWL	Sound power reduction
ϵ	Vortex strength parameter
λ	Slit wavelength
Λ	Eddy size
μ	Dynamic viscosity (sponge zone coefficient)
$\psi(\mathbf{x})$	Shape function of the eddy
$\Phi_{vv}(\omega)$	Power spectral density of the transverse velocity fluctuation

ρ	Free-stream density
ω	Angular frequency
σ	Vortex size parameter
τ	Retarded time
ξ, η, ζ	Generalized coordinates

Acronyms

ACARE	Advisory Council for Aviation Research in Europe
AGI	Aerofoil Gust Interaction
ATI	Aerofoil Turbulence Interaction
CAA	Computational Aeroacoustics
CFD	Computational Fluid Dynamics
FWH	Ffowcs-Williams Hawkings
LE	Leading Edge
LE	Large Eddy Simulation
NACA	National Advisory Committee for Aeronautics
OASPL	Overall sound pressure level
OGV	Outlet Guide Vane
PWL	Sound Power Level
RANS	Reynolds-averaged Navier–Stokes
SLE	Straight Leading Edge
SPL	Sound Pressure Level
TE	Trailing Edge

Declaration of Authorship

I, Marine Cannard, declare that this thesis entitled *Slitted leading-edge profiles for the reduction of broadband interaction noise* and the work presented in it are my own and has been generated by me as the result of my own original research.

I confirm that:

1. This work was done wholly or mainly while in candidature for a research degree at this University;
2. Where any part of this thesis has previously been submitted for a degree or any other qualification at this University or any other institution, this has been clearly stated;
3. Where I have consulted the published work of others, this is always clearly attributed;
4. Where I have quoted from the work of others, the source is always given. With the exception of such quotations, this thesis is entirely my own work;
5. I have acknowledged all main sources of help;
6. Where the thesis is based on work done by myself jointly with others, I have made clear exactly what was done by others and what I have contributed myself;
7. Parts of this work have been published and the list has been indicated in Chapter 1 of the thesis.

Signed:

Date:

Acknowledgements

This thesis would not have been written without a number of people to whom I am deeply thankful.

First of all and foremost, I must express my profound gratitude towards my supervisor Pr. Phillip Joseph who constantly inspired, supported and guided me throughout my scientific journey. His knowledgeable experience has taught me how to carry scientific research in the best way I could have ever imagined. On a more personal level, his constant optimism and his humane personality made our humorous but profound discussions the highlights of my days during these last few years. I also want to acknowledge my supervisor Jae Wook Kim who made it possible for me to realise this PhD following his expertise and guidance on numerical simulations.

I am deeply indebted to Chaitanya Paruchuri, with whom I closely collaborated during this project, for both his intellectual contribution and personal support along this journey. I must also thank Jacob Turner for his invaluable help on setting up numerical simulations when I needed advice during the difficult times of the PhD.

I also extend my gratitude to all members of the ISVR: fellow PhD candidates for our valuable discussions and relaxing coffee breaks, all lecturers and professors for their scientific wisdom, without forgetting the administrative officers without whom the organisation of the Institute would simply not exist!

Additionally, I would like to express my acknowledgements to Rolls-Royce Plc and EPSRC for the financial support.

Last but not least, I would like to express my deepest gratitude to my parents for giving me the direction in my education. This thesis would not have been possible without their warm love, continued patience, and endless support. I also hold my brother dearly in my heart for always cheering me up and encouraging me. I am extremely grateful to all my friends and the Yoga community for the moral support and our precious moments over the last few years.

Chapter 1

Introduction

1.1 Motivation

Noise pollution represents a key environmental concern, but also a matter of public health for citizens living in airport areas. According to reports from the ICAO, air traffic increased by approximately 6.4% compared to 2014 [5]. Reducing aircraft noise has therefore become a significant political issue, with the creation of European directives establishing regulations concerning the limitation of noise emission in airports. In 2000, ACARE set as the priority target a 50% reduction in aircraft perceived noise emission by 2020, that should reach 65% by 2050 [1]

Aircraft noise emissions originate from the jet engine or from the airframe interacting with the flow, such as landing-gears (Fig. 1.1). As illustrated in Fig. 1.2, turbofan engine noise is a combination of jet noise, fan noise and combustion & turbine noise. Fan noise is found to produce half of the total noise at take-off and landing, due to increases in the bypass ratio over the last decades that led to a significant decrease in jet noise.

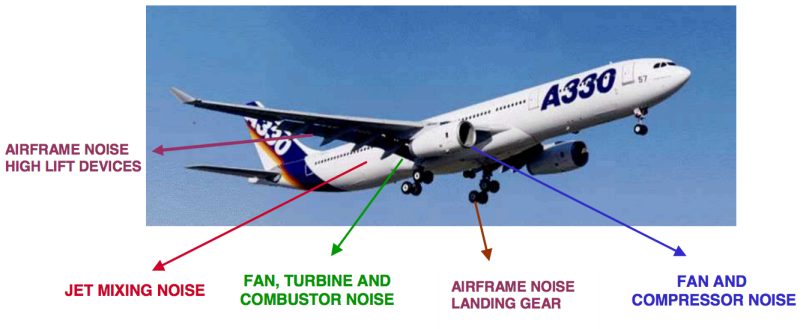

FIGURE 1.1: Aircraft noise sources [1]

[1] http://www.acare4europe.com/sria/flightpath-2050-goals/protecting-environment-and-energy-supply-0

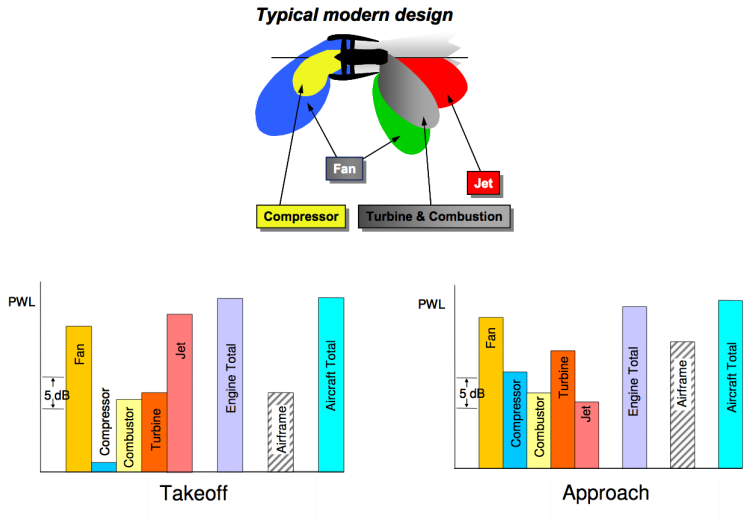

FIGURE 1.2: Engine noise sources and relative power levels of aircraft noise sources at takeoff and approach [1]

Fan noise can itself be decomposed into tonal noise and broadband noise. The tonal component is a harmonic contribution, generated by periodic fluctuations on the blades of the rotor/stator and is related to the blade pass frequency and its harmonics. On the other hand, the broadband component of fan noise displays a wide spectral bandwidth and is generally attributed to the turbulent behaviour of the flow, originating from the rotor wakes or instabilities in the boundary layer. Different mechanisms are known to produce broadband noise: rotor/stator interaction noise, rotor-boundary layer self noise and the rotor-wake guide vanes interaction noise.

1.2 Prediction of Aerofoil-Turbulence Interaction (ATI) noise

This thesis focuses on the reduction of aerofoil-turbulence (ATI) interaction noise, which is an inviscid phenomenon generated by the impingement of turbulent flows onto the leading-edge on an aerofoil. ATI noise occurs during the interaction of the turbulent wakes from the rotor with the outlet guide vanes (OGV's) and is believed to be the dominant broadband noise source on modern turbofan engines.

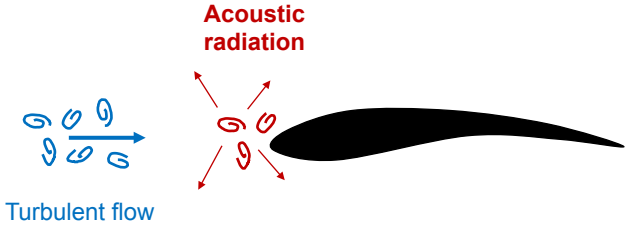

FIGURE 1.3: Illustration of aerofoil-turbulence interaction (ATI) noise

1.2.1 Analytical and experimental approaches

Isolated aerofoils

The first studies related to aerofoil-interaction noise date back to the 1920's and essentially focus on the determination of the aerodynamic response of aerofoils to flow disturbances. These findings represent an important step in the development of aeroacoustics prediction models, as formulations of the unsteady loading on the aerofoil surface directly provide expressions for the acoustic sources that will radiate to the far-field.

Following the work of Von Karman & Sears [6] on unsteady aerofoil theory, Sears proposed in 1941 a formulation for calculating the unsteady lift induced by the impingement of a harmonic vortical gust on a flat plate with no camber and zero thickness [7]. The theory is, however, limited to incompressible flows and two-dimensional (2D) parallel gusts only (no wavenumber in the aerofoil spanwise direction), as was pointed out by Paterson & Amiet [8].

Effects of compressibility and three-dimensionality were later taken into account by Adamczyk [9] in 1974, who developed approximate expressions for the compressible aerodynamic response of an infinite swept flat-plate due to an incoming three-dimensional gust. This formulation was derived by employing Graham's similarity rules, in order to express the 3D compressible case in terms of the formulations derived for either the 2D compressible case and the three-dimensional (3D) incompressible case. Adamczyk's formulation further accounts for the trailing-edge backscattering by adding a second component to the response function, using Landahl's iteration procedure.

Generalizing the work of Adamczyk, Amiet [10] developed in 1975 a compressible aeroacoustic prediction model for a 2D flat-plate encountering 3D incoming turbulence. This model predicts the fluctuating pressure along the flat-plate and uses Curle's theory [11] to determine the far-field radiated noise. In the frequency domain, the response is either determined by Adamczyk's approximation (high-frequencies) or Amiet's formulation (low frequencies). Offering a complete analytical approach for the interaction of a turbulent flow with a flat-plate, Amiet's model constitute an accurate validation case widely used by researchers. However, as in all the studies previously mentioned, the effects of aerofoil geometry are not accounted for.

Amiet's model has been extended by many researchers to take into account the effects of aerofoil geometry on the radiated noise. Kucukcoskun et al [12] derived a semi-analytical formulation taking into account geometrical near-field corrections and spanwise variations of the incoming flow. Moreau et al [13] proposed semi-empirical corrections to Amiet's model to account for the effects of thickness and camber, using a projection of sources calculated for a flat-plate onto the real aerofoil profile. Good agreement was obtained with experimental measurements. More recently, Santana et al [14] showed that Amiet's model overestimates interaction noise at frequencies for which the aerofoil chord is larger than the gust wavelength (compact source). The author proposed semi-empirical corrections to compensate for the over-prediction.

In order to take into account effects of real aerofoil geometry more precisely, other methods have been developed, requiring an expansion of the governing equations to the second order. To this aim, Goldstein and Atassi [15] used the Rapid Distortion Theory to calculate the radiation of a body of any geometrical shape under vortical or entropic perturbation. This method showed that the incoming gusts is distorted by the mean flow streamlines around the aeorofoil, mostly affecting the radiated noise at high frequencies.

Cascade of aerofoils

Numerous studies have been undertaken in the last few decades to understand the noise generated by the interaction of vortical velocity perturbations on a cascade of aerofoils. One possible approach consists in using the formulations of Amiet or Adamczyk previously mentioned to evaluate the unsteady loading of an isolated aerofoil and adding together the different responses for each aerofoil of the cascade. Glegg [16] applied this method to predict the noise generated by the interaction of the rotor wake with the stator, using the formulation developed by Goldstein for a propagation in an annular duct instead of a free-field propagation. These approaches account for the phase difference between the responses of each aerofoil of the cascade, but neglects the interference effects produced by the influence of neighbouring aerofoils on each other. This hypothesis can be justified when the inter-blade spacing is sufficiently large in comparison to the acoustic wavelength, but cannot generally be applied in a typical turbofan engine as the vanes are closely spaced. Atassi & Hamad [17] showed that these interference effects can significantly affect the jump in aerodynamic pressure and therefore the radiated noise.

To overcome these limitations, semi-analytical models known as "lifting surface methods" have been developed, expressing the unsteady loading on the aerofoil by an integral equation. Considering the blades as an unsteady distribution of pressure doublets, Kaji & Okazaki [18] studied the transmission and reflection of acoustic waves by a blade row using an acceleration potential method. A relation to the azimuthal orders of the modes propagating in the duct is also provided by this method. Using the mathematical theory developed by Lane and Friedman [19], Whitehead [20] [21] proposed a model determining the acoustic field generated by a cascade of flat plates undergoing different perturbations in a two-dimensional subsonic unsteady flow. The force and moment on the blades, wake shed from the trailing edge and outgoing acoustic waves can be calculated from this model, but some limitations are encountered due to numerical difficulties around the cut-off frequencies as reported by Whitehead. This work was extended to three-dimensional gusts by Goldstein. Using a different approach, Smith [22] considered the blades as a row of vortices of force equal to the jump of axial velocity between the upstream and downstream of the cascade. The vorticity distribution can then directly be linked to the pressure jump on the blades. The upstream and downstream acoustic pressures are numerically evaluated by computation of this source term. This theory was implemented in a FORTRAN code, LINSUB, by Whitehead [21] and extended by Cheong et al [23] by considering the periodicity of the cascade response function in the transverse turbulence wavenumber.

Another series of studies have expressed the problem using a Wiener-Hopf approach, as Mani & Horvay [24] who derived an approximate analytic solution for the reflection and transmission of acoustic waves in a cascade of arbitrary spaced flat plates. The blades were treated as semi-infinite, presenting either a leading-edge or a trailing-edge, to solve the two problems separately.

The model predictions are in good agreement with the work of Kaji & Okazaki [18], with a decreased accuracy above cut-off frequencies when the coupling between the leading and trailing edge can no longer be neglected [25]. Koch [25] developed a model accounting for this coupling inside the duct and derived an analytic formulation of the unsteady loading. Requiring a precise evaluation of the Wiener-Hopf coefficients, calculations are rather long and difficult, as reported by Koch. Extending the work of Koch, Peake [26] derived a simpler mathematical expression of the unsteady loading by considering successively the diffraction of the incident perturbation and of the inter-blade acoustic modes propagating upstream by a semi-infinite flat-plate with no trailing-edge, and the diffraction of the inter-blade acoustic modes propagating downstream by a semi-infinite flat-plate with no leading-edge. Finally, Glegg [27] provided an expression for the harmonic response function of a three-dimensional rectilinear cascade of finite blades excited by a three-dimensional gust which was later used by Hanson & Horan [28] to develop a model for the complete three-dimensional turbulence-cascade interaction noise.

The methods presented above all consider the blades as flat-plate aerofoils. Effects of angle of attack, camber and thickness were investigated by Peake & Kerschen [29], then by Evers & Peake [30] as detailed in Section 2.2.

1.2.2 Computational approaches

Requirements and methods

Rapid increases in computational power over the last decade gave a new dimension to numerical methods, by allowing the simulation of more and more complex problems and offering the possibility of breaking free from assumptions required in analytical models. However, despite the efficiency and accuracy of existing numerical methods, accurate aeroacoustic simulations are challenging because of the requirements needed in comparison to CFD methods to provide accurate results [31]. Far-field predictions imply a larger computational domain, in combination with finer meshes in order to resolve the highest frequencies, as well as the small scales of incoming turbulence. Furthermore, in view of the small acoustic velocity fluctuations in comparison to the mean-flow speed, a higher control of computational errors is also required in order to prevent a masking of the desired acoustic field by spurious waves arising from these computational errors [31]. Additional efforts are therefore required in the development of adapted low-dispersion and low-dissipation schemes, combined with specific non-reflecting boundary conditions.

The requirements previously mentioned make aeroacoustic simulations very costly in terms of computational resources. Direct Numerical Simulations (DNS) are therefore not suitable for studying aerofoil-interaction noise [32] and Large Eddy Simulations (LES), which are much cheaper, still remain too costly for more complex geometries [33]. Instead, a widespread approach consists in dividing the calculation into two stages: the first stage is dedicated to the unsteady flow simulation where sound sources are effectively determined, followed by a second stage where these sources are propagated to compute the radiated far-field noise [31]. The propagation stage is generally conducted by using an acoustic analogy (Lighhill, FWH or Kirchhoff/Curle) or by including the source terms in the Linearized Euler Equations (LEE). The determination of

acoustic sources is on the other hand more troublesome and can be realised in two different manners:

- The unsteady flow can be computed by DNS/LES/RANS simulations and the results implemented in the second calculation as an input
- An alternative approach consists in using stochastic methods to synthesise a turbulent field. In these methods, a synthetic turbulent velocity field is generated and injected in the domain to be directly used in the governing equations (full Euler or LEE for instance) or acoustic analogies. This approach is considerably less costly than running a DNS/LES/RANS and produce accurate results if the velocity field contains the most relevant features of the turbulence for the study considered [34]. The different synthetic turbulence generation methods available will be discussed further below. However, it is important to note that the synthetic method cannot predict the turbulence but only represent it in the calculation.

Single aerofoil with incoming harmonic gust

The first numerical studies on interaction noise were conducted by considering the simpler case of a single aerofoil interacting with a single frequency vortical gust at normal incidence.

Scott & Atassi [35] [36] developed a finite difference linearized Euler solver to compute the acoustic radiation from an aerofoil in a three-dimensional gust in the frequency domain. The velocity field is expressed as a sum due to a mean flow velocity and a perturbed velocity, itself decomposed into an irrotational part and a prescribed rotational part. As the prescribed vortical velocity is divergence-free, no pressure fluctuations are produced. Good results were obtained in the near-field but numerical dispersion and sensitivity to non-reflecting boundary conditions caused the authors to couple the solver to a Kirchhoff integral method to predict the radiated far-field noise [37]. This numerical method spearheaded the development of the NASA code GUST3D.

Later, Lockard and Morris [38] [39] studied the effect of gust frequency and aerofoil thickness on interaction noise, including nonlinear effects by solving the two-dimensional Navier-Stokes (NS) equations. The vortical gust is directly generated inside the computational domain once the mean flow has reached steady-state. Results are in good agreement with the work of Atassi et al [37]. However, spurious solutions are produced at the boundary in the nonlinear inviscid case and the viscous case faces some difficulties with instabilities in the gust and wake.

Hixon et al [40] solved the 2D nonlinear Euler equations in the time domain using the NASA BASS code to study the effect of a single-frequency 2D vortical gust convected past a Joukowski aerofoil for different gust amplitudes and frequencies. The flow is initialized to the mean flow and the vortical gust superposed at the inflow boundary. The results obtained with nonlinear flows were in good agreement with the benchmark results from the linear solver GUST3D, although some reflections were observed at high frequencies from the boundaries. These conclusions were

also reported by Golubev et al [41] [42] who studied the nonlinear inviscid gust-aerofoil interaction to quantify nonlinear effects. The author concluded that a new formulation was necessary for the far-field boundary conditions to avoid non-reflective solutions.

Stochastic methods for turbulent velocity field

The AGI studies previously presented allowed the derivation of benchmark validation cases for numerical methods but remain limited to single-frequency analyses. In order to study broadband noise generated by aerofoil-turbulence interaction, an incoming turbulent velocity field reproducing some experimental or numerical spectral data needs to be introduced. As mentioned above, several approaches can be considered: predicting all turbulence length scales from the governing equations by running an initial computation using DNS/LES/RANS, or synthesizing a turbulent velocity field with the use of stochastic generation methods. Considerably less expensive in computational resources and offering promising possibilities of accurate predictions, the second approach is usually considered. The development of these challenging methods is under constant improvement in order to achieve a more realistic representation of the turbulent velocity field. They can be classified into several categories according to the way they generate the velocity field.

Fourier methods

The original approach, developed by Kraichnan [43] in the field of particle diffusion, considers the turbulent field as a discrete sum of Fourier modes. The decomposition is illustrated in Eq. 1.1, with N number of modes. The amplitude of each mode $\mathbf{a}_n$ and $\mathbf{b}_n$ are chosen to match a specific Gaussian energy spectrum and the resulting velocity field is divergence-free. The idea was taken up by Karweit et al [44] for applications in aeroacoustics and enhanced by many researchers, such as Bailly and Juve [45] and Billson et al [46] [47] to study jet noise. Clair et al [48] used a similar technique to develop a numerical method for predicting the interaction noise between a flat plate and a velocity turbulent field. The perturbed velocity is introduced through an appropriate boundary condition and synthetized based on a desired wavenumber spectrum. Very good agreement with Amiet's analytical model was obtained. Gill [49] synthetized a 2D turbulence using the Fourier decomposition method to study the effect of aerofoil thickness on interaction noise with an LEE solver. Predictions showed a noise reduction for increased aerofoil thickness at high frequencies, dependent on the Mach number. The author however highlights the limits of the Fourier decomposition method when modelling more complex turbulent flows.

$$\mathbf{u}(\mathbf{x},t) = \sum_{n=1}^{N} [\mathbf{a}_n \cos(\mathbf{k}_n.\mathbf{x} + \omega_n t) + \mathbf{b}_n \sin(\mathbf{k}_n.\mathbf{x} + \omega_n t)] \tag{1.1}$$

Synthetic Eddy Methods

A second approach, known as the Synthetic Eddy Method (SEM), was developed by Jarrin et al [50] for Large Eddy Simulations. In this method, the turbulence is considered as a superposition of coherent structures defined by a shape function that attempts to reproduce some statistical behaviour of the turbulence, such as its temporal and spatial characteristics. The resulting velocity field is determined from the sum of the contribution of these synthetically generated eddies and injected as a boundary condition on the inlet plane. Although the generated velocity field was not divergence-free, this novel approach was successful in producing fully developed

turbulence for the cases investigated. The SEM was later taken up by Sescu & Hixon [51] to develop a synthetic turbulence generation method for aeroacoustics, with the main focus to reduce the level of spurious noise induced. The velocity field is derived from a vector potential that encompasses the eddies shape functions to satisfy the divergence-free condition. Numerical results obtained for broadband aeroacoustic stator simulations were compared with an experimental test case of decaying isotropic turbulence and good agreement was obtained, as well as a low level of spurious noise at the inflow boundary and inside the domain. Additionally, the authors demonstrated the importance of synchronizing the turbulent convection velocity with the mean flow velocity to lower the production of spurious acoustic disturbances. A general description of the method developed by Sescu is available in Eq. 1.2, with $\boldsymbol{\psi}$ being the vector velocity potential. $\mathbf{x}_n^0$ and t^0 represent the spatial and temporal location of the centre of the n^{th} eddy. λ_b and τ_b are respectively the turbulence length and time scales, and A_{inflow} is the area of the inflow boundary.

$$\begin{cases} \mathbf{u}(\mathbf{x},t) = \nabla \times \boldsymbol{\psi}(\mathbf{x},t) \\ \boldsymbol{\psi}(\mathbf{x},t) = \sqrt{\frac{A_{inflow}}{N}} \sum_{n=1}^{N} \epsilon_n \boldsymbol{\psi}_n \left(\frac{\mathbf{x}-\mathbf{x}_n^0}{\lambda_b}, \frac{t-t_n^0}{\tau_b} \right) \end{cases} \tag{1.2}$$

Previous improvements on the SEM were made by Kim & Haeri [52] who introduced a set of parameters for a more complete characterisation of the eddies. A Genetic Algorithm was used to optimize the parametrization of these new coefficients in order to reproduce a von Karman velocity spectra. The resulting turbulent velocity field is three-dimensional. Furthermore, the level of spurious noise was further reduced by smoothly injecting the velocity field inside the computational domain through the use of a sponge layer. The authors applied this new turbulence generation method to the simulation of aerofoil-turbulence interaction noise and obtained a reasonably good agreement with experimental data and the analytical solution provided by Amiet's model.

Random Particle Mesh methods

Another category of methods known as the Random Particle-Mesh (RPM) method, was developed by Ewert and Schroder [53] for the study of slat noise and trailing edge noise. The RPM method consists of injecting particles at each node of the discretized streamlines of the mean flow. The velocity field attributed to the particles is derived from a stream function generated by filtering white noise and is divergence-free. Dieste & Gabard [54] [55] used the RPM method to study interaction noise induced by the impingement of a turbulent flow on a flat plate. The results were in good agreement with Amiet's model. Dieste & Gabard also included a temporal evolution in the synthetized turbulence and compared the results with predictions of the radiated noise obtained in the case of frozen turbulence. They concluded that there was a very limited influence on the radiated noise by modelling the time correlation, which validate the hypothesis of frozen turbulence for the flat plate case. The general approach of the RPM method is illustrated by Eq. 1.3, where $\mathscr{G}$, $\mathscr{U}$ and ψ respectively represents the filter given by a Gaussian distribution, a spatial white noise and the stream function and is given by

$$\begin{cases} \mathbf{u}(\mathbf{x},t) = \nabla \times \boldsymbol{\psi}(\mathbf{x},t) \\ \psi_i(\mathbf{x},t) = \int_R \mathscr{G}(|\mathbf{x}-\mathbf{x}'|)\mathscr{U}_i(\mathbf{x}',t)\,d\mathbf{x}' \\ \mathscr{G}(|\mathbf{x}-\mathbf{x}'|) = A \ \exp(-\frac{\pi|\mathbf{x}-\mathbf{x}'|^2}{2\lambda^2}) \end{cases} \tag{1.3}$$

with $i = 1, 2, 3$, A a turbulent kinetic energy and λ the integral length of turbulence.

More recently, Gea-Aguilera et al [56] proposed an advanced digital filter for the RPM method, inspired from the SEM. The filtering of white noise is replaced by two terms controlling the amplitude and direction of rotation of each eddy. The method was applied for leading-edge noise predictions and validated against analytical solutions from Amiet's model. This advanced filter was further improved to generate three-dimensional homogeneous anisotropic turbulence for the study of aerofoil-turbulence interaction noise.

Cascade of aerofoils

As for analytical approaches, work on cascades and simulation towards complete rotor-stator configuration have been investigated. The work of Golubev & Atassi [57] [58] can be cited as a frequency domain approach, allowing the computation of the acoustic response of an annular cascade of unloaded blades undergoing disturbances in a swirling mean flow. Significant distortion of the vortical disturbances are observed which must likely affects the unsteady loading of the blades. A temporal approach was chosen by Sescu & Hixon [59] who used the code BASS from the NASA Glenn Research Center, solving Euler equations to calculate the noise generated by the impingement of three-dimensional rotor wakes on an annular cascade of flat-plates. More recently, Polacsek et al [60] used a time-domain Euler solver coupled to a synthetic turbulence model to develop a hybrid method computing the aeroacoustic response of an annular cascade subjected to a prescribed homogeneous isotropic turbulent flow.

1.3 Reduction of Aerofoil-Turbulence Interaction (ATI) noise

1.3.1 Influence of 2D aerofoil geometrical parameters

Paterson & Amiet [8] conducted a series of experiments to validate the model of Amiet. Noise measurements were carried out on a two dimensional NACA 0012 aerofoil subject to a turbulent flow of various Mach numbers (from 0.1 to 0.5) and showed that the noise sources tend to be concentrated at the leading-edge. The analytical model shows good agreement with experiments, especially at low frequencies, but considerable discrepancies at high frequencies could be observed when the gust wavelength reaches a value similar to the aerofoil thickness. The authors considered these deviations to be due to the zero-thickness approximation in the flat-plate model. The effect of angle of attack was also investigated and found to have a very small influence on the far-field noise (no more than 1 or 2 dB).

Moreau et al [13] has measured turbulence interaction noise radiated by three different aerofoil profiles while varying the angle of attack and concluded that the influence of incidence is negligible on the radiated noise. These findings are confirmed by other experimental studies, such as Rozenberg [61] and Chaitanya [2]. Chaitanya [2] also studied the effect of camber with four different aerofoils, which was found to be negligible on the far-field noise. Moreau et al [13] also concludes that there is very little influence of camber on the radiated sound but observes a small radiation asymmetry for cambered profiles.

Many experimental studies were carried out to account more precisely for the effect of thickness on the radiated noise. A report from Moreau et al [13] gathering results from several research team (Oerlemans & Migliore [62], Paterson & Amiet [8], Olsen & Wagner [63]) concludes that increasing the aerofoil thickness leads to a reduction in the radiated noise, which becomes more important as frequency increases. Similar trends were obtained by Devenport et al [64], Hall et al [65] and Chaitanya [2]. In [49], Gill indicates that the reduction of noise with aerofoil thickness is related to the distortion of the vortical gusts by the velocity gradients at the leading-edge stagnation region such. The wavefront gust is smoothed across the leading-edge and the gust amplitude is reduced. Devenport et al [64] studied the behaviour of the airfoil gust response function with varying angle of attack AoA. The effect of angle of attack on the noise due to interactions with isotropic turbulence has been generally concluded as small (approximately 1 dB change when varying the AoA of a NACA 0012 airfoil between 0°and 12°) and been attributed to the movement of the stagnation streamline towards the pressure-side of the airfoil.

On the semi-analytical side, Gershfeld [66] developed a model accounting for the effect of aerofoil thickness by using a shape-dependant Green's function originally developed by Howe for trailing edge noise. In the same way, Lysak et al [67] proposed an empirical thickness correction factor based on time-domain calculations using Rapid Distortion Theory, while Moriarty et al [68] derived a simplified numerical correction model based on the Boundary Element Method and experimental observations. Chaitanya [2] compared these three semi-empirical corrections with experimental measurements. His study showed a fairly good agreement in the noise reduction predictions compared to a flat plate, but highlighted that the corrections could be enhanced by taking the nose shape into account.

Oerlemans & Migliore [62] and more recently, Chaitanya [2] and Hainaut et al [69] showed that a blunter nose radius decreases interaction noise at high frequencies due to effects of gust distortion near the nose radius. An analytical solution based on the linearization of the Euler equations was proposed by Ayton [70] for predicting interaction noise, accounting for the nose profile, thickness, camber and angle of attack.

Peake & Kerschen [29] proposed a cascade model taking into account the angle of attack, while effects of camber and thickness were implemented by Evers & Peake [30]. Results indicate that real aerofoil geometry may significantly influence individual vortical modes, while having a very small impact on broadband noise when summed over all modes. Noise variations compared to a flat-plate geometry were found to be less than 2 dB. These findings were confirmed by

Chaitanya [2] who studied the effects of real aerofoil geometry on the radiated noise generated by the interaction between a 2D cascade with a 2D turbulent flow, using the 3D viscous CFD solver HYDRA from Rolls-Royce. Chaitanya [2] concluded that the flat-plate assumption is good enough to predict the radiated power to within 1 or 2dB.

1.3.2 Serrated leading-edges

As detailed above, the research on aerofoil two-dimensional geometrical modifications conclude that the modifications of those geometrical parameters have very little effect on ATI noise and are not sufficiently effective to reduce ATI in a significant manner[2]. Other forms of passive treatments have therefore been investigated, such as the modifications of the leading-edge profile itself, by the introduction of serrations. Leading and trailing-edge serrations were first investigated from an aerodynamic point of view. It has been shown that serrations on the LE can prevent the aerofoil from separating and delay the onset of stall, due to the generation of secondary flows along the serration edge [71] [72] [73] [74] [75]. Favier et al [76], Hansen et al [77] and Chong et al [78] showed that the lift and drag coefficients can be improved by serrated leading-edges at post-stall conditions, but a decrease in lift at pre-stall conditions were observed.

Serrated leading-edges were later studied from an aeroacoustic point of view. Extending Amiet's model, Roger et al [79] developed an analytical model to take into account a sinusoidal leading-edge profile for a semi-infinite flat-plate with trailing-edge projected to infinity. The model uses a strip-theory approach as well as a second approach based on stretched coordinates. The author highlights the importance of the supercritical or sub-critical nature of the local impingement of a gust in the noise reduction capabilities. Clair et al [80] undertook an experimental and numerical investigation to study the effects of sinusoidal leading-edge profiles on interaction noise. Noise reductions of around 4dB were obtained experimentally and were well reproduced numerically. The author however noticed an over-prediction at high frequencies, which are believed to be due to the effect of trailing edge noise and to the fact that oblique gusts were not accounted for in the simulations.

Lau [81] performed a numerical investigation on the effects of wavy leading-edge amplitude and wavelength on aerofoil-gust interaction noise. The ratio between the wavy leading-edge amplitude and the streamwise wavelength of the incident gust was found to be a key factor in the noise reduction levels. The author also showed that the serrations introduce a phase shift in the gust response in the spanwise direction, resulting in surface pressure fluctuations of smaller amplitude which in turns provides a global noise reduction. The importance of the serration amplitude has also been reported by Narayanan et al [82] in a parametric experimental study on flat-plates in an open jet wind tunnel. The authors have also determined the existence of a minimum frequency above which noise reductions can be achieved. These findings are consistent with Lau et al [81] and with the hypothesis that noise reduction mechanisms are due to interference of sound radiated along the edges.

Kim et al [83] investigated flat-plate aerofoils with straight and wavy leading-edges using the code CANARD and identified two main mechanisms contributing to the noise reduction. The first is due to a drop in the source strength at the hill centre of the wavy leading-edge geometry, attributed to the obliqueness of the sinusoidal profile. The second is due to cut off effects along the oblique edge. Kim also suggests that there are destructive interference between the peak and hill region as another reduction mechanism. Additionally, the sources at the root were found to be dominant in comparison to the sources at the tip and along the oblique edge. These mechanisms were also suggested by Chaitanya et al [84] in an experimental study with realistic aerofoils, which showed similar trends in noise reduction between flat-plate and aerofoils. In this parametric investigation, the serration inclination angle was shown to constitute a key factor in noise reductions, with the existence of an optimum serration inclination angle at which maximum noise reductions occur. This optimum serration wavelength is found to be achieved when it is roughly equal to four times the transverse turbulent integral length-scale, guaranteeing that the root sources become incoherent. Chaitanya [2] also provided an analytical expression for the reduction of interaction noise for single-wavelength sinusoidal leading-edge profiles at this optimum condition, given by $10\log_{10}(fh/U)+10$, where h is the amplitude of the serration, which was in good agreement with experimental data. As an illustration, the power level reduction obtained with conventional serrations is plotted against $f(2h)/U$ in Fig. 1.4) from [2], with the analytical expression $10\log_{10}(fh/U) + 10$ represented by the dotted line.

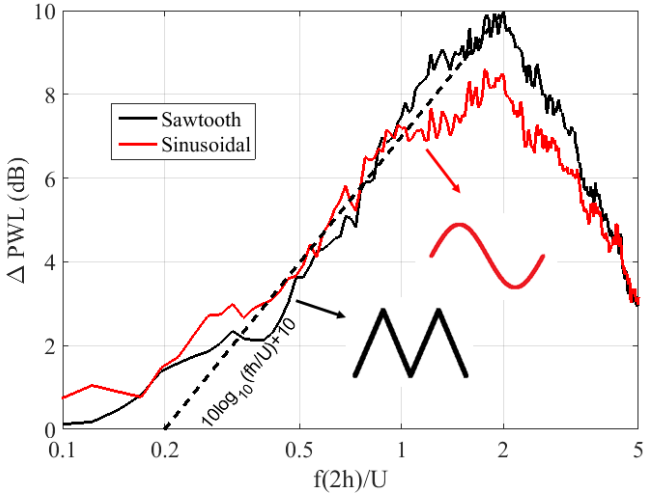

FIGURE 1.4: ATI noise reduction with serrated leading-edges aerofoil [2]

Based on Amiet's approach, Lyu et al [85] established a mathematical model for predicting aerofoil-turbulence interaction noise for serrated leading-edges, using Fourier expansions and Schwarzschild techniques. The model obtained very good agreement with experimental data and is consistent with previous findings concerning the effect of serration amplitude and hydrodynamic wavelength [81] [82] [84] [83]. The author also emphasizes on the importance of the spanwise correlation length in the noise reduction achievements, in order to allow destructive interference to occur.

To take advantage of these interference effects occurring between adjacent roots, Chaitanya et al [86] proposed a double-wavelength sinusoidal profile for which adjacent roots are separated in the streamwise direction. Additional noise reduction of around 4B was obtained at a particular frequency with these new profiles in comparison with single-wavelength profiles, therefore validating the mechanism of destructive interference between adjacent roots. Dual-frequency wavy-leading edges were also investigated by Turner et al [87] based on a numerical approach and found to notably enhance interaction noise reductions. At the maximum noise reduction frequency, the downstream and upstream root were found to be out-of-phase. Additionally, by comparing the downstream and upstream source strengths, the largest matching source strength between the two roots was also found to be obtained at that maximum noise reduction frequency. These observations therefore confirmed the principles of destructive interference and the location of the maximum source strength at the roots of the serration profile. An explanation concerning the disparities found in source strengths between the peak and the root location was given by Turner et al [88] in a numerical investigation of source mechanisms. The author determined the existence of a horseshoe-like vortex system created by the wavy leading-edge that produces secondary vortices at the leading-edge. This phenomenon leads to discrepancies in the streamwise vorticity distribution along the leading-edge profile, which further enhances the source strength at the serration roots [88]

Making use of the destructive interference existing between adjacent roots, Chaitanya et al proposed a number of innovative leading-edge profiles that are considerably more effective than conventional sinusoidal profiles [3]. Those profiles were constructed in a way that increases the number of coherent compact source regions per serration wavelength that destructively interfere, compared to a single wavelength serration. The different aerofoils were tested in the open jet wind tunnel facility at the ISVR, where they were placed in an isotropic turbulent flow. Figure 1.5 represents the reduction of sound power level obtained with those new profiles against a non-dimensional frequency fh/U, where h is the amplitude of the serration. Also shown in Fig. 1.5 is the line $10\log_{10}(fh/U) + 10$ representing the optimum sound power reduction achievable for a single-wavelength serration of the same amplitude. The noise reductions achieved were significantly higher than for conventional serrations, reaching around 15 dB for specific geometries presenting slits introduced at the root of the profile.

1.4 Slitted leading-edges for the reduction of broadband interaction noise

From the different profiles tested in [3], the slitted leading-edges have been identified as the geometry providing the best noise reductions, reaching $15dB$ at specific frequencies. As shown in Fig. 1.5, all geometries presenting slits introduced onto the roots of the profile provided enhanced noise reductions of around 8dB compared conventional sinusoidal profiles. The improved noise reductions specifically occur in a lower frequency region than the ones obtained with conventional profiles, which is of particular interest for the reduction of interaction noise. The slitted profiles however seem to be less effective at higher frequencies, probably due to secondary vortices interacting with the trailing edge. The characteristics of these vortices will be

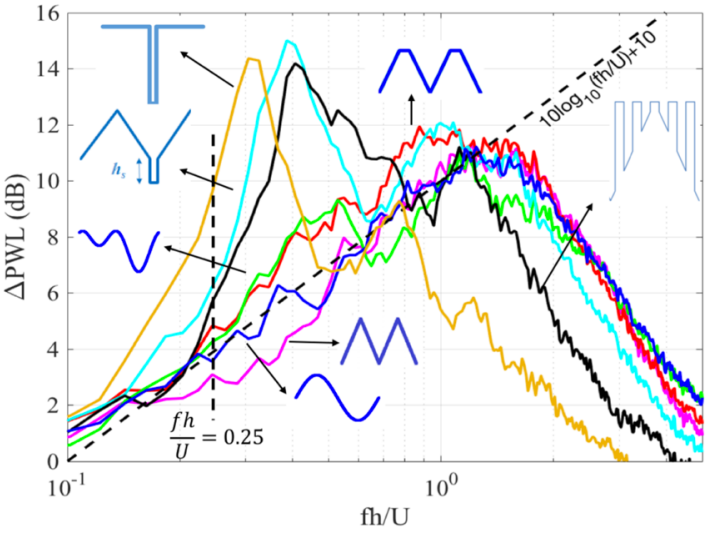

FIGURE 1.5: Enhanced noise reductions using innovative serrations: sound power reduction comparisons plotted against non-dimensional frequency - Experimental study [3]

discussed in this thesis. Chong et al showed in [89] that those secondary flow structures generated by the serrated leading edge could also have positive effect to reduce trailing edge noise. Additionally in the same study, Chaitanya et al [3] also compares the overall sound power reductions obtained from the different profiles, calculated for the frequency range of $fh/U = 0.1$-2 (Fig. 1.6). The results show here again that all geometries including slits in the profile provide a higher overall sound power reduction of more than 4 dB to more than 5dB, compared to overall reductions of less than 4dB for conventional profiles, which confirms the superior efficiency of slitted profiles. From all these slitted profiles, the most effective geometry, providing the highest overall noise reduction of 5.16 dB, simply comprises the introduction of narrow slits onto the leading-edge of the flat-plate. Chaitanya and Joseph [4] have proposed two noise reduction mechanisms to explain the enhanced noise reductions due to these slitted aerofoils. One is related to a reduction in overall source strength, the other is related to interference between two highly coherent sources at either ends of the slit of roughly the same strength. Based on the hypothesis of two compact coherent sources Chaitanya has proposed a model for predicting sound power reductions at any arbitrary frequency. The model was aimed at explaining his experimental observations which showed that maximum sound power reductions were obtained at frequencies f_n for which $f_n h/U = (2n+1)/2$, where $n = 0, 1, 2....$ This observation provided evidence of strong interference between two compact source regions at either ends of the slit, which was used as the basis of the model. Destructive interference are represented by the peaks at frequencies $f_n h/U = (2n+1)/2$ and constructive interference by the dips at $f_n h/U = (n+1)/2$. It can be noted that reductions still happen at those frequencies (constructive interference) due to the reduction of source strength occurring (as shown in Chapter 5 of this thesis). However, this model does not take into account the difference in travel times between the two compact sources to the observer, which will be shown to be necessary for accurate predictions in the present work. Additionally, no information is given on the relative contributions of source strength reduction and destructive interference on the total noise reduction provided by the slitted profiles. The sound power reductions obtained for slitted leading-edge profiles are represented in Fig. 1.7 from

[4] and compared with the optimum noise reductions obtained for conventional profiles represented by the dotted line $10\log_{10}(fh/U) + 10$ as in Fig. 1.5.

Serration profile	Dimensions	ΔOAPWL
Slitted	$w/\lambda = 0.13, a/\lambda = 0.87, \lambda/c_0 = 0.11$	5.16
Slitted-root	$h_s/c_0 = 0.21, \lambda/c_0 = 0.1$	4.86
Variable-slit	$\lambda/c_0 = 0.2, b/\lambda = 0.13, d/\lambda = 0.066$	4.30
Chopped-peak	$\lambda/c_0 = 0.1, l_c/\lambda = 0.33$	4.08
Double-wavelength	$\lambda_1/c_0 = 0.067, \lambda_2/c_0 = 0.133, \phi = \pi/2, h_1 = h_2$	3.66
Sinusoidal	$\lambda/c_0 = 0.1$	3.50
Sawtooth	$\lambda/c_0 = 0.1$	3.08

[a]Overall sound power reduction levels (ΔOAPWL) are calculated for the frequency range of $fh/U = 0.1$–2, where the OAPWL for the baseline is 76.22 dB at a flow velocity of 60 m/s.

FIGURE 1.6: Leading-edge serration profiles considered in this study for the same peak-to-root amplitude of $hc0 = 0.167^a$ [2]

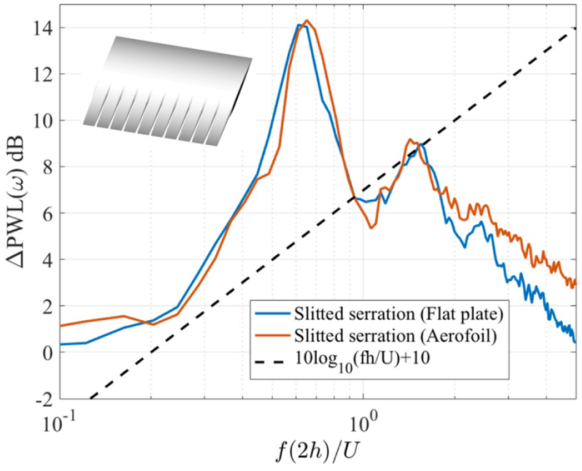

FIGURE 1.7: Sound power reduction comparisons for a slitted serration on flat plate and aerofoil of amplitude-chord ratio ($h/c = 0.167$), width-wavelength ratio $w/\lambda = 0.133$ at jet velocity of 60 m/s [4]

The work due to Ayton in [3] provided an analytic model to predict the noise radiation due to any arbitrary periodically varying leading-edge flat plate profile interacting with a single harmonic vortical gust. The analytic model is based on the solution of the acoustic wave equation using the Wiener–Hopf technique and therefore neglects secondary vorticity. Poor agreement with the experimental noise reductions is obtained for the slitted profiles, which suggests that the secondary vorticity plays an important role in the generation of the source strength distribution. Additionally in [3], an optimum slit ratio $a/w \approx 7$, with w the slit width and a the leading-edge length, has been determined experimentally, for which maximum noise reductions are obtained. However, the reasons for the value of this optimum are still unclear and will be investigated in greater details in this thesis.

The current research on leading-edge profiles presented above therefore establishes through experimental work the superior noise reductions that can be obtained with slitted geometries but the physical mechanisms responsible have not yet been identified and represent a crucial step in the optimisation of aerofoil leading-edge profiles. Computational work is required to provide a

deeper understanding of the generation of the compact sources on the aerofoil surface as well as to identify the factors controlling the source strength distribution and their effects.

1.5 Objectives and contribution

As stated above, numerical methods have been extensively used to investigate the use of conventional single and double-wavelength sinusoidal and sawtooth profiles on ATI noise [90] [91] [92] but have been restricted to these conventional profiles.

This thesis focuses on the investigation of slitted leading-edge geometries implemented on flat plates through a mostly numerical approach. The thesis has the following objectives:

1. To validate the noise reduction obtained using leading-edge slits in recent experimental studies
2. To identify and understand more precisely the noise reduction mechanisms involved in the use of slitted leading-edge profiles
3. To extend the analytic two-source model developed by Chaitanya [4] to obtain more accurate predictions of noise reductions
4. To optimize leading-edge profiles for maximum noise reductions through a detailed parametric study
5. To perform an experimental validation of the present numerical investigation

1.6 Scope of the thesis

The present chapter outlines the main motivations for this project and outlines the current methods available to predict and reduce aerofoil-turbulence interaction noise and presents the objectives of the thesis. Chapter 2 contains a presentation of the computational method used in this investigation. In Chapter 3, the analytical model developed by Amiet to predict ATI noise is used to validate the numerical methodology detailed in Chapter 2, on a flat-plate subject to a single spanwise vortex. Chapter 4 presents the study of the physical mechanisms of slitted leading-edge profiles by investigating the source distribution of the aerofoil surface. The far-field radiation of slitted-profiles is investigated in Chapter 5, which extends the two-source model proposed by Chaitanya et al [4]. A numerical parametric study on different slit configurations is presented in Chapter 6 in order to provide general guidelines for the optimisation of slitted profiles. A validation of this parametric study is performed experimentally in Chapter 7. Finally, conclusions and future work required are in Chapter 8.

1.7 Publications

1.7.1 Journal papers

M. Cannard, P. Joseph, J. Turner, J.W. Kim and P. Chaitanya (2020). 'Physical mechanisms and performance of slitted leading-edge profiles for the reduction of broadband aerofoil interaction noise', 473, article 115214, ***Journal of Sound and Vibration***.

M. Cannard, P. Joseph, P. Chaitanya and J.W. Kim (2020). 'Parametric study on slitted leading-edge profiles for thereduction of broadband aerofoil interaction noise', submitted to ***AIAA Journal***.

1.7.2 Conference papers

M. Cannard, P. Joseph, J. Kim, P. Chaitanya, 'Numerical investigation into slitted leading-edge profiles for reducing interaction noise'. In ***25th International Congress on Sound and Vibration 2018, ICSV 2018: Hiroshima Calling.*** vol. 3, International Institute of Acoustics and Vibration (IIAV). pp. 1366-1373 .

M. Cannard and P. Joseph and J. Turner and J.W. Kim and P. Chaitanya, 'Slitted leading-edge profiles for the reduction of broadband interaction noise; physical mechanisms and performance', presented in ***25th AIAA/CEAS Aeroacoustics Conference***, May 2019, Delft, number 2019-2511.

Chapter 2

Computational method

In this chapter, the computational method used for the current investigation is presented. The present work is realised using an in-house 3D compressible Euler solver developed by Kim, known as CANARD (Computational Aerodynamics & Aeroacoustics Research coDe). The general approach of this solver is to inject vortical disturbances in the computational domain, that will travel downstream and impinge over an isolated aerofoil. In this investigation, the vortical disturbances are modelled by a single spanwise vortex. The distribution of fluctuating pressure over the aerofoil surface as well as the far-field radiated noise induced are determined by resolution of the governing equations on an adapted grid. The details of the single spanwise vortex model is further detailed in chapter 4.

2.1 Governing equations

The choice of solving the full 3D compressible Euler equations to model the aerofoil response is validated by the inviscid nature of AVI noise [39]. The computational cost can therefore be reduced by not considering the viscous terms during the simulation, which also allows to prevent the generation of other unwanted types of noise, like aerofoil self noise requiring a boundary layer to develop.

The governing equations are solved in conservative form and expressed in a generalized coordinate system as given by Eq. 2.1. The generalized coordinates are given by $\xi_i = \{\xi, \eta, \zeta\}$, while the Cartesian system is represented by $x_j = \{x, y, z\}$ with $i = 1, 2, 3$ and $j = 1, 2, 3$. The Jacobian determinant of the coordinate transformation from Cartesian to generalized coordinates is given by $J = |\partial(\xi, \eta, \zeta)/\partial(x, y, z)|$.

$$\frac{\partial}{\partial t}\left(\frac{\mathbf{E}}{J}\right) + \frac{\partial}{\partial \xi_i}\left(\frac{\mathbf{F}_j}{J}\frac{\partial \xi_i}{\partial x_j}\right) = -\frac{c}{L}\frac{\mathbf{S}}{J} \tag{2.1}$$

$\mathbf{E}$ and $\mathbf{F}$ respectively represent the conservative variable and flux vectors and are defined by

$$\mathbf{E} = \begin{bmatrix} \rho \\ \rho u \\ \rho v \\ \rho w \\ \rho e_t \end{bmatrix}, \quad \mathbf{F}_j = \begin{bmatrix} \rho u_j \\ \rho u u_j + \delta_{1j} p \\ \rho v u_j + \delta_{2j} p \\ \rho w u_j + \delta_{3j} p \\ (\rho e_t + p) u_j \end{bmatrix}$$

The fluctuating velocity field is given by $u_j = \{u, v, w\}$ and $e_t = p/\left[(\gamma - 1)\rho + u_j u_j/2\right]$ represents the internal energy per unit mass. An additional source term $\mathbf{S}$ is included on the RHS of the governing equations and represent a sponge zone surrounding the computational domain (see section 2.5.1).

2.2 Computational domain and grid generation method

Computational domain

A flat-plate aerofoil with zero thickness and no incidence is placed at the centre of the computational domain, which consists of a rectangular prism. The aerofoil chord is made semi-infinite in the direction of the trailing-edge to remove the back-scattering otherwise occurring when the vortex reaches the end of the flat-plate and interfering with the leading-edge noise.

The computational domain is decomposed into 6 blocks arranged in a H-topology and is surrounded by a sponge zone, aimed at attenuating numerical reflections from the boundaries. The use of a multi-block grid allows the use of more than one computational mesh in the complete domain, which facilitates the meshing of complex regions and brings more efficiency to run the code in parallel. The no-thickness flat plate is modelled using a slip-wall boundary condition in between two adjacent blocks. One sided differences are applied there so no information passes between the two blocks, representing the two sides of the plate. A screenshot of the computational domain is available in Fig. 2.1.

Grid generation

The accuracy of any CAA analysis is highly dependent on the quality of the mesh generated in the computational domain. In particular, the design of a mesh needs to full-fill some requirements that are not always straightforward, especially when high-order methods are used in combination with curvilinear meshes to solve the governing equations [93].

In the present analysis, the grid is Cartesian in the case of a flat-plate with a straight leading-edge, but remains non-uniform in the plane $x - y$. Indeed, as the main important features of the flow need to be captured, a clustering of points is necessary in some regions of the computational domain. The grid spacing is for example reduced upstream the aerofoil in order to resolve adequately the vortex, but stretched in regions where the flow is fully developed. This allows an accurate representation of the main characteristics of the flow without having to keep such a refinement in the complete domain, which would be computationally too expensive. However,

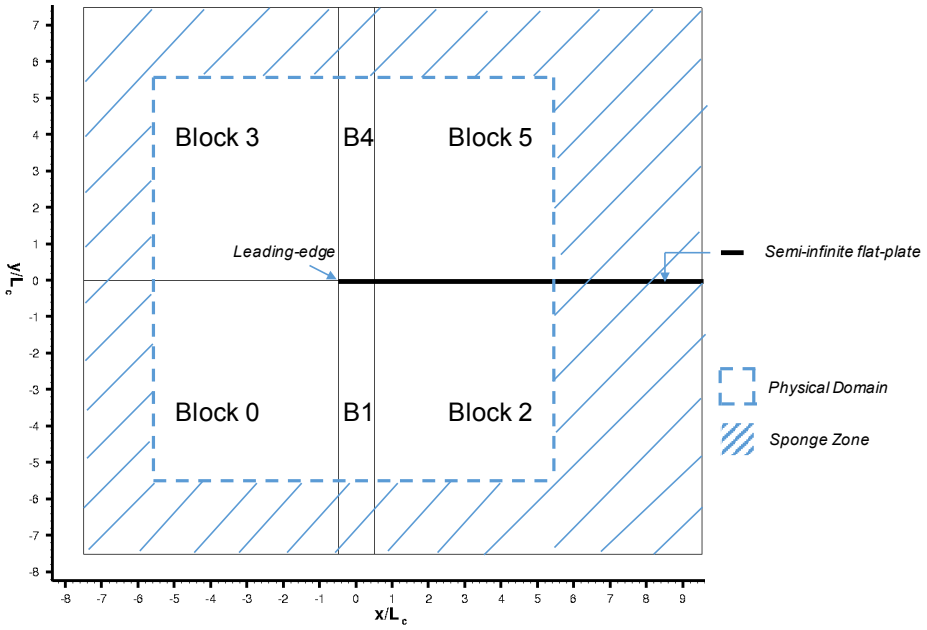

FIGURE 2.1: Computational domain

these regions of extreme aspect ratio or important skewed cells very often lead to the development of spurious waves [93] [94]. This phenomenon can further be aggravated by the use of high-order centred schemes, such as the one used in the present investigation (section 2.3). Indeed the non-dissipative nature of these schemes would allow the spurious waves to grow and spread inside the domain, leading to computational failure [31]. For these reasons, the chosen mesh generation method should be able to produce smooth grid functions.

In this study, the mesh is generated by an algebraic grid generation method. As suggested by the name, this method uses algebraic equations (such as polynomial interpolation) to determine the grid points, based on specified boundary grid points [93]. Here, the polynomials are constructed so that the grid functions are smooth between all the points, till the second derivative included. Algebraic methods have the reputation of being very fast computationally and able to easily cluster grid points in specific regions through weighting terms in the equations.

In the present case, the mesh is here refined at the leading edge of the flat plate to a minimum grid element $\Delta x_{min} = 0.00625$, which corresponds to 1/160 of the chord. The grid is uniform in the z-direction with a spacing of $\Delta z = 0.0025$. It should be noted that the mesh becomes curvilinear once wavy leading-edges are introduced and the grid refined in the z-direction depending on the wavelength of the WLE profile.

2.3 Spatial discretisation

The nonlinear Euler equations are solved in the time-domain using optimized high-order finite-difference compact schemes and filters [95] [96] that can be put in the form of a pentadiagonal

matrix system, described in Eq. 2.2.

$$\mathbf{P}\overline{\mathbf{f}}\mathbf{'} = \frac{1}{\Delta x}\mathbf{Q}(\mathbf{f} + \mu\widetilde{\Delta}\mathbf{f}) \tag{2.2}$$

In this system, $\mathbf{f} = (f_0, f_1, ..., f_N)^T$, $\mathbf{f'} = (f'_0, f'_1, ..., f'_N)^T$ and $\widetilde{\Delta}\mathbf{f} = (\widetilde{\Delta}f_0, \widetilde{\Delta}f_1, ..., \widetilde{\Delta}f_N)^T$ respectively represent the nodal values of the objective function, the numerical approximation of the derivative and the filter's contribution. The matrices $\mathbf{P}$ and $\mathbf{Q}$ contain the finite-difference scheme coefficients. The parameter μ is set to either 0 (without filter) or 1 (with filter).

2.3.1 Compact scheme

The spatial discretisation is realised by the following fourth-order optimised compact central finite-difference scheme [95], based on a seven-point stencil:

$$\beta\overline{f}'_{i-2} + \alpha\overline{f}'_{i-1} + \overline{f}'_i + \alpha\overline{f}'_{i+1} + \beta\overline{f}'_{i+2} = \frac{1}{\Delta x}\sum_{m=1}^{3} a_m(f_{i+m} - f_{i-m}) \tag{2.3}$$

The use of compact (Pade) schemes have become an attractive choice to achieve low-dispersion and low-dissipation characteristics. Indeed due to their implicit nature, compact schemes usually achieve higher order accuracy than their explicit counterpart schemes by offering more parameters to optimise the truncation order and/or the spectral characteristics [31]. As a result, smaller stencils are required for a larger resolution bandwidth, also implying less computational resources. In return, a linear system of equations must be solved to compute the first derivative.

In addition, the present compact scheme is also central and therefore non-dissipative. This constitutes another advantage, by preventing important attenuation of signals and allowing the capture of small-amplitude acoustic fluctuations. In counterpart, the use of a filter will be required to avoid the growth of numerical instabilities (section 2.3).

As in Eq. 2.3, the system can be put in the matrix-vector form $\mathbf{P}\overline{\mathbf{f}}\mathbf{'} = \frac{1}{\Delta x}\mathbf{Q}\overline{\mathbf{f}}$, with $\mathbf{P}$ and $\mathbf{Q}$ containing the LHS and RHS coefficients of the scheme.

$$\mathbf{P} = \begin{bmatrix} 1 & \gamma_{01} & \gamma_{02} & 0 & \dots & 0 & 0 & 0 & 0 \\ \gamma_{01} & 1 & \gamma_{12} & \gamma_{13} & 0 & \dots & 0 & 0 & 0 \\ \gamma_{20} & \gamma_{21} & 1 & \gamma_{23} & \gamma_{24} & 0 & \dots & 0 & 0 \\ 0 & \beta & \alpha & 1 & \alpha & \beta & 0 & \dots & 0 \\ \vdots & \ddots & \ddots & \ddots & \ddots & \ddots & \ddots & \ddots & \vdots \\ 0 & \dots & 0 & \beta & \alpha & 1 & \alpha & \beta & 0 \\ 0 & 0 & \dots & 0 & \gamma_{24} & \gamma_{23} & 1 & \gamma_{21} & \gamma_{20} \\ 0 & 0 & 0 & \dots & 0 & \gamma_{13} & \gamma_{12} & 1 & \gamma_{10} \\ 0 & 0 & 0 & 0 & \dots & 0 & \gamma_{02} & \gamma_{01} & 1 \end{bmatrix}$$

$$\mathbf{Q} = \begin{bmatrix}
b_{00} & b_{01} & b_{02} & b_{03} & b_{04} & b_{05} & b_{06} & 0 & 0 & \dots & 0 \\
b_{10} & b_{11} & b_{12} & b_{13} & b_{14} & b_{15} & b_{16} & 0 & 0 & \dots & 0 \\
5b_{20} & b_{21} & b_{22} & b_{23} & b_{24} & b_{25} & b_{26} & 0 & 0 & \dots & 0 \\
-a_3 & -a_2 & -a_1 & 0 & a_1 & -2 & a_3 & 0 & 0 & \dots & 0 \\
0 & -a_3 & -a_2 & -a_1 & 0 & a_1 & a_2 & a_3 & 0 & \dots & 0 \\
\vdots & \ddots & \ddots & \ddots & \ddots & \ddots & \ddots & \ddots & \ddots & \ddots & \vdots \\
0 & \dots & 0 & -a_3 & -a_2 & -a_1 & 0 & a_1 & a_2 & a_3 & 0 \\
0 & \dots & 0 & 0 & -a_3 & -a_2 & -a_1 & 0 & a_1 & a_2 & a_3 \\
0 & \dots & 0 & 0 & -b_{26} & -b_{25} & -b_{24} & -b_{23} & -b_{22} & -b_{21} & -b_{20} \\
0 & \dots & 0 & 0 & -b_{16} & -b_{15} & -b_{14} & -b_{13} & -b_{12} & -b_{11} & -b_{10} \\
0 & \dots & 0 & 0 & -b_{06} & -b_{05} & -b_{04} & -b_{03} & -b_{02} & -b_{01} & -b_{00}
\end{bmatrix}$$

The compact interior scheme can be applied at the nodes $3 \leq i \leq N-3$, but different sets of coefficients (γ_{ij} and b_{ij}) have to be derived for the boundary and near-boundary nodes $i = \{0, 1, 2\}$ and $i = \{N-2, N-1, N\}$, corresponding to the boundary closure schemes (see below).

Optimisation of the interior scheme

The accuracy of finite-difference schemes can be assessed by truncation error analysis, giving an asymptotic estimate of the error in the scheme. Obtained by Taylor series expansion of the scheme, the truncation error can be improved to increase numerical accuracy by adding correction terms or adjusting the scheme coefficients [31].

Another approach to assess the quality of a scheme is the analysis of spectral resolution properties, referred to as dispersion and dissipation. They respectively correspond to the real and imaginary part of a modified wavenumber, determined by Fourier analysis of the numerical scheme (Eq. 2.3). These spectral properties represent the error in the wave propagation characteristics of a single Fourier mode [97].

Although maximizing the order of accuracy is a traditional method to reduce numerical errors, it has been shown more recently that improving the spectral resolution could considerably enhance the quality of a scheme [31] [97]. This strategy was used by Kim [95] to optimize the current compact finite-difference scheme: a constraint was applied on some coefficients to achieve a certain truncation error and the remaining parameters were determined to minimize an integrated error between the exact and modified wavenumber over a specified wavenumber range [95].

Boundary closure strategy

As mentioned above, the compact finite-difference scheme defined in Eq. 2.3 cannot be applied at the nodes $i = \{0, 1, 2\}$ (and respectively at the nodes $i = \{N-2, N-1, N\}$). In order to close the system of equations, boundary and near-boundary schemes need to be derived.

To this end, a set of extrapolation functions is defined to approximate and replace the objective function when exterior terms are encountered in the scheme [95]. These extrapolation functions are constructed based on a linear combination of polynomial and trigonometric series, whose coefficients are determined by matching conditions that keep the 7-point stencil, as well as the 4^{th} order accuracy. The resulting compact boundary schemes are non-central and their coefficients are expressed in terms of the interior coefficients.

As for the interior scheme, the spectral properties of the boundary schemes can be optimized by Fourier analysis. For this purpose, additional parameters are included in the extrapolated functions and optimised in a way that minimises the relative difference between the interior and boundary modified-wavenumbers [95]. This procedure allows the boundary schemes to approximately achieve the same resolution characteristics as the interior schemes. Being non-central, it should be noted that the boundary schemes will always display some level of dissipation, which is maintained reasonably low by the spectral optimisation.

For information, another boundary scheme is used for parallelisation purposes at the subdomain interfaces, based on a decomposition of the pentadiagonal matrix system into quasi-disjoint subsystems [98]. These subdomain boundary schemes involve an exchange of three halo terms between subdomains.

2.3.2 Compact filter

Because of the non-dissipative nature of central schemes, any numerical instability originated from spurious solutions might expand and spread into the computational domain [31]. A possible treatment to avoid this coupling between physical and spurious solutions consists in filtering the values by the introduction of a cut-off frequency. At the end of each time step, poorly-resolved waves will be removed from the solution, improving numerical stability [97].

Derivation of compact filters

In this study, the values are filtered by the term $\widetilde{\Delta}\mathbf{f}$ (Eq. 2.3) based on the following pentadiagonal compact scheme [96], where $\widetilde{\Delta} f_i = \widetilde{f}_i - f_i$ represents the difference between filtered and original values:

$$\beta\widetilde{\Delta} f_{i-2} + \alpha\widetilde{\Delta} f_{i-1} + \widetilde{\Delta} f_i + \alpha\widetilde{\Delta} f_{i+1} + \beta\widetilde{\Delta} f_{i+2} = \sum_{m=1}^{3} a_m (f_{i-m} - 2f_i + f_{i+m}) \tag{2.4}$$

The coefficients were optimised by Fourier analysis to achieve a desired cut-off wavenumber, as well as a sixth-order accuracy [96]. As for the main scheme, the system can be put in a matrix-vector notation taking the form $\mathbf{R}\widetilde{\Delta}\mathbf{f} = \mathbf{T}\mathbf{f}$ with the matrix $\mathbf{R}$ and $\mathbf{T}$ respectively containing the LHS and RHS coefficients of the filter.

Boundary closure filter strategy

Similar to the strategy used to close the main compact scheme, an extrapolation function based on a linear combination of exponential functions is used to derive boundary filters and close the pentadiagonal matrix [96]. Coefficients are expressed in terms of the interior filter coefficients, themselves only depending on the desired cut-off wavenumber.

As the main boundary compact schemes, the boundary filters are non-central and therefore achieve a lower resolution than the interior filters. To counterbalance this fact, a weighting factor is applied on the desired cut-off wavenumber in order to attribute lower cut-off frequencies for the boundary filters [96].

As for the main scheme, another boundary closure filter strategy is used at the subdomain interfaces for parallelisation purposes [98].

2.4 Temporal discretisation

Once the governing equations have been discretised in space, a time-stepping method needs to be applied to advance the solution in time. In the current work, this is achieved by a fourth-order four-stage Runge-Kutta method (RK4) which requires four evaluations of the spatial derivatives to be performed. After spatial discretisation, the differential equation to be solved can be expressed as in Eq. 2.5 and the RK4 time-marching procedure is given by the system in Eq. 2.6, where $\mathbf{E}$ represents the conservative variables and $\mathbf{G}$ contains the flux derivatives and the source term defined as $\mathbf{F}$ and $\mathbf{S}$ in Eq. 2.1.

$$\frac{d\mathbf{E}}{dt} = \mathbf{G}(\mathbf{E}, t) \tag{2.5}$$

$$\begin{cases} \mathbf{C}_0 = \mathbf{E}^n \\ \mathbf{C}_1 = \mathbf{E}^n + \mathbf{G}(\mathbf{C}_0, t)\ \ \Delta t/4 \\ \mathbf{C}_2 = \mathbf{E}^n + \mathbf{G}(\mathbf{C}_1, t)\ \ \Delta t/3 \\ \mathbf{C}_3 = \mathbf{E}^n + \mathbf{G}(\mathbf{C}_2, t)\ \ \Delta t/2 \\ \mathbf{Q}^{n+1} = \mathbf{E}^n + \mathbf{G}(\mathbf{C}_3, t)\ \ \Delta t \end{cases} \tag{2.6}$$

The chosen method is explicit and therefore only requires the values of the solution at the previous time step to calculate the new solution time. Although implicit time-marching schemes are not subjected to any stability constraint, the explicit version of the RK4 was here considered since enough stability could be achieved for this nonlinear problem, saving some important computational cost.

Because of the explicit nature of the time-marching scheme, the time step is restricted by the Courant-Friedrichs-Lewy condition ($CFL < 1$) to satisfy stability. The CFL is here set to $CFL = 0.95$ and the time step determined accordingly:

$$CFL = \Delta t(U_\xi + U_\eta + U_\zeta) \tag{2.7}$$

with U_ξ, U_η and U_ζ the maximum speed at which information can propagate, respectively in the ξ, η and ζ directions.

2.5 Boundary conditions

The application of adapted boundary conditions are one of the most important elements of the entire computation. Indeed, a number of issues encountered in the computational domain are actually generated at the boundaries [31]. Typically, boundary conditions permit the flow to enter or exit the computational domain in a smooth manner. They are also used to define any body of interest inside the computational domain. This implies preventing reflections from outgoing waves. When the boundary conditions are not well-defined, disturbances are created at these regions and outgoing waves are reflected, which propagate back inside and grow under the shape of spurious solutions contaminating the solution [97].

In the present computation, two strategies are simultaneously used. The computational domain is first surrounded by a sponge zone that attenuates spurious waves as they travel through the layer. Secondly, generalized characteristic boundary conditions developed by Kim [99] [100] are applied at the outer boundaries of the sponge zone and also used to define the aerofoil surfaces.

2.5.1 Sponge zone

The computational domain is composed of a physical region where the governing equations are solved and surrounded by a sponge zone where a treatment of the flow variables is applied. The sponge zone is modelled by an additional source term on the RHS of the governing equations [101], defined as follow:

$$\mathbf{S} = \begin{cases} \sigma_s(x,y)\left[\rho - \rho_\infty, \lambda_s(x)\rho(\mathbf{u} - \mathbf{u}_t), p - p_\infty\right] & \text{for } \mathbf{x} \in \Omega_{sponge} \\ 0 & \text{for } \mathbf{x} \in \Omega_{physical} \end{cases} \tag{2.8}$$

The sponge zone is essentially used as an absorbing treatment to attenuate disturbances before they reach the outer boundaries: while travelling through the buffer, the amplitude of the waves is scaled by the damping coefficient $\sigma(x, y)$, increasing from zero inside the computational domain to a positive value σ_0 as it reaches the outer boundaries [101]. As a result, the density and

pressure can be forced to smoothly return to ambient values and the velocity set to a defined target. Similarly, when disturbances are reflected from the outer boundaries, they are damped by the sponge zone as they travel back inside the computational domain. The scaling factor $\sigma(x, y)$ is adjusted in such a way that a sufficient amount of attenuation is provided to the disturbances and is defined by the following equations:

$$\begin{cases} \sigma_s(x,y) = \frac{\sigma_0}{2}(1 + \cos\ [\pi \mathscr{A}(x)\mathscr{B}(y)]) \\ \mathscr{A}(x) = 1 - \max\ (\frac{x_a - x}{x_a - x_{min}}, 0) - \max\ (\frac{x - x_b}{x_{max} - x_b}, 0) \\ \mathscr{B}(x) = 1 - \max\ (\frac{y_a - y}{y_a - y_{min}}, 0) - \max\ (\frac{y - y_b}{y_{max} - y_b}, 0) \end{cases} \tag{2.9}$$

Additional control is provided to the velocity forcing by the weighting factor $\lambda_s(x)$ as the forcing profile differs from the one used for the pressure and density:

$$\lambda_s(x) = (1 + \delta)\,[1 - \tanh\ (x/L] + 1 \quad \text{with} \quad \delta = \min\ [2M/(1 + M), 1] \tag{2.10}$$

2.5.2 Generalized characteristic boundary/interface conditions

Additionally to the sponge zone, boundary conditions are applied at the outer boundaries of the sponge layer, wall surfaces to define the aerofoil and at the block/subdomain interfaces. Generalized characteristic boundary conditions were developed by Kim [99] [100] for this purpose and are used in the present computation.

The basic idea behind the generalized characteristic boundary conditions is to update and correct the amplitude of the incoming characteristic waves according to the boundary condition desired. To this end, the governing equations written in conservative form and generalized coordinates (Eq. 2.1) have to be manipulated and re-written into a characteristic form in the direction normal to the boundary surface considered [99]. Eq. 2.11 shows for instance the equation used to derive the GCBC for the boundaries normal to the n-direction.

$$\frac{\partial \mathbf{H}}{\partial t} + \underline{\Lambda}\frac{\partial \mathbf{H}}{\partial n} = -\underline{\mathbf{D}}^{-1}\mathbf{S}^* \tag{2.11}$$

This equation is a quasi-linear characteristic wave equation, with $\mathbf{H} = \underline{\mathbf{D}}^{-1}\mathbf{E}$ representing the characteristic variables and $\mathbf{D}^{-1}$ the transformation matrix from the flow variables $\mathbf{E}$. The diagonal matrix $\underline{\Lambda}$ holds the phase speeds of the characteristic waves. The transverse fluxes are included in the new source term $\mathbf{S}^*$ of the RHS of Eq. 2.11, while the second term of the LHS contains the fluxes in the normal direction and can also be written:

$$L_i = \lambda_i \frac{\partial H_i}{\partial n}, \qquad (\text{i} = 1,\ 2,\ ...,\ 5) \tag{2.12}$$

These terms can be classified as either incoming or outgoing according to the sign of the speed term λ_i. Outgoing terms are calculated using the interior nodes, while physical boundary conditions are derived and applied to correct the amplitude of incoming waves. This defines an updated characteristic variables vector, and the corresponding modified value of the flow variables at the boundaries can be obtained using the reverse transformation. Flow variables are finally replaced by their modified version during the time-marching step.

Non-reflecting [99] and no-slip boundary conditions [100] were derived by Kim for use in this generalized characteristic method, which are used in the present work at the far-field boundaries and to define the aerofoil surfaces. The no-slip condition is extended through the blocks 2 and 5 to model the semi-infinite chord in the trailing-edge direction.

Chapter 3

Prediction of aerofoil-turbulence interaction noise

In this chapter, the computational method used in the current work is validated against the analytical model of Amiet, which relates to flat-plate turbulence interaction noise. The simulation considers a flat-plate in a uniform mean flow being impacted by vortical perturbations injected upstream of the aerofoil. The vortical perturbations are modelled by a single spanwise vortex. The vortex filament presents no spanwise variation since a periodic boundary condition being applied in the spanwise direction. Amiet's model, developed for a three-dimensional configuration, is modified to account for the propagation in a 2D field. The 2D Amiet formulation is first presented in this chapter. Details concerning the computational setup are then presented, followed by a comparison of the predicted results for aerofoil-turbulence interaction noise with the 2D flat-plate formulation.

3.1 Amiet's model

The impingement of a turbulent flow onto the leading-edge of an aerofoil generates pressure fluctuations over the surface, due to the fluctuating component of the velocity normal to the chord. Using the acoustic analogy, these fluctuations can be assimilated to a dipole source distribution which radiates to the far-field. In Amiet's model [10], the distribution of dipole sources over the aerofoil surface is first determined by thin-aerofoil theory. The far-field noise is then calculated using the theory of Kirchhoff.

The origin of the coordinate system (x_1, x_2, x_3) is at the centre of the aerofoil, with the x_1- and x_3-coordinates respectively extending in the chordwise and spanwise direction while the x_2-coordinate is oriented normal to the profile (Fig. 3.1). The mean flow $\mathbf{U}$ is in the x_1-direction and defined by the velocity vector $\mathbf{U} = (U, 0, 0)$. The observer is in the far-field at the location (y_1, y_2, y_3) and no shear-layer is considered (jet-stream extended to infinity). Based on thin-aerofoil theory, the model does not take into account the exact geometry of the aerofoil, which

is considered as a flat plate with zero thickness and no angle of incidence. The configuration of the model is depicted in Fig. 3.1.

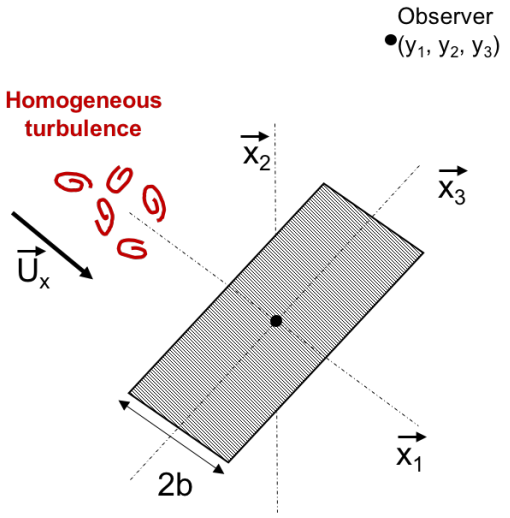

FIGURE 3.1: Configuration of Amiet's flat-plate model

The incident vorticity field is modelled by a perturbation introduced upstream of the flat plate and decomposed in Fourier series, where one component of the perturbation is referred to as a sinusoidal gust. The turbulence is assumed to be frozen and only convected by the mean flow [10]. In the present analysis, there is no variation of the turbulence in the spanwise direction. As a result, an incoming sinusoidal gust with no spanwise variation is represented in the aerofoil fixed coordinate system by $w_g(x_1,t) = w_0 e^{i\left[k_{x_1}(x_1-Ut)\right]}$, with k_{x_1} the wavenumber in the x_1-direction and w_0 the velocity amplitude of the harmonic gust. The complete turbulent velocity is obtained by integration over the k_{x_1} wavenumbers and defined by Eq. 3.1, where $\hat{w}_R$ indicates the spatial Fourier transform of w.

$$w\left(x_1,t\right) = \int_{-\infty}^{+\infty} \hat{w}_R(k_{x_1}) e^{i\left[k_{x_1}(x_1-Ut)\right]}\, dk_{x_1} \tag{3.1}$$

3.1.1 Pressure distribution over the aerofoil surface

The pressure jump Δp across a flat plate aerofoil of infinite span generated by the sinusoidal gust w_g is given by Eq. 3.2, where ρ the mean-flow density. The function g represents the transfer function between the turbulent velocity and the aerofoil pressure jump distribution along the chord.

$$\Delta p\left(x_1,t\right) = 2\pi\rho U w_0 g\left(x_1,k_{x_1}\right) e^{-ik_{x_1}Ut} \tag{3.2}$$

The unsteady pressure jump due to the complete turbulent field Δp_T is obtained by integration over all wavenumber components and given by Eq. 3.3:

$$\Delta p_T\left(x_1,t\right) = 2\pi\rho U \int_{-\infty}^{+\infty} \hat{w}_R(k_{x_1}) g(x_1,k_{x_1}) e^{-ik_{x_1}Ut}\, dk_{x_1} \tag{3.3}$$

Performing a Fourier transform with respect to time (Eq. 3.4) gives an expression for the unsteady pressure jump in the frequency domain, given by Eq. 3.5:

$$\Delta\hat{p}_T\left(x_1,\omega\right) = \frac{1}{2\pi}\int_{-\infty}^{+\infty} \Delta p_T\left(x_1,t\right) e^{-i\omega t}\, dt \tag{3.4}$$

$$\Delta\hat{p}_T\left(x_1,\omega\right) = 2\pi\rho U \int_{-\infty}^{+\infty} \hat{w}_R(k_{x_1}) g(x_1,k_{x_1}) \left(\frac{1}{2\pi}\int_{-\infty}^{+\infty} e^{i(k_{x_1}U-\omega)t}\, dt\right) dk_{x_1} \tag{3.5}$$

The term in brackets is the Dirac delta function, which automatically provides a relationship between k_x and ω.

$$\frac{1}{2\pi}\int_{-\infty}^{+\infty} e^{-ipt}\, dt = \delta(p) = \begin{cases} 1 & \text{if } p = 0 \\ 0 & \text{otherwise} \end{cases} \tag{3.6}$$

with $p = k_{x_1}U - \omega$.

For frozen turbulence, the wavenumber in the chordwise direction is therefore imposed and equal to $K_c = \omega/U$. The final expression for the pressure jump in the frequency-domain is given by Eq. 3.7:

$$\Delta\hat{p}_T\left(x_1,\omega\right) = 2\pi\rho U\ \hat{w}_R(K_c)\ g(x_1,K_c) \tag{3.7}$$

3.1.2 Far-field radiation of the dipole sources distribution

According to the acoustic analogy, the radiated noise can be calculated by considering a distribution of dipole sources over the aerofoil surface whose strength is equal to the unsteady force on the surface, equal to the pressure jump. The Kirchoff analogy is here considered to propagate the sources to the far-field. In this analogy, acoustic sources are assumed to be located on a control surface and classified as monopole, dipole or quadrupole sources. The integral form of the Kirchoff analogy is given in the frequency domain by Eq. 3.8, where only the dipole sources are considered.

$$p(\mathbf{y},\omega) = \iint_S i\omega\mathscr{F}_i(\mathbf{x},\omega)\frac{\partial\mathscr{G}(\mathbf{y}|\mathbf{x},\omega)}{\partial x_i}\, dS \tag{3.8}$$

with $\mathbf{x} = (x_1, x_2)$ the location of the sources on the control surface S, $\mathbf{y} = (y_1, y_2)$ the observer position and $\mathscr{G}(\mathbf{y}|\mathbf{x},\omega)$ the Green function in the frequency domain. $\mathscr{Q}_n$, $\mathscr{F}_i$ and $\mathscr{T}_{ij}$ respectively

represent the monopole, dipole and quadrupole contributions. In this work, the control surface S is defined by the rigid flat-plate surface and the acoustic sources are assimilated to dipoles of strength $\mathscr{F}_i(\mathbf{x},\omega) = \Delta\hat{P}_T\,(x_1, x_2, \omega)$. Hence, the FWH formulae reduces to:

$$p(\mathbf{y},\omega) = \int_{-L/2}^{+L/2} \Delta\hat{p}_T(x_1, x_2 = 0, \omega)\frac{\partial\mathscr{G}(\mathbf{x}|\mathbf{y},\omega)}{\partial y_2}\,dx_1 \tag{3.9}$$

where the positions of the sources on the aerofoil surface are defined by $\mathbf{x} = (x_1, x_2 = 0)$ and the observer location is given by $\mathbf{y} = (y_1, y_2)$.

In the present work, Amiet's model is modified in order to account for the propagation in a 2D field. To this end, the 2D time harmonic convected Green function for free-field and uniform mean flow is used and described in 3.10 by:

$$\mathscr{G}(\mathbf{x}|\mathbf{y},\omega) = \frac{-i}{4\beta}H_0^{(2)}\left(\frac{k_0}{\beta^2}\sqrt{(y_1 - x_1)^2 + \beta^2 y_2^2}\right)e^{ik_0M(y_1-x_1)/\beta^2} \tag{3.10}$$

with $\beta = \sqrt{1 - M^2}$, $k_0 = \omega/c$ and $H_0^{(2)}$ the Hankel function of the second kind of 0^{th} order.

Considering an observer located in the far-field, the Hankel function and the distance between source and observer can be approximated by [102]:

$$\begin{cases} H_1^{(2)}(z) \approx \sqrt{\frac{2}{\pi z}}e^{-iz+i3\pi/4} \\ \sqrt{(y_1 - x_1)^2} + \beta^2 y_2^2 \approx \sqrt{y_1^2 + \beta^2 y_2^2} = S_0 \end{cases} \tag{3.11}$$

The Green's function derivative can then be approximated by:

$$\frac{\partial G}{\partial y_2}(y_1, y_2, x_1, \omega) \approx -\frac{iy_2}{4}\sqrt{\frac{2k_0}{\pi S_0^3}}e^{-i\frac{k_0}{\beta^2}[S_0 - x_1y_1/S_0 - M(y_1-x_1)] + i\frac{3\pi}{4}} \tag{3.12}$$

Substituting Eq. 3.12 and Eq. 3.7 in Eq. 3.9, a final expression for the radiated pressure is given by:

$$p(\mathbf{y},\omega) = -2\pi\rho U\hat{w}_R(K_c)\frac{iy_2}{4}\sqrt{\frac{2k_0}{\pi S_0^3}}\int_{-L/2}^{+L/2} g(x_1, K_c)e^{-i\frac{k_0}{\beta^2}[S_0 - x_1y_1/S_0 - M(y_1-x_1)] + i\frac{3\pi}{4}}\,dx_1 \tag{3.13}$$

Despite the absence of randomness in the input (prescribed single vortex), the PSD of the far-field radiated pressure is considered to compare the results and defined by:

$$S_{pp} = \frac{1}{T}E\left[p(x, y, \omega)p^*(x, y, \omega)\right] \tag{3.14}$$

with the subscript * indicating the complex conjugate transpose and T the time over which the Fourier Transform of the signal is taken.

The expression of the far-field acoustic pressure PSD, S_{pp} is given by Eq. 3.15, where the coordinate system has been changed to a 2D cylindrical co-ordinate system (r_0, θ) [102]:

$$S_{pp}(r_0, \theta, \omega) = \frac{\pi \rho_\infty^2 (\frac{L}{2})^2 sin^2(\theta) U_\infty k_0}{2 r_0 A(\theta, M)^3} \; \Phi_{ww}(K_c) \mid \mathscr{L}(\theta, K_c) \mid^2 \tag{3.15}$$

where $A = \sqrt{1 - M^2 sin^2(\theta)}$ and $\Phi_{ww}(K_c) = \frac{\pi}{T} E\left[\hat{w}_R(K_c) \hat{w}_R^*(K_c)\right]$ is the one-dimensional wavenumber spectrum of the transverse turbulence velocity component. The function $\mathscr{L}$ is the aeroacoustic transfer function, based on the aerodynamic transfer function g and details are given further below.

3.1.3 Transfer functions

Aerodynamic transfer function g

The expression for the transfer function g introduced in Eq. 3.2 is divided into two contributions $g = g_1 + g_2$. The term g_1 is the main contribution from the leading-edge, obtained by assuming an aerofoil of semi-infinite chord without trailing edge. The term g_2 is a first order correction due to the existence of the trailing-edge, assuming a semi-infinite flat plate with trailing-edge and no leading-edge.

Different aerofoil response functions are used according to the nature of the gust and are detailed in [103]. For a reduced frequency $\mu_a = \frac{\omega b}{c\beta^2} < \pi/4$, the gust is subcritical and the low frequency response function g^{low} has two components g_1^{low} and g_2^{low}, such that $g^{low} = g_1^{low} + g_2^{low}$. The expressions of the two components g_1^{low} and g_2^{low} are given in Eq. 3.16 and Eq. 3.17.

$$g_1^{low}(x_1, K_c) = \frac{e^{-i\pi/4}}{\pi \sqrt{\pi(\bar{x}_1 + 1)(\overline{K}_c + i\beta^2 \kappa')}} e^{\left[(iM\mu + \kappa')(\bar{x}_1 + 1)\right]} \tag{3.16}$$

$$g_2^{low}(x_1, K_c) = -\frac{e^{-i\pi/4}}{\pi \sqrt{2\pi(\overline{K}_c + i\beta^2 \kappa')}} \left\{1 - \text{erf}\left[\sqrt{2\kappa'(x_1 - 1)}\right]\right\} e^{\left[(iM\mu + \kappa')(\bar{x}_1 + 1)\right]} \tag{3.17}$$

where $\overline{x}_0 = x_0/b$, $\overline{K}_c = K_c b$ and erf is the error function defined by $\text{erf}(x) = \frac{2}{\sqrt{\pi}} \int_0^x e^{-t^2} \, dt$ and where

$$\begin{aligned} &\overline{x}_0 = 2x_0/L, \quad && \overline{K}_c = K_c L/2, \quad && \mu = \overline{K}_c M/\beta^2 \\ &\kappa^2 = \mu^2, && \kappa' = -i\kappa \end{aligned}$$

For $\mu_a > \pi/4$ however, the gust wavefronts pass along the aerofoil leading-edge faster than the speed of sound. In this case, the gust is said to be supercritical and a high frequency response function g_{high} is used [10] with g_1^{high} and g_2^{high} given by:

$$g_1^{high}(x_1, K_c) = \frac{e^{-i\pi/4}}{\pi\sqrt{\pi(\bar{x}_1+1)(\bar{K}_c+\beta^2\kappa)}} e^{-i[(\kappa-M\mu)(\bar{x}_1+1)]} \tag{3.18}$$

$$g_2^{high}(x_1, K_c) = \frac{e^{-i\pi/4}}{2\pi\sqrt{\pi(\bar{K}_c+\beta^2\kappa)}} \left\{1-(1+i)E^*\left[2\kappa(1-\bar{x}_1)\right]\right\} e^{-i[(\kappa-M\mu)(\bar{x}_1+1)]} \tag{3.19}$$

where E^* the conjugate of the Fresnel integral defined by:

$$E(x) = C(x) + iS(x) = \int_0^x \frac{e^{it}}{\sqrt{2\pi t}}\, dt \tag{3.20}$$

Aeroacoustic transfer function $\mathscr{L}$

The radiation function $\mathscr{L}$ introduced in Eq. 3.15 represents the chordwise integral of the surface loading g and is defined by:

$$\mathscr{L}(\theta, K_c) = \frac{1}{b}\int_{-L/2}^{L/2} g(x_1, K_c) e^{i\frac{k_0}{\beta^2}\left(\frac{cos(\theta)}{A(\theta,M)}-M\right)(x_1+b)+i\frac{3\pi}{4}}\, dx_1 \tag{3.21}$$

For a subcritical gust ($\mu_a < \pi/4$), the aeroacoustic transfer function is given by:

$$\mathscr{L}^{low}(\theta, K_c) = \frac{S(\mu_h)}{\beta} e^{i\mu_h f(M)} \left[J_0(\mu_a \frac{cos(\theta)}{A(\theta,M)}) - iJ_1(\mu_a \frac{cos(\theta)}{A(\theta,M)})\right] \tag{3.22}$$

where J_0 and J_1 are the Bessel functions of the first kind or order 1 and 2, S is the Sears function and $f(M) = (1-\beta)\ln(M) + \beta\ln(1+\beta) - \ln(2)$.

For a supercritical gust ($\mu_a > \pi/4$), the aeroacoustic transfer function is given by the sum of $\mathscr{L}_1^{high}$ and $\mathscr{L}_2^{high}$:

$$\mathscr{L}_1^{high}(\theta, K_c) = \frac{\sqrt{2}}{\pi\beta\sqrt{\mu_h(1+M)\theta_1}} E^*(2\theta_1) e^{i\theta_2} \tag{3.23}$$

$$\mathscr{L}_2^{high}(\theta, K_c) = \frac{e^{i\theta_2}}{\pi\theta_1\beta\sqrt{2\pi\mu_h(1+M)}} \left[i(1-e^{-2i\theta_1}) + (1-i)\times\left[E^*(4\mu_a\beta^2) - \sqrt{\frac{2}{1+\frac{cos(\theta)}{A(\theta,M)}}} e^{-2i\theta_1} E^*(2\theta_3)\right]\right] \tag{3.24}$$

where θ_1, θ_2 and θ_3 are given by:

$$\begin{cases} \theta_1 = \mu_a(1 - \frac{cos(\theta)}{A(\theta,M)}) \\ \theta_2 = \beta^2\mu_h + \mu_a(M - \frac{cos(\theta)}{A(\theta,M)}) - \frac{\pi}{4} \\ \theta_3 = \mu_a(1 + \frac{cos(\theta)}{A(\theta,M)}) \end{cases} \tag{3.25}$$

In this study, the prescribed spanwise vortex has its wavefronts parallel to the aerofoil leading edge since the spanwise wavenumbers equal 0. Therefore, it travels along the leading-edge with infinite phase speed and can be considered as supercritical. Additionally, since a semi-infinite chord is considered is the computational method, there is no trailing-edge and the transfer functions g and $\mathscr{L}$ will therefore be reduced to $g = g_1^{high}$ (Eq. 3.18) and $\mathscr{L} = \mathscr{L}_1^{high}$ (Eq. 3.23).

3.2 Computational setup

3.2.1 Description of the problem

The numerical validation study is performed on a semi-infinite flat plate with zero thickness being impacted by a vortical disturbance injected upstream of the aerofoil. A uniform mean flow velocity is assumed with free stream Mach number set to $M = 0.3$, oriented in the chordwise x_1-direction, with x_2 the direction normal to the plate and x_3 the spanwise direction. The aerofoil chord is effectively semi-infinite by extending further downstream the no-slip (no-penetration) boundary conditions implemented on the flat-plate. This condition allows the removal of trailing edge interaction noise. Periodic boundary conditions are applied across the spanwise boundary planes of the flat plate. The total plate span is therefore effectively infinite. The situation is depicted in Fig. 3.2. Note that all positions and lengths are normalised by unit length and all velocities are normalised by the speed of sound.

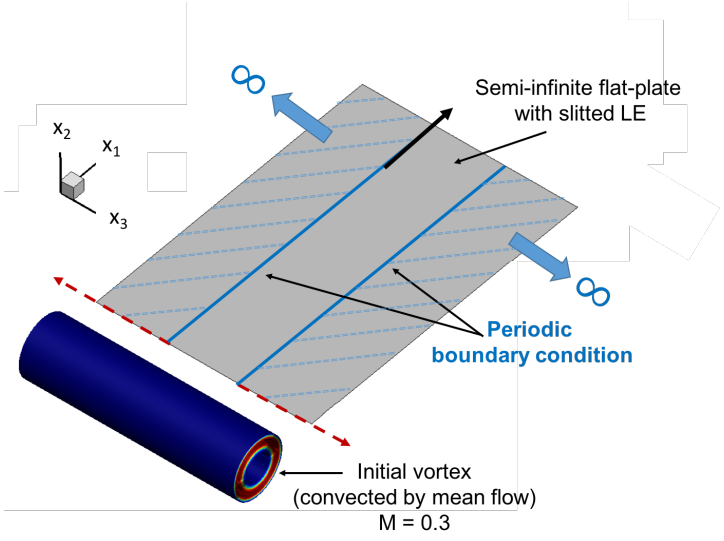

FIGURE 3.2: Sketch of the flat-plate problem

3.2.2 Synthetic prescribed vortex

The vortical disturbance impinging on the flat plate is modelled as a single spanwise vortex injected upstream of the plate as an initial field. The vortex model is based on the Gaussian eddy profile used in the synthetic turbulence model proposed by [104] and [105]. The vortex-induced velocity field at point in the field $\mathbf{x} = (x_1, x_2, x_3)$ is determined by taking the curl of a vector potential shape function $\psi(\mathbf{x})$ ($\mathbf{u}'(\mathbf{x}, t = 0) = \nabla \times [\psi(\mathbf{x})\mathbf{e}_z]$), where $\mathbf{e}_z$ is a unit vector in the spanwise direction. This ensures that the vortex is divergence-free, which is essential to avoid the production of spurious noise. The Gaussian shape function ψ is described in Eq. (3.26), where c is the speed of sound, and is completely defined by the two parameters $\sigma_{vortex} = 0.001$ and $\epsilon_{vortex} = 0.24$, which control the vortex size and strength respectively. These parameters give a vortex velocity amplitude close to 2% of the mean flow to minimise non-linear propagation effects.

$$\psi(\mathbf{x}) = c\frac{\epsilon_{vortex}}{\sqrt{\sigma_{vortex}}} \exp\Big(-\big[3\sigma_{vortex} r^2(\mathbf{x})\big]^2\Big), \qquad r^2(\mathbf{x}) = (x_1 - x_0)^2 + x_2^2 \tag{3.26}$$

Taking the curl of the shape function defined in Eq. (3.26) gives the following expressions for the streamwise and transverse components, $\mathbf{u}$ and $\mathbf{v}$ of the initial velocity field, given in Eq. (3.27), where $x_0 = -1.355$ is the prescribed initial position of the vortex core and $x_{\mathrm{LE}} = -0.5$ the location of the plate leading-edge.

$$\left.\begin{aligned} \mathbf{u}(\mathbf{x}, t = 0) &= U - 36\sigma^2 x_2 r(\mathbf{x})\psi(\mathbf{x}) \\ \mathbf{v}(\mathbf{x}, t = 0) &= 36\sigma^2 (x_1 - x_0) r(\mathbf{x})\psi(\mathbf{x}) \end{aligned}\right\} \tag{3.27}$$

In this study the incoming disturbance is modelled by a single 2D spanwise vortex whose velocity components are therefore identical along the span. The limitation with this 2D approach is that the effects of spanwise correlation and the stochastic features of the incoming turbulence are not included. However, the 2D vortex has the significant advantage that it allows secondary vortices to be easily identified, its frequency spectrum is smoothly varying, and does not require time averaging. The use of a single vortex therefore allows one to focus on the fundamental slit response. The essential difference between incoming turbulent flow and the single vortex assumed in this thesis is that in the case of turbulence the surface pressure response between adjacent slits is likely to be partially coherent while it is perfectly coherent for a single 2D incoming vortex. Furthermore, it is anticipated that the effect of turbulence length scale on the noise reductions will be small when the slit width is smaller than the turbulence length scale. The essential noise reduction mechanism for each slit is therefore identical in both cases. The transverse velocity profile (normal to the plate) of the initial vortex, along the centre-line is plotted in Fig. 3.3 versus non-dimensional streamwise position x_1. The vortex is assumed to rotate in the clockwise direction as it convects downstream. The vortex can be seen to first generate a downward stroke as it encounters the flat plate, followed by an upward stroke with identical velocity. As the vortex convects over the flat plate, positive pressure is generated during the downward stroke on the upper side of the plate followed by negative pressure during the upwards stroke, with the

opposite behaviour occurring on the lower side.

The Power Spectral Density $\Phi_{vv}(\omega)$ of the transverse velocity fluctuation v defined in Eq. (3.27) is plotted in Fig. 3.3 versus non-dimensional frequency $f\Lambda/U$, where Λ is the radius of the vortex, based on the assumption that the eddy convects as a frozen pattern with mean flow speed U. It is noted that even though the vortex shape is unbounded and decays exponentially from its centre, it will be shown to be useful to define the effective radius of the vortex Λ in a manner consistent with the integral length scale for turbulence, given by Eq. (3.28). The leading edge of the vortex is therefore assumed to be located at Λ from the vortex centre, which is the initial position of the vortex, referred to as $x_0 = -1.355$ in Eq. (3.28).

$$\Lambda = \frac{1}{\max|v(x_1)|}\int_{x_0}^{x_0+\infty}|v(x_1)|\mathrm{d}x_1 \quad \text{at} \quad x_2 = x_3 = 0, t = 0 \tag{3.28}$$

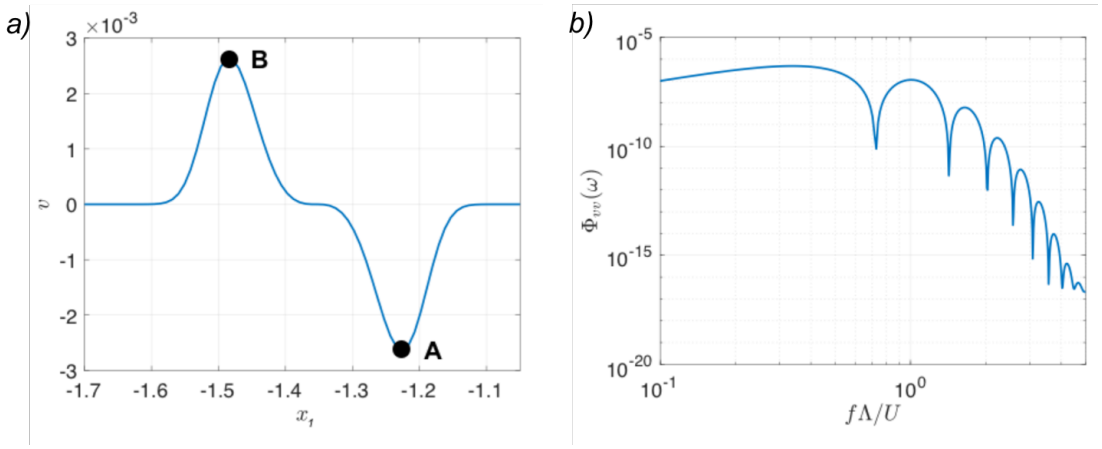

FIGURE 3.3: Prescribed vortex velocity at $t = 0$ (a) and power spectral density of the transverse velocity fluctuation versus non-dimensional frequency (b). Point A and point B indicate the location of maximum downwash and maximum upwash respectively

3.2.3 Wall pressure and far-field radiation

The wall pressure generated by the vortical disturbance on the flat-plate and the corresponding far-field radiation is determined by using the 3D compressible Euler time-domain solver presented in Chapter 3. Viscosity effects are therefore neglected in these simulations. Note that viscosity effects are assumed to be negligible at the leading-edge where the boundary layers are thin.

The simulation is realised with a total of 963 × 802 × 41 grid cells in the x_1, x_2 and x_3 directions respectively, corresponding to a total of 31 665 366 grid cells in the domain, which are shared over 480 processor cores for parallelisation purposes. In the present analysis, the chosen grid is Cartesian, with a clustering of points at specific regions of the computational domain to capture the main important features of the flow. The grid spacing is reduced upstream of the aerofoil to resolve adequately the vortex with at least 25 points across the vortex radius,

but stretched in regions where the flow is fully developed to balance the use of computational resources. Grid points are clustered around the flat-plate leading-edge with the smallest grid size $\Delta x_1^{min} = \Delta x_2^{min} = 0.00625L$. Table 3.1 gives the parameters of the computation as well as the domain size, defined as ($[x_{min}\ x_{max}]$,

This section will present a comparison of the predicted noise with the 2D formulation of Amiet. The power spectral density (PSD) and sound pressure level spectrum (SPL) are defined by Eq. 3.29, with $p_{ref} = 2.10^{-5}Pa$ the reference pressure.

$$SPL(\mathbf{x},\omega) = 10\log_{10}(\frac{S_{pp}(\mathbf{x},\omega)}{p_{ref}^2}), \qquad S_{pp}(\mathbf{x},\omega) = \frac{1}{T}E\left[p(\mathbf{x},\omega)p^*(\mathbf{x},\omega)\right] \tag{3.29}$$

The fluctuating signals are extracted at a particular position directly from the nodes value or by a linear interpolation of neighbouring nodes values when no grid point are available at the observer position.

3.2.4 Pressure jump along the aerofoil

The fluctuating wall pressure jump Δp_w is defined by:

$$\Delta p(\mathbf{x},t) = p(x_1, x_2 = 0^+, x_3, t) - p(x_1, x_2 = 0^-, x_3, t) \tag{3.30}$$

with $x_2 = 0^+$ and $x_2 = 0^-$ respectively indicating the upper and lower surfaces of the flat plate.

As the aerofoil leading-edge is at the intersection of more than two blocks, its value is calculated by averaging between the blocks at the leading-edge junction. This point is therefore excluded from the calculations without affecting the results. Fig. 3.4 displays the fluctuating pressure on the upper & lower surfaces one grid point aft of the leading-edge, as well as the corresponding pressure jump at this point. An upward pulse followed by a downward pulse can be seen to be generated on the aerofoil upper surface, which is consistent with the prescribed clockwise velocity profile (Fig. 3.3).

The magnitude $|\Delta\hat{p}(x_1,\omega)|$ and phase Φ_{jump} of the pressure jump along the aerofoil provide information about the acoustic source strength and the speed at which the acoustic waves travel. The phase is defined by:

$$\Phi_{jump}(x,\omega) = \tan^{-1}\left[\frac{Im(\Delta\hat{p}(x_1,\omega))}{Re(\Delta\hat{p}(x_1,\omega))}\right] \tag{3.31}$$

where $\Delta\hat{p}(x_1,\omega)$ the Fourier transform of the wall pressure fluctuations difference.

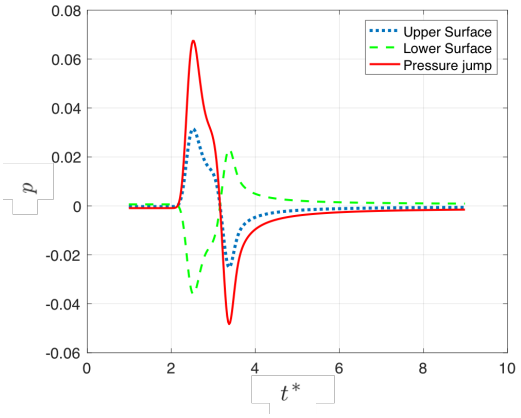

FIGURE 3.4: Fluctuating pressure on the flat-plate surface - measured one grid point after the LE

3.2.4.1 Magnitude of the pressure jump

The magnitude of the pressure jump along the aerofoil is plotted against predictions from Amiet's model in Fig. 3.5 at a single non-dimensional frequency $fL/c = 1.5$, where $L = 1$m. According to Amiet's model, the pressure jump is infinite at the leading-edge and reaches zero at the trailing-edge to satisfy the Kutta condition. In the present case, the chord is semi-infinite in the trailing-edge direction, which explains why both predictions give a non-zero value at $x_1/L = 0.5$.

Good overall agreement with Amiet's model is observed, with maximum pressure jump magnitudes found near the leading-edge region and a decaying profile. Some oscillations are visible from the leading-edge until about 10% of the chord. These oscillations are attributed to numerical errors and directly linked to the mesh used on the aerofoil surface (blocks 1 and block 4 on Fig. 2.1), with one complete oscillation extending for 3 mesh cells. As it will be shown further below, this mesh provides a good enough approximation of Amiet's model to validate the numerical method used. However, an improved finer mesh will be used for the slitted leading-edge investigation and is presented in Chapter 4.

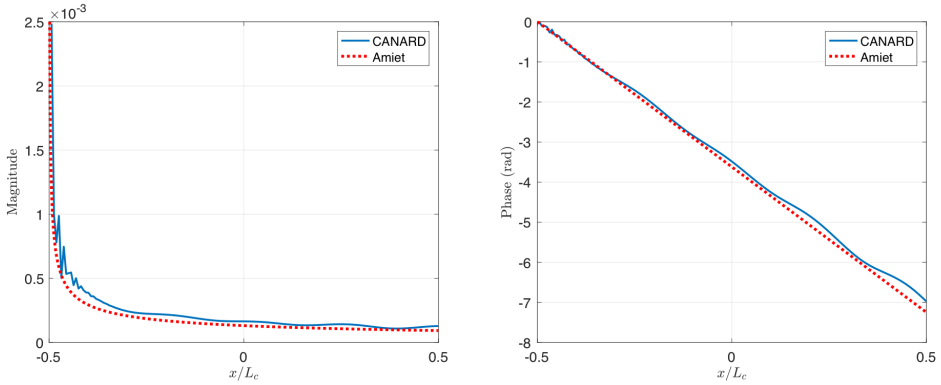

FIGURE 3.5: Magnitude and phase of the pressure jump along the aerofoil - $fL/c = 1.5$

3.2.4.2 Phase of the pressure jump

The phase of the pressure jump along the aerofoil is plotted against predictions from Amiet's model in Fig. 3.5 at a non-dimensional frequency $fL/c = 1.5$. Good agreement with Amiet's solution is obtained. The phase of the pressure jump can be used to determine the speed at which ΔP propagates along the chord. The phase variation across the flat plate is consistent with a wave traveling downstream at a speed of $c + U$, indicating that the response of the flat plate is of the form of an acoustic wave superimposed on the mean flow.

3.2.5 Far-field radiated pressure and directivity

Far-field radiated pressure

The fluctuating far-field pressure is extracted from the computational domain for an observer located at a position $(y_1, y_2, y_3) = (0, 5, 0)$. There are 400 samples extracted over a non-dimensional time interval $0 < t^* < 12$. The extracted far-field radiated pressure signal and its PSD are shown in Fig. 3.6. The radiated pressure field compares well with predicted values from Amiet's model up until a non-dimensional frequency f* ≈ 5.*Thediscrepanciesobservedinthespectradecayafterthisfrequencyareattribute* 5, the mesh is most likely too coarse to resolve accurately higher frequencies. It is again noted that an improved finer mesh will be used for the slitted leading-edge investigation and is presented in Chapter 4.

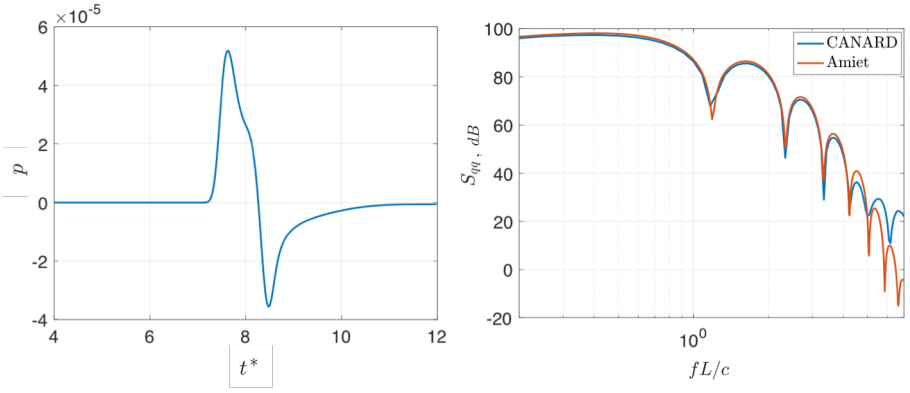

FIGURE 3.6: Far-field radiated time-pressure signal and its PSD for an observer located at $(y_1, y_2, y_3) = (0, 5, 0)$

Oscillations are present in the spectra, owing to the finite of the incident vortex. These oscillations therefore occur with periodicity of frequency equal to U/Λ. Fig. 3.7 shows the SPL pressure now normalised by the vortex velocity spectrum.

A $1/f$ dependence is observed in Fig. 3.7 after normalizing the far-field noise by the vortex velocity spectra. The reason for this behaviour can be explained by dimensional analysis of Eq. 3.15 for the high frequencies. As the far-field radiated noise has been normalized by the vortex velocity spectra in Fig. 3.7, the dimensional analysis is performed on S_{pp}/Φ_{ww}.

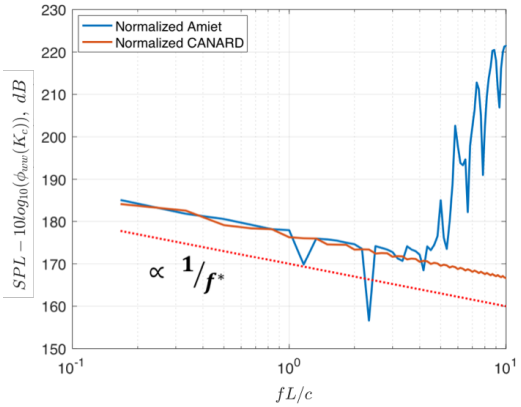

FIGURE 3.7: SPL of the far-field radiated noise normalized by the vortex velocity spectra for an observer position $(y_1, y_2, y_3) = (0, 5, 0)$

The first factor in Amiet's prediction formula (Eq. 3.15) only depends on f by the term $k_0 = 2\pi f/c$. The following dependency can therefore be written:

$$\frac{\pi\rho_0^2 b^2 U k_0 sin^2(\theta)}{2r_0 A^3(\theta, M)} \propto \quad k_0 \quad \propto f \tag{3.32}$$

The aeroacoustic transfer function $\mathscr{L}$ (Eq. 3.23) depends on f by the terms μ_h, μ_a and θ_1, all proportional to the frequency. Additionally, since the predictions are performed using a semi-infinite chord ($b \to \infty$), the term $\mu_a = \frac{\omega b}{c\beta^2} \to \infty$ and the Fresnel integral $E^*(2\theta_1)$ converges to a value independent of frequency.

$$\mathscr{L}_1^{high}(\theta, k_x) = \frac{\sqrt{2}}{\pi\beta\sqrt{\mu_h(1+M)\theta_1}} E^*(2\theta_1) e^{i\theta_2} \quad \underset{f\to+\infty}{\longrightarrow} \quad \frac{cst(\theta, k_x)}{\sqrt{\mu_h\theta_1}} \quad \propto \frac{1}{f} \tag{3.33}$$

Combining Eq. 3.32 with 3.33 and using Eq. 3.15, the proportionality to f^{-1} is recovered, consistent with Amiet's prediction.

$$S_{pp}/\Phi_{ww} \quad \underset{f\to+\infty}{\longrightarrow} \quad cst(\theta, k_x) \;\; f \;\; \frac{1}{f^2} \quad \propto \frac{1}{f} \tag{3.34}$$

Directivity

The observer is located in the plane $z = 0$. The directivity is obtained by extracting the fluctuating pressure at 101 equidistant points located on a circle centred on $(x, y, z) = (0, 0, 0)$ with a radius of 2.5 chords. Fig. 3.8 displays the directivity at two non-dimensional frequency $f^* = 1.5$ and $f^* = 3$ and shows a good agreement with Amiet's model.

The computational method is therefore validated and used in the following chapters to predict interaction noise.

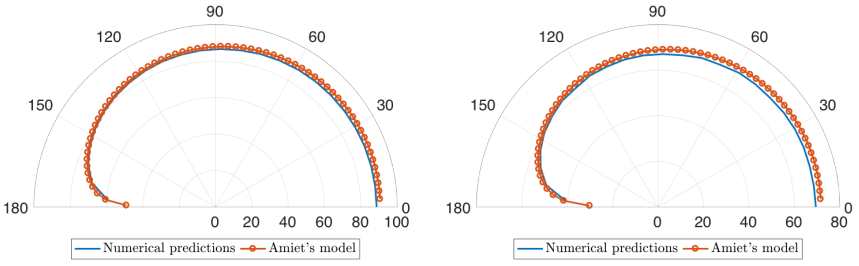

FIGURE 3.8: Directivity of the far-field radiated noise for an observer located in the plane $x_3 = 0$ at a radius $r = 5$ from the centre of the flat plate: a) $fL/c = 1.5$ - b) $fL/c = 3$

Chapter 4

Physical mechanisms of slitted leading-edge profiles: source distribution of the aerofoil surface

This chapter focuses on a numerical study into the characteristics and mechanism of the noise reduction due to slitted leading edges interacting with a single spanwise vortex, using the same numerical method presented in Chapter 2 and 3. The surface pressure fluctuations generated on the slitted flat-plate and the far-field radiated noise are analysed in detail and compared to results obtained with a straight leading-edge. The vortex dynamics is explored in great detail as well as a detailed investigation into the resulting unsteady surface pressure distribution. Special attention is paid to the identification of the noise reduction mechanism. A description of the serration geometry is first provided, followed by the details on the computational procedure used in the investigation. The source distribution in the vicinity of the slit and its generation mechanism will be analysed.

4.1 Serration geometry and computational setup

4.1.1 Description of the problem

The numerical study is performed on the same semi-infinite flat plate described in Chapter 3, with the uniform mean flow velocity still set to $M = 0.3$. A rectangular slit has been introduced onto the flat-plate leading-edge by applying the no-slip boundary condition to the grid points located on the edges of the slit where all velocity components vanish. The situation is depicted in Fig. 4.1 indicating a rectangular slit of width w along the x_3-direction and length h along the x_1-direction, with x_2 the direction normal to the plate. As periodic boundary conditions are applied across the spanwise boundary planes of the flat plate separated by λ, the total plate span is therefore effectively infinite so that the slit is repeated every wavelength λ. All positions and lengths are normalised by unit length and all velocities are normalised by the speed of sound.

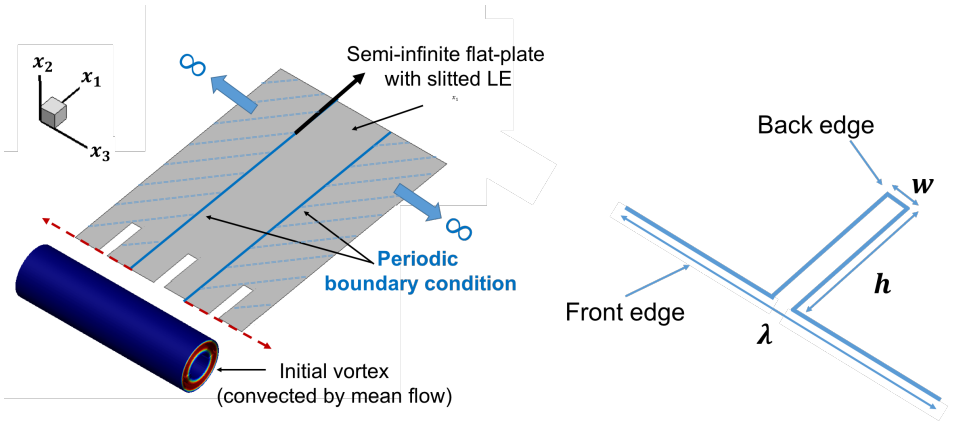

FIGURE 4.1: Sketch of the current problem (the red dotted arrow indicates periodic boundary conditions in the spanwise direction)

This chapter focuses on a representative slit configuration based on typical dimension ratios investigated experimentally by Chaitanya et al [4]. It has a slit aspect ratio of $h/w = 33$ with $\lambda/w = 10$, where w is determined by the periodic boundary condition. These parameters capture the essential physics of the noise reduction mechanism.

4.1.2 Computational setup

4.1.2.1 Surface pressure fluctuations

The wall pressure generated by the vortical disturbance on the flat-plate is determined by solving the 3D compressible Euler time-domain solver, as described in Chapter 2 and 3. Viscosity effects are therefore neglected in these simulations. This inviscid hypothesis has been assumed in all previous numerical investigations into the noise reductions due to serrated leading edge profiles, for example ([48, 81, 88, 105]). For the particular case of the narrow slit, viscosity is likely to have some influence on the behaviour of the flow in the vicinity of the slit. However, it will be demonstrated that this inviscid simulation provides good qualitative agreement with the noise reductions obtained experimentally in Fig. 1.7, thereby demonstrating that the simulation is capable of capturing the essential noise reduction mechanisms.

The numerical procedure used to determine the surface pressure fluctuations is identical to the one described in Chapter 3. However, the grid has been modified in an effort to capture the main characteristics of the physical mechanisms, with a greater refinement in all directions near the slit. In the spanwise x_3-direction, grid points are clustered around the slit corner with the smallest grid size $\Delta x_3^{min} = 0.001h$ and at least 30 points are used inside the slit in the spanwise direction. The grid is also refined in the streamwise (x_1) and transverse (x_2) directions, with the smallest cells located at the slit corners of size $\Delta x_1^{min} = \Delta x_2^{min} = 0.003h$. Finally, a total of 301 equidistant points are used along the slit streamwise edge to capture the development of secondary streamwise vortices. The grid parameters were chosen following a thorough grid convergence study on the number of points required inside the slit and around the slit corners to obtain a converged solution. The fine mesh used in this study is due to the need to resolve

the detailed behavior of the secondary vortex system described in Section 4.2. The simulation is realised on a total of 802 × 602 × 101 grid cells in the x_1, x_2 and x_3 directions respectively, corresponding to a total of 48, 763, 204 grid cells in the domain, which are shared over 480 processor cores.

Similar to Chapter 3, the numerical method is validated by computing and comparing the predicted pressure jump across a flat plate with Straight Leading Edge (SLE) with Amiet's formulation. The predictions in time were Fourier Transformed to determine the magnitude and phase of the pressure jump at a single non-dimensional frequency $fL/c = 1.5$, where $L = 1$m, and the results plotted in Fig. 4.2 against non-dimensional distance x_1 plotted on a logarithmic scale. Also shown in this figure is the predictions obtained from Amiet's model [10] of leading edge noise from a flat plate, by allowing the chord length to go to infinity. Note that since the aerofoil chord is essentially infinitely long, no trailing-edge correction was applied. Good overall agreement between the numerical and analytic predictions is observed.

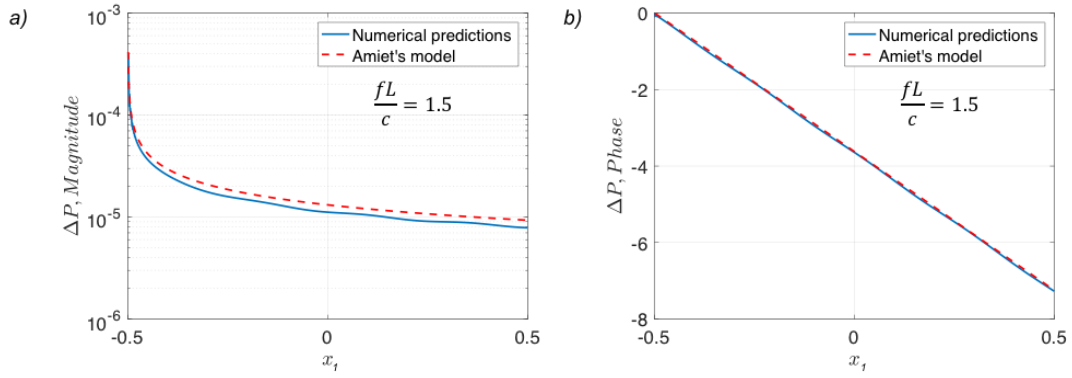

FIGURE 4.2: Surface pressure fluctuations for a baseline SLE case compared with Amiet's model: a) Magnitude - b) Phase

4.1.2.2 Far-field radiation

Due to the refinement used on the surface, the computational domain has been reduced to $([x_{min}\ x_{max}], [y_{min}\ y_{max}]) = [-4\ 4], [-4\ 4]$ for balancing the computational resources needed and reducing the simulation time. In order to calculate the far-field radiation, a FWH calculation has been used and is described further below.

The far-field radiation as a function of time $p(\mathbf{x}, t)$ at any observer $\mathbf{x}$ is determined directly by the integration of the fluctuations in pressure jump $\Delta p(\mathbf{y}, \tau)$ at all point $\mathbf{y}$ across the aerofoil surface, assuming dipole radiation into free space with uniform mean flow and is therefore of the form,

$$p(\mathbf{x}, t) = -\frac{1}{2\pi} \iint_S \left[\Delta p(\mathbf{y}, \tau) \frac{\partial}{\partial y_2} G(\mathbf{x}, t|\mathbf{y}, \tau) \right] \mathrm{d}S(\mathbf{y}) \tag{4.1}$$

where $G(\mathbf{x}, t|\mathbf{y}, \tau)$ is the 3D time-domain Green function between a source point $\mathbf{y}$ at source time τ and an observer at $\mathbf{x}$ at receiver time t given by,

$$G(\mathbf{x}, t|\mathbf{y}, \tau) = -\frac{\delta(\tau - t + \tau^*)}{4\pi r_\beta} \quad ; \quad \tau^* = \frac{r_\beta - M r_1}{c\beta^2} \tag{4.2}$$

in which $r_\beta = \sqrt{(x_1 - y_1)^2 + \beta^2(x_2 - y_2)^2 + \beta^2(x_3 - y_3)^2}$ represents the flow-corrected acoustic distance and $r_1 = |x_1 - y_1|$.

Finally, assuming far field observers the distance r_β is taken outside of the surface integral and replaced by $\sigma = \sqrt{x_1^2 + \beta^2(x_2^2 + x_3^2)}$. In the far field r_β can be approximated by $r_\beta \approx \sigma - \frac{x_1 y_1 + \beta^2 x_3 y_3}{\sigma}$ in the expression for the time delay τ^*, and near field terms of second order in r_β^2 can be neglected. The final expression for the acoustic pressure at an arbitrary far field observer can be expressed by Eq. (4.3).

$$p(\mathbf{x}, t) = -\frac{x_2}{4\pi c \sigma^2} \iint_S \left[\frac{\partial \Delta p(\mathbf{y}, \tau)}{\partial \tau}\right]_{\tau = t - \tau^*} \mathrm{d}S(\mathbf{y}) \tag{4.3}$$

where the pressure jump is evaluated at the retarded time $\tau = t - \tau^*$.

In order to validate the method, the far-field radiation of a baseline SLE case is calculated with the FWH calculation using the surface pressure fluctuations presented above in Fig. 4.2. Figure 4.3 a) shows that the far-field time signal obtained by propagating the surface pressure to the position $(y_1, y_2, y_3 = (0, 5, 0))$ compares very well with the time signal directly obtained in Chapter 3 in Fig. 3.6. Additionally, Fig. 4.3 b) represents a comparison of its PSD with Amiet's model and shows a very good agreement in the decay for all frequencies, with discrepancies in the amplitude from $fL/c = 5$. The reduction in the spectra amplitude from this frequency is attributed to the sampling number in the time signal, allowing 6.6 points in time to resolve an oscillation with $fL/c = 5$ (or period of 0.2). The directivity at a radius $r = 5$ is also compared with Amiet's model for two frequencies $fL/c = 1, 5$ and $fL/c = 3$ in Fig. 4.4 and also shows a very good agreement, with a slight reduction of less than 1dB for both frequencies.

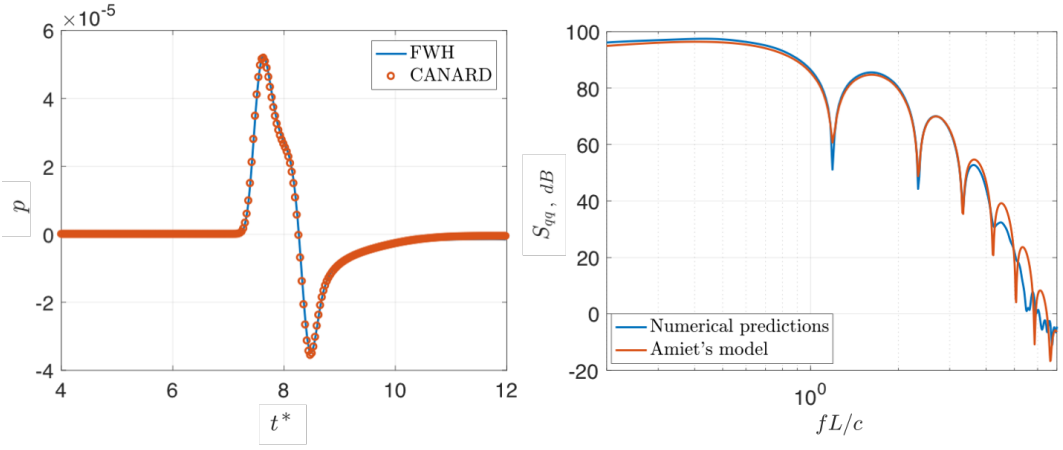

FIGURE 4.3: a) Comparison of the far-field time signal obtained at $(y_1, y_2, y_3 = (0, 5, 0))$ using CANARD code and FWH propagation - b) Far-field radiation spectra obtained using FWH calculation compared with Amiet's model

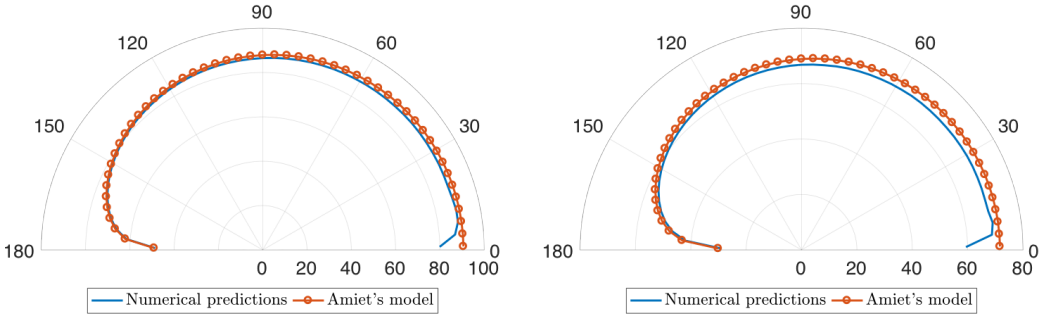

FIGURE 4.4: Far-field directivity obtained using FWH calculation, compared with Amiet's model: a) $fL/c = 1.5$ - b) $fL/c = 3$

4.1.3 Grid convergence study

A grid convergence study has been conducted to determine and validate the discretisation needed for slitted leading-edge profiles to obtain a stable numerical solution. Results are based on the quantity of interest for the present study, namely the wall pressure generated at the front and back-edge regions of the slit, which will be compared both in time domain and frequency domain. The study focuses in particular on the number of points required inside the slit, as well as around the slit corners. Additionally, the sensitivity on the streamwise spacing along the slit edge and on the transverse spacing is studied.

4.1.3.1 Number of points inside the slit

The influence of the number of points inside the slit on the wall pressure generated at the end of slit has been studied for a number of points varying from $N_{slit} = 15$ to $N_{slit} = 50$. A number of points inferior to $N_{slit} = 10$ produces high oscillations near the slit, causing the code to become unstable. The wall pressure time signal and its PSD generated at the back-edge of the slit are represented on Fig. 4.5 a) and b) for the different cases.

With less than 1 dB deviation obtained between the different cases, these figures show that no effective difference is observed, both in time and frequency domain, from $N_{slit} = 30$. The numerical solution is therefore stable enough and 30 points inside the slits will be used for the study.

4.1.3.2 Number of points around the slit corner

The influence of the number of points around the slit corner on the wall pressure generated at the leading-edge has been studied for different stretching of the grid in the spanwise direction. The quantity N_{corner} defines the number of points available around the slit corner, equally spaced at a Δx_3 equal to the spacing inside the slit, before stretching the grid towards the spanwise

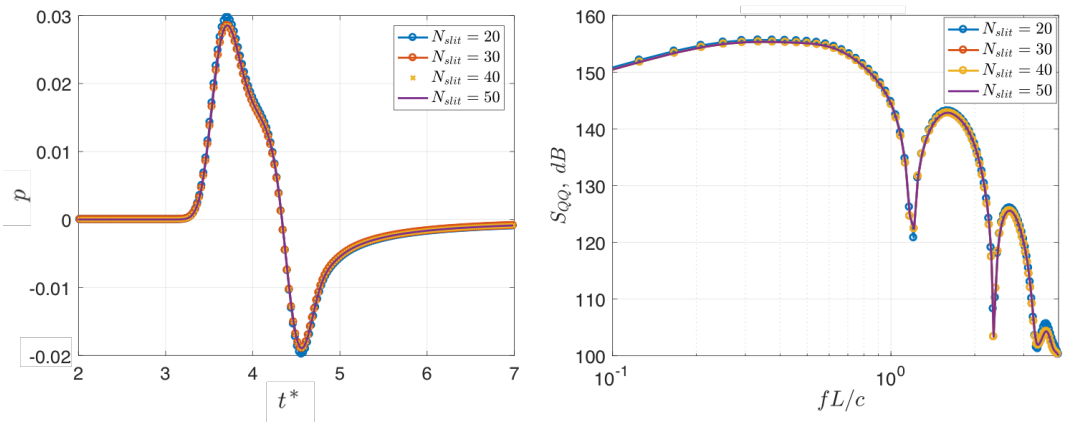

FIGURE 4.5: Influence of the number of points inside the slit N_{slit}: wall pressure time signal (a) and its PSD (b) generated at the back-edge of the slit for different N_{slit}

boundaries. The RMS pressure along the front-edge is represented on Fig. 4.6 for the different cases. For a more detailed comparison, the PSD of the wall pressure time signal generated at two different positions along the front-edge region is represented on Fig. 4.7 for the different cases.

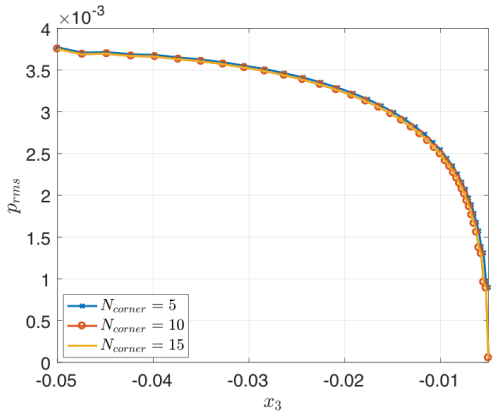

FIGURE 4.6: Influence of number of points around the corner of the slit: RMS of the wall pressure time signal generated along the front-edge region for different N_{corner}

With a difference inferior to 0.5 dB between the different cases, it can be concluded that a stable pressure profile is obtained at the front-edge region for different number of points around the slit corners, for $N_{corner} > 5$. The quantity $N_{corner} = 10$ is therefore chosen for the study.

4.1.3.3 Streamwise spacing along the slit edge and transverse spacing

The grid convergence study is completed by a study concerning the sensitivity on the streamwise spacing along the slit edge and on the transverse spacing used near the flat-plate. Three different levels of grid resolution are compared: the current grid used in the investigation and two levels obtained by refining/coarsening the grid by 20% in the x_1/x_2 plane. Results concerning the wall pressure generated at the back-edge region are represented in time and frequency domain in Fig. 4.8 a) and b) respectively.

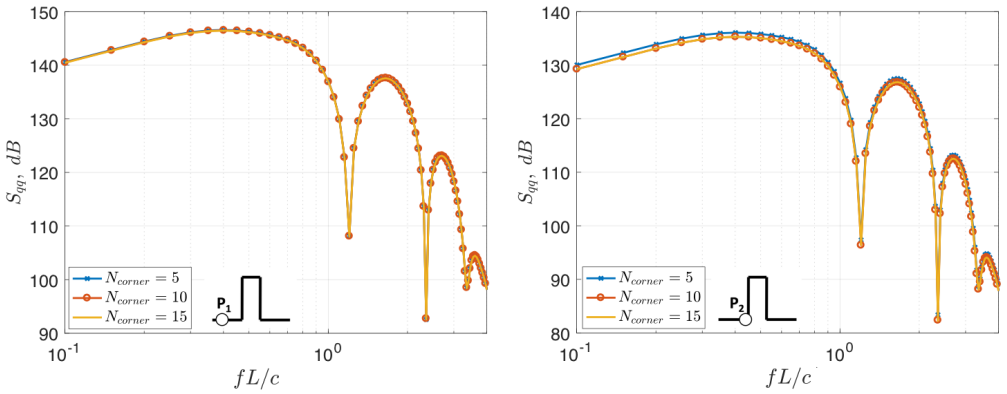

FIGURE 4.7: PSD of the wall pressure time signal generated at two different positions P_1 and P_2 along the front-edge region for different N_{corner}: a) P_1 close to the spanwise boundary - b) P_2 close to the slit corner

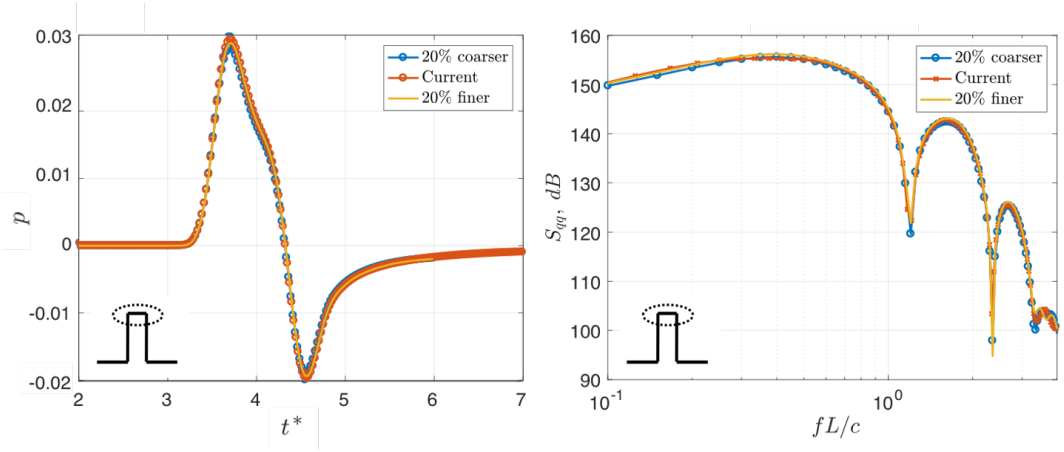

FIGURE 4.8: Wall pressure time signal (a) and its PSD (b) generated at the back-edge of the slit for three different levels of grid resolution

No effective difference in the time signals and spectra obtained with the three different levels is obtained, with a maximal deviation of 0.5 dB.

4.1.3.4 Grid parameters chosen for the investigation

The following parameters are retained to build the grid for the parametric investigation, with N_{x_1} the number of points along the flat-plate in block 1 and block 4 from Fig. 2.1.

TABLE 4.1: Grid resolution for the slitted flat-plate configuration

N_{slit}	N_{corner}	Δx_1^{min}	Δx_2^{min}	N_{x_1}
30	10	0.001	0.001	601

4.2 Source distribution on the flat-plate

4.2.1 Wall pressure fluctuations on the surface

For the purposes of understanding the noise reduction mechanism this section focuses on the time variation of pressure generated on the aerofoil surface as the vortex convects across the plate. Contour plots of the pressure generated on the slitted and baseline aerofoil surfaces are shown in figures 4.9(a - f) corresponding to three instances in time during the passage of the vortex.

In this simulation the length of the slit was chosen so that $h/2\Lambda$=0.91. The first snapshot in time shown in Fig. 4.9(a) was chosen to correspond to when the maximum downwash velocity due to the vortex, identified as A in Fig. 3.3(a), reaches the front edge of the slitted flat plate. Also shown in Fig. 4.9(d) for comparison is the corresponding surface pressure distribution for the baseline aerofoil. The distribution of the surface pressure due to the slit can be clearly seen to more localised towards the leading edge than the baseline case. A strong span-wise pressure variation is now evident with the pressure dropping to very low values near the edges of the slit. The overall effect of the slit is therefore to provide a reduction in the integrated source strength, which will be considered in greater detail below.

The second snapshot of time considered here corresponds to when the effective leading edge Λ of the vortex just arrives at the back edge of the slit so that the slit front edge simultaneously interacts with the vortex trailing edge. Highly localised, high intensity pressure fluctuations can be observed at the back edge of the slit. The level of pressure fluctuation in this region is significantly higher than the pressure fluctuation near the leading edge of the baseline aerofoil, which will be shown in Chapter 5 to contribute to the far field noise reduction. There therefore exists a range of angles for which the sound radiation from the front and back regions interfere destructively, leading to enhanced noise reductions. The conditions for destructive interference will be investigated in detail in Chapter 5. However, as confirmed at the end of Chapter 5 the condition for destructive interference does not require the slit length to be shorter than the vortex size or length scale in the case of incoming turbulence.

Finally, the third snapshot in time considered here, plotted in Fig. 4.9(c), is when the effective trailing edge of the vortex just reaches the back edge of the slit. At this moment in time the distribution of pressure at the end of the slit closely matches that observed in Fig. 4.9(b) but with opposite sign since the velocity is now in the opposite direction.

Before investigating the relationship between the surface pressure fluctuations plotted in Fig. 4.9 and its far field radiation, the physical mechanisms responsible for these surface pressure distributions are studied.

4.2.2 Source strength decay at the leading-edge

The source strength decay of a baseline aerofoil in the streamwise direction is represented on Fig. 4.10 and is found to decay following a trend in $1/\sqrt{x_1}$.

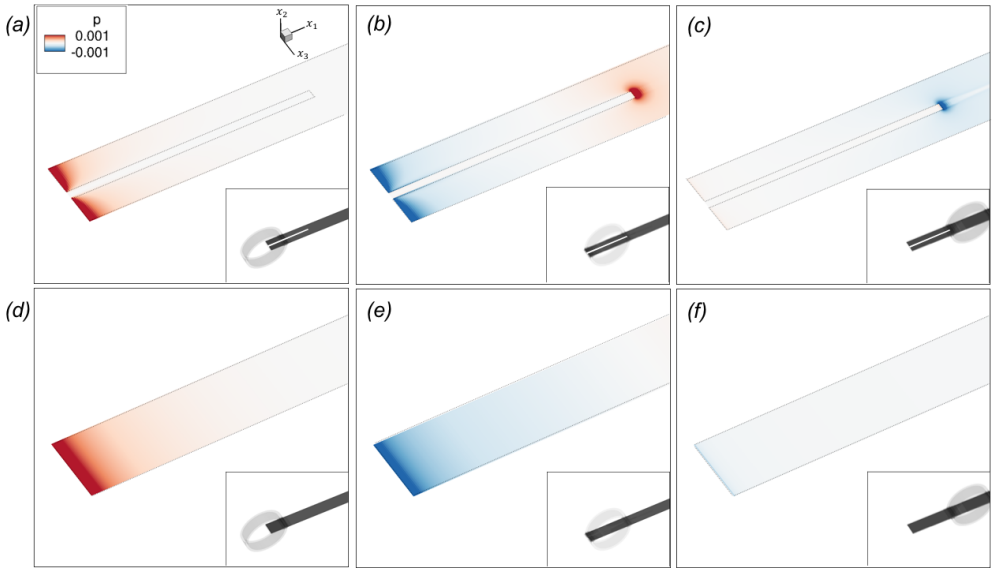

FIGURE 4.9: Contour plots of the generated acoustic pressure (p) on the aerofoil surface in temporal order: comparison slitted aerofoil ((a), (b), (c)) and baseline SLE ((d), (e), (f)). The iso-surfaces of the spanwise vorticity are represented with an additional scale on the right hand side corner to visualise the position of the main vortex

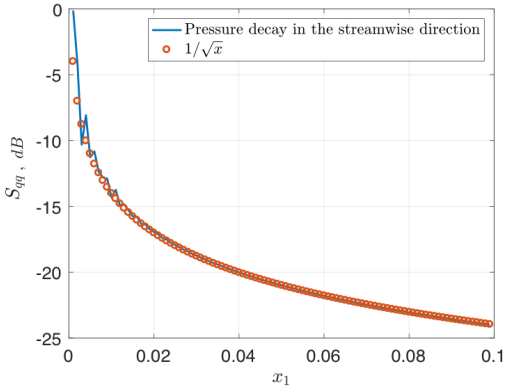

FIGURE 4.10: Source strength decay in the streamwise direction of a baseline aerofoil at $fh/U = 1.5$

For a slitted flat-plate, the pressure is found to decay at a different rate in the streamwise direction, depending on the spanwise location. Figure 4.11 represents the contour plots of the source strength at the front-edge of the slitted flat-plate for different frequencies. The pressure decay in the streamwise direction is also plotted for two spanwise locations. It is observed that, close to the spanwise boundaries, the pressure decays at the same rate as for a baseline aerofoil ($1/\sqrt{x_1}$). By contrast, closer to the slit edge, the pressure is found to decay at a faster rate of ($1/x_1$). The slit feature seems to impose a rate of decay in $1/x_1^n$, with n varying from $n = 1/2$ close to the slit edge, to $n = 1$ away from the slit.

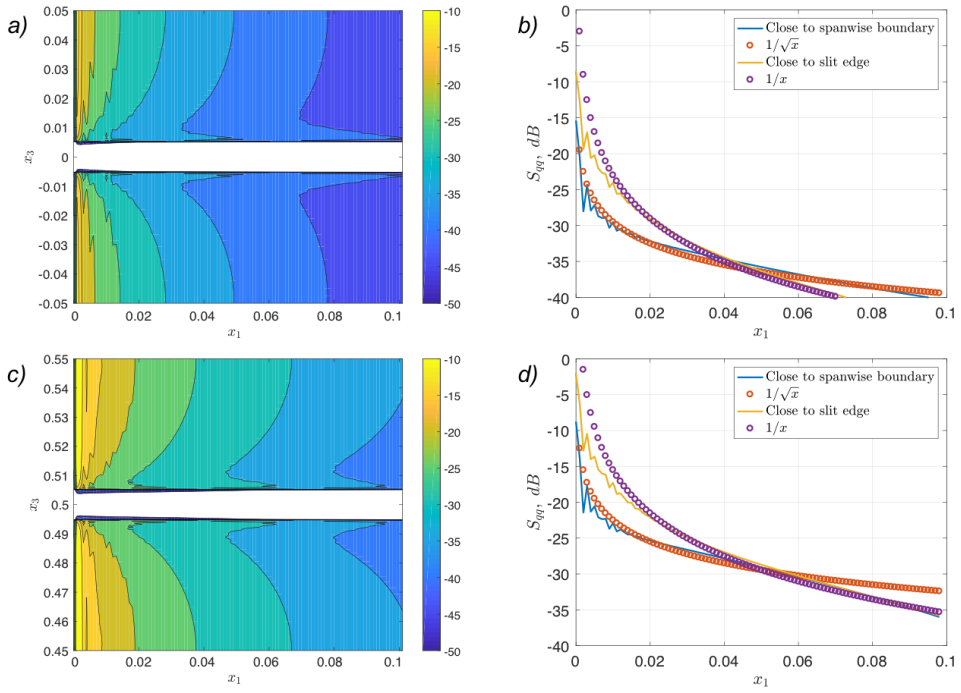

FIGURE 4.11: a), c) Contour-plots of the source strength at the leading-edge of a slitted aerofoil at different frequencies (a): $fh/U = 0.5$, c): $fh/U = 1.5$) - b), d) Source strength decay in the streamwise direction (b): $fh/U = 0.5$, d): $fh/U = 1.5$)

4.3 Secondary vortices: induced spanwise and streamwise vortices

As explained above, the generation of the two sources at the front and back-edge of the slit is due to the impingement of the main prescribed vortex on the plate. However, the respective level and shape of these acoustic regions can be linked to the influence of secondary vortices generated during the impingement of the main prescribed vortex onto the flat plate. Figures 4.12(a, b, c) show iso-surfaces of the induced spanwise and streamwise vortices created at the same three instants in time as Fig. 3.3. The no-slip boundary condition applied to the flat-plate leads to large velocity gradients in the vicinity of the slit. Strong secondary spanwise vorticity at the front and back edges can be observed, driven by the velocity gradient ($\partial v/\partial x_1 > 0$). Also present is strong secondary streamwise vorticity along the edges of the slit driven by the velocity gradient ($\partial v/\partial x_3 > 0$).

The generation of secondary vorticity was previously identified on wavy leading-edges by Turner [88] who attributed an increase in pressure at the root and a reduction in pressure at the peak to an additional downwash and counter-acting upwash respectively created by secondary vorticity. As previously demonstrated by [88], the secondary spanwise vorticity on a serrated flat plate creates an additional downwash, contributing to higher pressure fluctuations, as it is also the case for a straight leading-edge aerofoil. An identical mechanism is encountered on slitted flat-plates, at both the front and the back-edge of the slit. It can be noted that on Fig. 4.12 b) that the spanwise vorticity between the front edge and the back edge is of opposite sign, despite originating from the same single spanwise roller. The reason for these opposite values is that

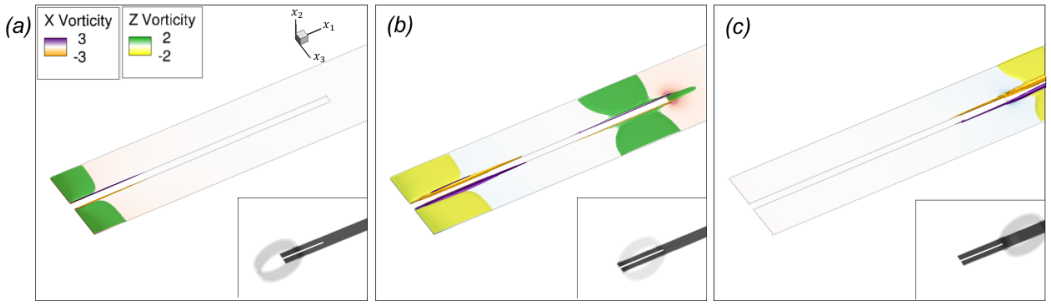

FIGURE 4.12: Contour plots for generated acoustic pressure (p) and iso-surfaces of induced vorticity generated along the leading-edge profile during the interaction, in temporal order. The iso-surfaces of the spanwise vorticity are represented with an additional scale on the right hand side corner to visualise the position of the main vortex

the secondary vorticity is responding to the sign of the velocity of the main vortex. Fig. 4.12 b) corresponds to the instance in time when the front-edge is impacted by the upwash of the main vortex and the back-edge by the downwash of the main vortex, which explains the spanwise vorticity of opposite sign.

4.3.1 Influence of secondary streamwise vortices on the slit front-edge

For slitted aerofoils, in addition to the induced spanwise vortices, a streamwise vortex system can also be seen that originates at the slit corners and arises from the streamwise velocity discontinuity in the spanwise direction x_3 ($\partial v/\partial x_3 > 0$) across the longitudinal slit edge. Figures 4.12 (a, b) show the iso-surfaces of secondary streamwise vortices generated at the front and back edge of the slit when the main vortex impinges on the front and back edge respectively. A counter-rotating pair of streamwise vortices can be observed along the longitudinal edges of the slit which grows as the vortex is convected along the plate.

Figure 4.13(c) represents an illustration of the streamwise vortex system over a $x_2 - x_3$ plane at a specific streamwise location and shows their rotation direction. It indicates the generation of an upwash velocity that counteracts the downwash of the main vortex. As a result the pressure jump along the front-edge decreases as the slit corner is approached as indicated on Fig. 4.13(a). This is consistent with the spanwise decay of the pressure observed on Fig. 4.9 b).

4.3.2 Influence of secondary streamwise vortices on the slit back-edge

The detailed variation in secondary vortex strength along the front and back edges is now considered. Fig. 4.14(a) shows the variation of spanwise and streamwise vorticity amplitudes along the span at the front-edge of the slit, as the location of maximum downwash (point A in Fig. 3.3(a)) just reaches the front edge. Similarly, Fig. 4.14(b) shows the variation in vorticity amplitudes along the back-edge of the slit as point A reaches the back edge. The comparison between Fig. 4.14(a) and Fig. 4.14(b) shows that both vorticity components are significantly larger at the back-edge than at the front for most of the span, except close to the front corner where the streamwise vorticity is generated and therefore reaches comparable levels to the levels at the back. Additionally, as indicated by Fig. 4.13(d), the downwash produced as the main

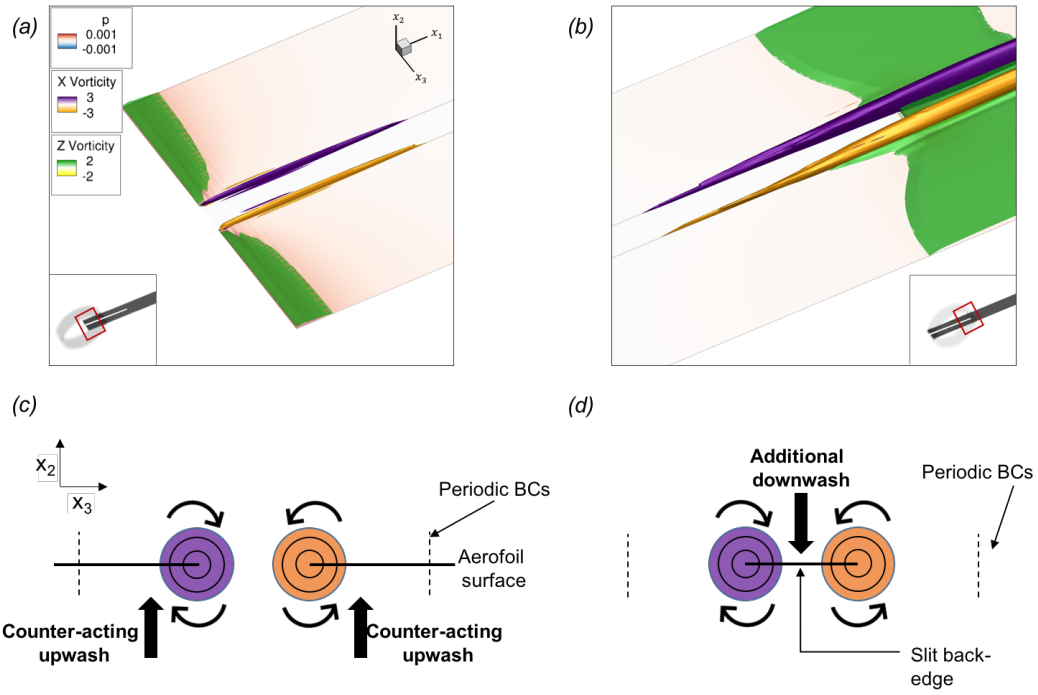

FIGURE 4.13: Influence of the counter-rotating pair of secondary streamwise vortices generated during the downwash of the main vortex: (a) zoom on the leading-edge as the main vortex impinges on the front-edge - (b) zoom on the back-edge as the main vortex impinges on the back-edge - (c) illustration of the streamwise vortices rotation at the front-edge - (d) illustration of the streamwise vortices rotation at the back-edge

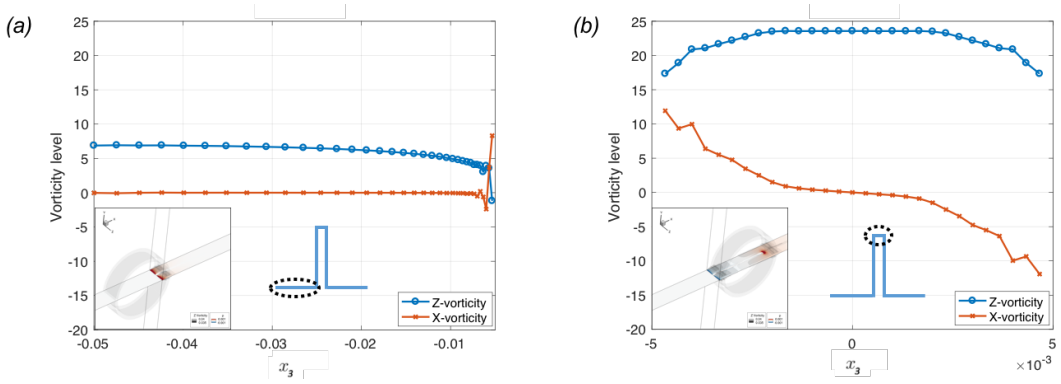

FIGURE 4.14: Spanwise and streamwise vorticity levels as the maximum downwash velocity (point A on Fig. 3.3 (a)) reaches the slit front edge (a) and the slit back-edge (b)

vortex impinges on the back-edge of the slit is enhanced by the additional downwash created by the secondary streamwise vortices. This combined effect is responsible for the significantly higher pressure fluctuations observed at the back-edge of the slit.

The evolution of the streamwise vortices created at the front-edge region as they are convected along the streamwise edge of the slit is studied by measuring the vorticity at a fixed point in the main vortex reference frame. The chosen locations correspond to the points of highest downwash amplitude (point A). The X-vorticity levels at point A is represented in temporal order in Fig. 4.15, which shows that the velocity discontinuity along the slit keeps feeding the streamwise

vortices. As a result, a growth of the vortices in size is observed as they are convected. A second pair of streamwise vortices is generated as the vortex reaching the back-edge region. Additionally, the vortices seem to be convected away from the plate, shifting below the lower surface during the downwash (and above the upper surface during the upwash, not shown here).To illustrate the behaviour of the streamwise vortex system more clearly, vorticity streamlines are plotted in Fig. 4.16. As observed in Fig. 4.15, the vortex is driven beneath the plate during the downwash phase of the main vortex (and above the plate during the upwash phase, not shown here). Due to their opposing sense of rotation the two vortices will drive each other further away from the plate as they convect with the mean flow.

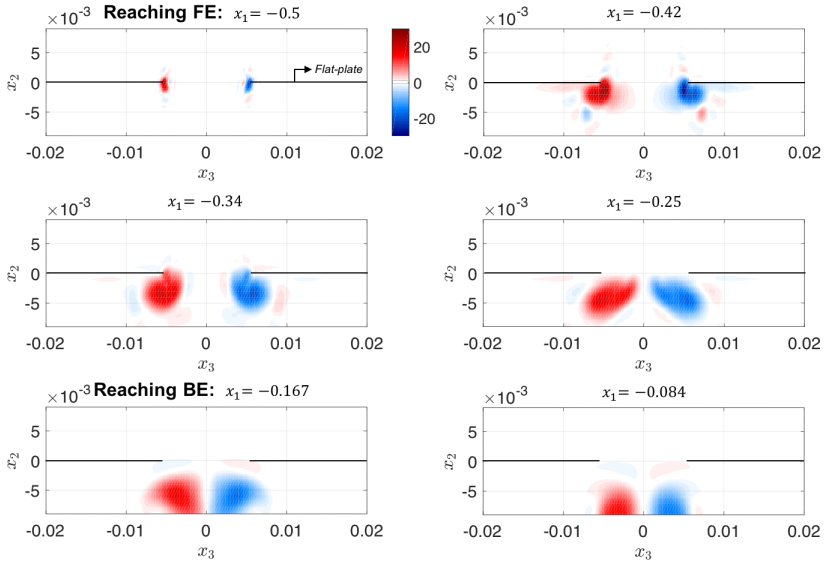

FIGURE 4.15: Contour-plots of the streamwise vorticity in the x_2/x_3 plane as the point A of maximum downwash in the vortex travels along the slit longitudinal edge from the front-edge of the slit to the back-edge

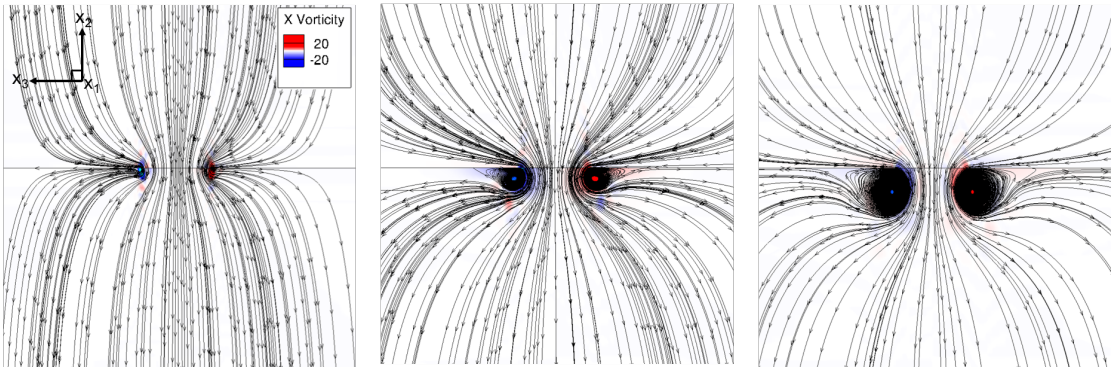

FIGURE 4.16: Streamlines in the x_2/x_3 plane as the point A of maximum downwash in the vortex travels along the slit longitudinal edge from the front-edge of the slit (a) to the back-edge (c)

It can be noted that the pressure fluctuations at the back-edge of the slit are likely to vary with the slit length, depending on the level of the streamwise vorticity reaching the back-edge. The source level at the back-edge will therefore vary with slit length, but the generation mechanism

remains the same.

The spanwise vortex model investigated in this chapter can be assumed to be a simple representation of a coherent structure within a turbulent flow. In practice, turbulence comprises a range of vortex scales with random orientation. However, it can be assumed that the same basic noise reduction mechanisms applies: it will be shown in Chapter 7 that there is qualitative agreement between predictions and experiments, which seems to indicate that the same mechanism applies although further work is needed to confirm this.

Chapter 5

Physical mechanisms of slitted leading-edge profiles: far-field radiation

Chaitanya et al [4] has proposed two noise reduction mechanisms to explain the enhanced noise reductions due to slitted aerofoils. One is related to a reduction in overall source strength, the other is related to interference between two highly coherent sources at either ends of the slit of roughly the same strength. Section 4.2 has confirmed the presence of two regions of very localised pressures at either ends of the slit.

Based on the hypothesis of two compact coherent sources Chaitanya et al has proposed a model for predicting sound power reductions at any arbitrary frequency. The model was aimed at explaining his experimental observations which showed that maximum sound power reductions were obtained at frequencies f_n for which $f_n h/U = (2n+1)/2$, where n is any integer $n = 0, 1, 2...$, as shown in Fig. 1.7. This observation provided evidence of strong interference between two compact source regions at either ends of the slit, which was used as the basis of the model. However, the model provides no insight into the effect of the slits on the detailed far field pressure directivity. Furthermore, in this frequency domain model, it was not possible to predict the condition for maximum overall noise reductions when integrated over all frequencies.

In this section the simple two-source model is further developed for predicting the noise reductions and also to assist in the understanding of the detailed noise reduction mechanism. The model captures all of the features observed in the numerical predictions and experiments, including both constructive and destructive interference as observed in Chaitanya [4].

5.1 Derivation of the two-source analytic model

The surface pressure distribution shown in Fig. 4.9 reveals the presence of two distinct source regions; one at the leading edge and another localised around the serration root. The integration of the surface pressures required to compute the far field radiation in Eq. (4.3) is therefore the

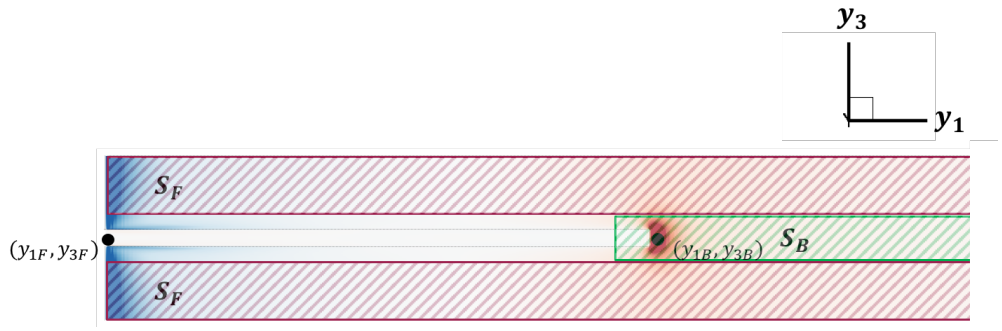

FIGURE 5.1: Illustration of front and back-edge areas. The two circles indicate the respective acoustic centres in each source region.

sum of the surface integrations taken over their respective source areas S_F and S_B as illustrated in Fig. 5.1,

$$p(\mathbf{x},t) = -\frac{x_2}{4\pi c\sigma^2}\left[\iint_{S_\mathrm{F}} \frac{\partial \Delta p(\mathbf{y},\tau)}{\partial \tau}\mathrm{d}S(\mathbf{y}) + \iint_{S_\mathrm{B}} \frac{\partial \Delta p(\mathbf{y},\tau)}{\partial \tau}\mathrm{d}S(\mathbf{y})\right]_{\tau=t-\tau^*} \tag{5.1}$$

Based on the observation in Fig. 4.9 that these two source regions are highly localised at either ends of the slit, the source distribution resulting from the surface pressure integrations is now approximated by two compact sources with appropriate time delays τ^*_F and τ^*_B,

$$\left[\iint_{S_\mathrm{F,B}} \frac{\partial \Delta p(\mathbf{y},\tau)}{\partial \tau}\mathrm{d}S(\mathbf{y})\right]_{\tau=t-\tau^*} \approx \left[\dot{F}_\mathrm{F,B}(\tau)\right]_{\tau=t-\tau^*_\mathrm{F,B}} \tag{5.2}$$

where $[\dot{}]$ is used to denote differentiation with respect to time and where the acoustic source strengths F_F and F_B are identified as the surface integrals of the surface pressures taken over the respective acoustic regions,

$$F_\mathrm{F}(t) = \iint_{S_\mathrm{F}} \Delta p(\mathbf{y},t)\mathrm{d}S_\mathrm{F}(\mathbf{y}), \qquad F_\mathrm{B}(t) = \iint_{S_\mathrm{B}} \Delta p(\mathbf{y},t)\mathrm{d}S_\mathrm{B}(\mathbf{y}) \tag{5.3}$$

The time delays between the effective centres of the sources, $(y_{1\mathrm{F}}, y_{3\mathrm{F}})$ and $(y_{1\mathrm{B}}, y_{3\mathrm{B}})$ at the front and back of the slit respectively, τ^*_F and τ^*_B can be calculated from the expression for τ in Eq. (4.2). In this analysis it is assumed that the observer is located in the $x_1 - x_2$ plane at $x_3 = 0$ corresponding to the middle of the slit. For this situation, the time delays are given by,

$$\left.\begin{aligned} \tau^*_\mathrm{F} &= \frac{r_{\beta\mathrm{F}} - Mr_{1\mathrm{F}}}{c\beta^2} \\ \tau^*_\mathrm{B} &= \frac{r_{\beta\mathrm{B}} - Mr_{1\mathrm{B}}}{c\beta^2} \end{aligned}\right\} \tag{5.4}$$

where $r_1 = (x_1 - y_1)$ and $r_\beta \approx \sigma - \frac{x_1 y_1 + \beta^2 x_3 y_3}{\sigma}$, in which $y_{1\mathrm{B}} = y_{1\mathrm{F}} + h$, $y_{2\mathrm{F}} = y_{2\mathrm{B}} = 0$ and $y_{3\mathrm{F}} = y_{3\mathrm{B}} = 0$.

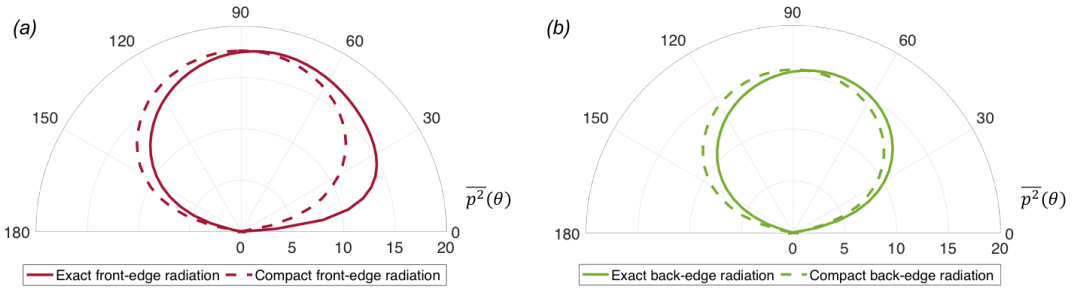

FIGURE 5.2: Comparison of the mean square pressure directivity obtained using the two-point source analytic model and the exact numerical predictions: (a) front-edge radiation - (b) back-edge radiation

In order to validate this compact source assumption the mean square pressure directivity obtained from the exact surface pressure integration of Eq. (5.1) is compared in figures 5.2(a, b) to that obtained using the compact assumption of Eq. (5.2) for both the front and root source regions respectively.

Figure 5.2 shows those mean square pressure directivities in dB in the $x_3 = 0$ plane. Figure 5.2(b) confirms the compact source hypothesis for the root region where very close agreement is observed between the exact and approximate directivity predictions. Similarly good agreement can also be observed for the front edge region in Fig. 5.2(a), except for a small range of downstream angles where significant deviations of up to 4dB between the two predictions can be observed. This front-edge source directivity is characteristic of leading edge radiation in the high frequency limit. Nevertheless, the compact source assumption appears to provide a reasonable approximation to the exact directivity over most observer angles.

Both the far field mean square pressure and its Power Spectral Density can be obtained from the auto-correlation of the far-field radiated pressure defined by Eq. (5.1).

$$R_{\mathrm{pp}}(\tau) = E\left[p(\mathrm{t})p(\mathrm{t}\text{-}\tau)\right] \tag{5.5}$$

where $E[.]$ denotes Expectation, which for turbulent flows is essentially the average taken over a sufficiently long time duration. However, since the study only considers a single vortex only one realisation is possible and the Expectation is therefore redundant. Replacing the far-field radiated pressure by the expression obtained in Eq. (5.1), the auto-correlation of the acoustic pressure can be written in terms of the temporal derivatives of the acoustic source strengths F_{F} and F_{B},

$$R_{\mathrm{pp}}(\tau) = \left(\frac{x_2}{4\pi c\sigma^2}\right)^2 \left(E\left[\left(\dot{F}_{\mathrm{F}}(t) + \dot{F}_{\mathrm{B}}(t-\tau_{\mathrm{A}})\right)\left(\dot{F}_{\mathrm{F}}(t-\tau) + \dot{F}_{\mathrm{B}}(t-\tau-\tau_{\mathrm{A}})\right)\right]\right) \tag{5.6}$$

where

$$\tau_{\mathrm{A}} = \tau^*_{\mathrm{B}} - \tau^*_{\mathrm{F}} = \frac{h}{c\beta^2}(M - \frac{x_1}{\sigma}), \tag{5.7}$$

which represents the difference in travel times between the front and back edge sources to the observer.

Expanding Eq. (5.6), $R_{\mathrm{pp}}(\tau)$ can be re-written in terms of the sum of the auto-correlations of the front and back-edge sources $R_{\dot{\mathrm{F}}\dot{\mathrm{F}}}(\tau) + R_{\dot{\mathrm{B}}\dot{\mathrm{B}}}(\tau)$ plus the cross-correlation between them $R_{\dot{\mathrm{F}},\dot{\mathrm{B}}}(\tau)$, as indicated by Eq. (5.8).

$$R_{\mathrm{pp}}(\tau) = \left(\frac{x_2}{4\pi c\sigma^2}\right)^2 \left(R_{\dot{\mathrm{F}}\dot{\mathrm{F}}}(\tau) + R_{\dot{\mathrm{B}}\dot{\mathrm{B}}}(\tau) + R_{\dot{\mathrm{B}},\dot{\mathrm{F}}}(\tau - \tau_{\mathrm{A}}) + R_{\dot{\mathrm{F}},\dot{\mathrm{B}}}(\tau + \tau_{\mathrm{A}})\right) \tag{5.8}$$

Note also that for computational reasons it may be useful to use the identity $R_{\dot{\mathrm{x}},\dot{\mathrm{x}}}(\tau) = -\frac{\partial^2}{\partial\tau^2} R_{\mathrm{x,x}}(\tau)$.

5.2 Mean square pressure directivity

The mean square pressure at any point in the sound field can be calculated from Eq. (5.8) by setting $\tau = 0$:

$$\overline{p^2}(x_1, x_2, x_3 = 0) = R_{\mathrm{pp}}(0) = \left(\frac{x_2}{4\pi c\sigma^2}\right)^2 \left(R_{\dot{\mathrm{F}}\dot{\mathrm{F}}}(0) + R_{\dot{\mathrm{B}}\dot{\mathrm{B}}}(0) + 2R_{\dot{\mathrm{F}},\dot{\mathrm{B}}}(\tau_{\mathrm{A}})\right) \tag{5.9}$$

in which $\tau_{\mathrm{A}} = \tau_{\mathrm{A}}(\theta)$, where the following symmetry property has been used: $R_{\dot{\mathrm{B}},\dot{\mathrm{F}}}(-\tau_A) = R_{\dot{\mathrm{F}},\dot{\mathrm{B}}}(\tau_A)$.

This expression demonstrates that greatest noise reductions are obtained for the range of τ_{A} for which $R_{\dot{\mathrm{B}},\dot{\mathrm{F}}}(-\tau_{\mathrm{A}}) \leq 0$, i.e., for the range of observer angles for which the front and back-edge sources are anti-correlated. The observer angle θ can be uniquely calculated from τ_{A} by using $x_1 = r\cos\theta$, $x_2 = r\sin\theta$, $x_3 = 0$ and $\sigma = r\sqrt{\cos^2\theta + \beta^2\sin^2\theta}$ in Eq. (5.4), giving:

$$\tau_{\mathrm{A}}(\theta) = \frac{h}{c\beta^2}\left(M - \frac{\cos\theta}{\sqrt{\cos^2\theta + \beta^2\sin^2\theta}}\right) \tag{5.10}$$

The range of possible values of τ_{A} encompassing the range of observer angles between $\theta = 0°$ (downstream) and $\theta = 180°$ (upstream) may be obtained by substituting these angle limits into Eq. (5.10) to give,

$$\frac{-h}{c(1+M)} \leq \tau_{\mathrm{A}} \leq \frac{h}{c(1-M)} \tag{5.11}$$

Eq. (5.10) may be inverted to give the observer angle θ for any difference in arrival time τ_{A} in the range of τ_{A} specified above,

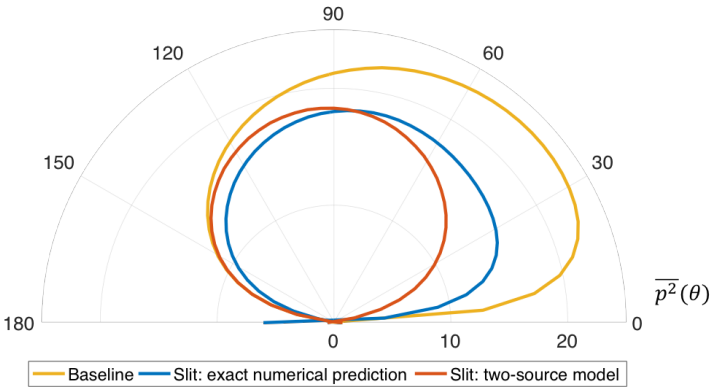

FIGURE 5.3: Directivity of the mean square pressure for both baseline and slitted aerofoil: comparison between the two-point source analytic model and the exact numerical predictions

$$\theta = \arctan\left[\frac{1}{\beta}\sqrt{\frac{1}{(M-\frac{\beta^2}{M}\frac{\tau_{\mathrm{A}}}{\tau_{\mathrm{H}}})^2}-1}\right] \tag{5.12}$$

where $\beta^2 = 1 - M^2$ and τ_{H} is the time taken for the vortex to convect along the slit length h,

$$\tau_{\mathrm{H}} = h/U \tag{5.13}$$

Figure 5.3 shows the mean square pressure directivity in dB in the plane $x_3 = 0$ for the baseline case and for the slitted aerofoil obtained using the complete surface pressure integration of Eq. (4.3) and also using the two-source model of Eq. (5.1). The directivity obtained using the model can be observed to provide reasonably good agreement with the exact calculation with the greatest discrepancy of about 5dB occurring downstream of the aerofoil, consistent with the deviation observed in Fig. 5.2 between the exact and approximate front edge directivity functions.

Greatest noise reductions of about 8dB can be observed in the downstream direction calculated from the exact model. However, negligible noise reductions are predicted using both models in the upstream direction. This behaviour can be explained from the characteristics of the cross correlation function $R_{\dot{\mathrm{B}},\dot{\mathrm{F}}}(\tau)$ which control the directivity in Eq. (5.9).

Figure 5.4 shows the cross-correlation $R_{\dot{\mathrm{F}},\dot{\mathrm{B}}}(\tau)$ in normalised form (between -1 and 1) as the coefficient $R_{\dot{\mathrm{F}},\dot{\mathrm{B}}}(\tau)/\sqrt{(R_{\dot{\mathrm{B}},\dot{\mathrm{B}}}(0)R_{\dot{\mathrm{F}},\dot{\mathrm{F}}}(0))}$ plotted against the ratio τ/τ_H. Also shown in this figure is the range of possible τ_A values given by Eq. (5.11) ($-0.23 \leq \tau_A/\tau_H \leq 0.43$). The correlation function can be observed to peak at about 0.8 at $\tau/\tau_{\mathrm{H}} = 1.1$. Despite the presence of secondary vorticity at the back edge of the slit, the pressure fluctuations between front and back therefore remain highly correlated, which is essential for effective interference between the two source regions. Note also that the time of peak correlation, $\tau/\tau_{\mathrm{H}} = 1.1$, indicates that the effective centres of the two source regions are about 10% further apart than the physical slit height h. This may be related to the size of the vortex being 10% greater than the length of the slit h in this particular example. But more work is needed to confirm this.

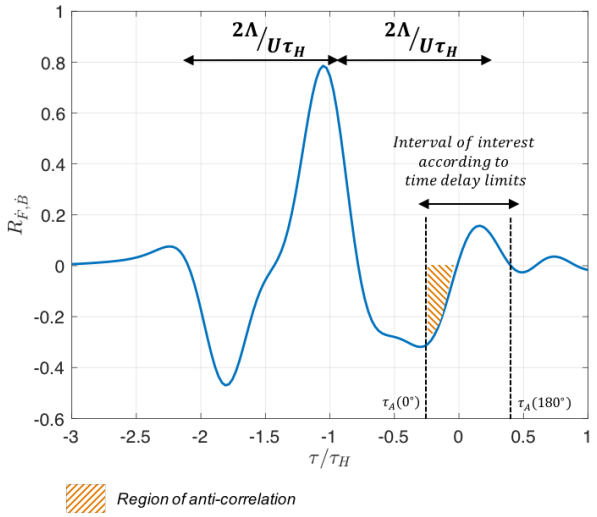

FIGURE 5.4: Cross-correlation coefficient between the front and back-edge acoustic sources

The correlation function within the permissible range of τ_A values given by Eq. (5.8) can be observed to be anti-correlated (as indicated by the hatched region) for $-0.23 < \tau_A/\tau_H < 0$ corresponding to the range of upstream angles between 0° and 73°. Greatest noise reductions in Fig. 5.3 are therefore obtained for this range of angles. By contrast, positive correlation is observed for $0 < \tau_A/\tau_H < 0.43$ corresponding to the range of predominantly downstream observer angles of 73° to 180°.

Figure 5.4 makes explicit that good levels of noise reduction are obtained when the range of permissible τ_A values are situated in the anti-correlation region of the correlation function, which is mostly controlled by the vortex size Λ. To understand this behaviour more clearly the time taken for the vortex to pass over the front or back edge, $2\Lambda/U$, is indicated in Fig. 5.4 by horizontal arrows and can be seen to roughly match the time duration between the main peak at $\tau/\tau_H = 1.1$ and the second largest peak at $\tau/\tau_H = -0.2$. Noise control performance is therefore determined by the combination of the slit length and vortex size. A complete parameter study is therefore required to determine the optimum slit length for a particular vortex size corresponding to an integral length-scale for incoming turbulence.

5.3 Frequency dependence of noise reduction

The previous section has analysed the mechanism of noise reduction by a narrow leading edge slit on a flat plate interacting with a single spanwise vortex. The conditions for overall noise reduction, i.e., integrated over all frequencies, were discussed. However, this analysis provides no insight into the performance of slits across the frequency range. The two-source model developed in Section **??** is now re-formulated in the frequency domain where the Power Spectral Density (PSD) of the far field pressure is derived and related to the mean square pressure by,

$$\overline{p^2} = R_{pp}(0) = \int_{-\infty}^{\infty} S_{pp}(\omega)\,\mathrm{d}\omega, \tag{5.14}$$

The far-field pressure PSD is related to the Fourier Transform of the autocorrelation function,

$$S_{\mathrm{pp}}(\omega) = \int_{-\infty}^{\infty} R_{\mathrm{pp}}(\tau) e^{\mathrm{i}\omega\tau}\,\mathrm{d}\tau \tag{5.15}$$

Substituting Eq. (5.8),

$$S_{\mathrm{pp}}(\omega) = \left(\frac{x_2}{4\pi c\sigma^2}\right)^2 \int_{-\infty}^{\infty} \left[R_{\dot{\mathrm{F}}\dot{\mathrm{F}}}(\tau) + R_{\dot{\mathrm{B}}\dot{\mathrm{B}}}(\tau) + R_{\dot{\mathrm{B}},\dot{\mathrm{F}}}(\tau - \tau_A) + R_{\dot{\mathrm{F}},\dot{\mathrm{B}}}(\tau + \tau_{\mathrm{A}})\right] e^{\mathrm{i}\omega\tau}\mathrm{d}\tau \tag{5.16}$$

Using the Fourier Transform identity $\int_{-\infty}^{\infty} R_{\mathrm{pp}}(\tau-\tau_0)e^{\mathrm{i}\omega\tau}\,\mathrm{d}\tau = S_{\mathrm{pp}}(\omega)e^{\mathrm{i}\omega\tau_0}$, Eq. (5.16) becomes,

$$S_{\mathrm{pp}}(\omega) = \left(\frac{x_2}{4\pi c\sigma^2}\right)^2 \left(S_{\dot{\mathrm{F}}\dot{\mathrm{F}}}(\omega) + S_{\dot{\mathrm{B}}\dot{\mathrm{B}}}(\omega) + S_{\dot{\mathrm{B}}\dot{\mathrm{F}}}(\omega)e^{\mathrm{i}\omega\tau_{\mathrm{A}}} + S_{\dot{\mathrm{F}}\dot{\mathrm{B}}}(\omega)e^{-\mathrm{i}\omega\tau_{\mathrm{A}}}\right) \tag{5.17}$$

Noting that the cross correlation coefficient $R_{\dot{\mathrm{B}},\dot{\mathrm{F}}}$ plotted in Fig. 5.4 has peak value of 0.8 shifted in time by a delay very close to τ_{H} suggests that its corresponding cross spectra $S_{\dot{\mathrm{B}},\dot{\mathrm{F}}}$ and $S_{\dot{\mathrm{F}},\dot{\mathrm{B}}}$, may be expressed in the form $S_{\dot{\mathrm{B}}\dot{\mathrm{F}}}(\omega) = |S_{\dot{\mathrm{B}}\dot{\mathrm{F}}}(\omega)|e^{\mathrm{i}\omega\tau_{\mathrm{H}}}$ and $S_{\dot{\mathrm{F}}\dot{\mathrm{B}}}(\omega) = |S_{\dot{\mathrm{F}}\dot{\mathrm{B}}}(\omega)|e^{-\mathrm{i}\omega\tau_{\mathrm{H}}}$. The phase of the cross spectrum, $\omega\tau_{\mathrm{H}}$ therefore arises entirely from the time taken for the vortex to convect along the slit.

Lastly, the approximation $|S_{\dot{\mathrm{B}},\dot{\mathrm{F}}}(\omega)| = \sqrt{S_{\dot{\mathrm{F}}\dot{\mathrm{F}}}(\omega)S_{\dot{\mathrm{B}}\dot{\mathrm{B}}}(\omega)}$ is made, owing to the high maximum correlation coefficient (≈ 0.8), the final expression for the far-field pressure PSD is given by,

$$S_{\mathrm{pp}}(\omega) = \left(\frac{x_2}{4\pi c\sigma^2}\right)^2 \left(S_{\dot{\mathrm{F}}\dot{\mathrm{F}}}(\omega) + S_{\dot{\mathrm{B}}\dot{\mathrm{B}}}(\omega) + 2\sqrt{S_{\dot{\mathrm{F}}\dot{\mathrm{F}}}(\omega)S_{\dot{\mathrm{B}}\dot{\mathrm{B}}}(\omega)}\cos(\omega(\tau_{\mathrm{A}} + \tau_{\mathrm{H}}))\right) \tag{5.18}$$

with $S_{\dot{\mathrm{F}}\dot{\mathrm{F}}}(\omega)$ and $S_{\dot{\mathrm{B}}\dot{\mathrm{B}}}(\omega)$ are the source strength PSD of the front and back edge respectively, calculated by taking the PSD of Eq. (5.3). The ratio of these frequency-dependent source strengths will be examined later in subsection 5.6. Note that for computational purposes it may be useful to note the identity $S_{\dot{\mathrm{x}}\dot{\mathrm{y}}}(\omega) = \omega^2 S_{\mathrm{xy}}(\omega)$.

The form of Eq. (5.18) for the far field pressure PSD provides a clear interpretation of the noise reduction mechanism. It demonstrates that, at any single frequency ω and observer angle θ, the front and back edge of the slit arrive with a phase difference of $\omega(\tau_{\mathrm{H}} + \tau_{\mathrm{A}})$. The sum of time delays $\tau_{\mathrm{H}} + \tau_{\mathrm{A}}$ corresponds to the time taken τ_{H} for the vortex to convect from one end of the slit to the other, plus the difference in times τ_{A} taken for sound to propagate from the front and back edges to the far field observer, as sketched in Fig. 5.5.

5.4 Frequency-dependent directivity

In this section the detailed behaviour of the far field directivity as specified by Eq. (5.18) is investigated as a function of frequency, where τ_{A} is computed from θ using Eq. (5.12). Figure 5.6 shows the directivity function based on the two-source model prediction of Eq. (5.18) at four

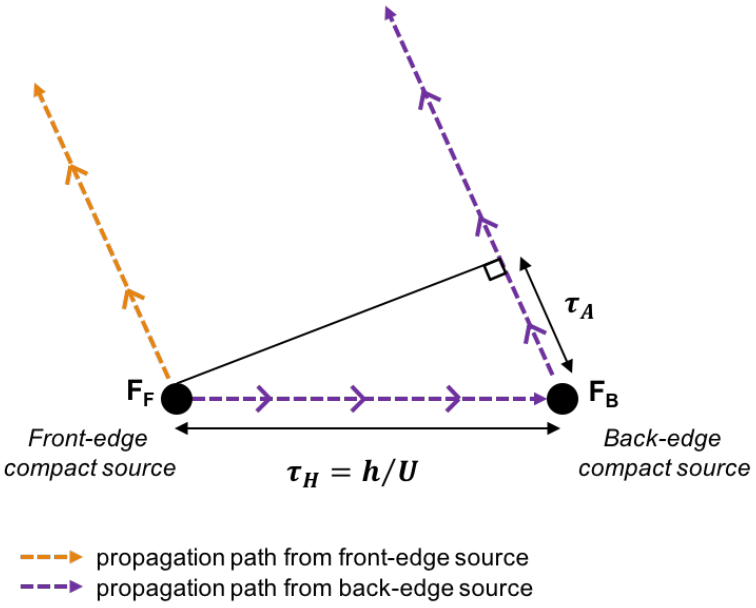

FIGURE 5.5: Illustration for the hydrodynamic and acoustic delays between the propagation from the front and back-edge sources

non-dimensional frequencies. Also shown is the directivity prediction for the slitted and baseline profiles obtained by taking the PSD of the exact calculation of $p(t)$ from Eq. (4.3).

Overall agreement between the exact and approximate far field directivity predictions can be observed to be better than 3dB over most angles, with the greatest discrepancy occurring at small downstream angles less than 20°, where differences of up to 10dB can be observed. This deviation is due to the errors in the compact approximation shown explicitly in Fig. 5.2(a).

The directivity functions plotted in Fig. 5.6, in dB in the plane $x_3 = 0$, can be observed to be highly frequency dependent. As for the mean square pressure plotted in Fig. 5.3, greatest noise reductions occur downstream with negligible reduction upstream at observer angles greater than about 90°. The reason for the differing upstream and downstream behaviour is because the directivity function due to the slitted flat plate is more omni-directional than for baseline directivity whose radiation pattern extends further downstream as the leading-edge source distribution becomes less compact as shown in Fig. 4.9. Unlike for the mean square pressure, however, the directivity pattern at a single frequency for the slitted case can be observed to display a number of sidelobes whose number increases with increasing frequency. Clearly, therefore, in a narrow frequency band, interference between the front and back edge is important in controlling the directivity. This is in contrast with the mean square pressure directivity which is only controlled by the correlation between back and front sources.

5.5 Optimum observer position

One of the most significant features of these directivity plots is the existence of particular optimum observer angles for which the noise reductions are especially high. No such angle can

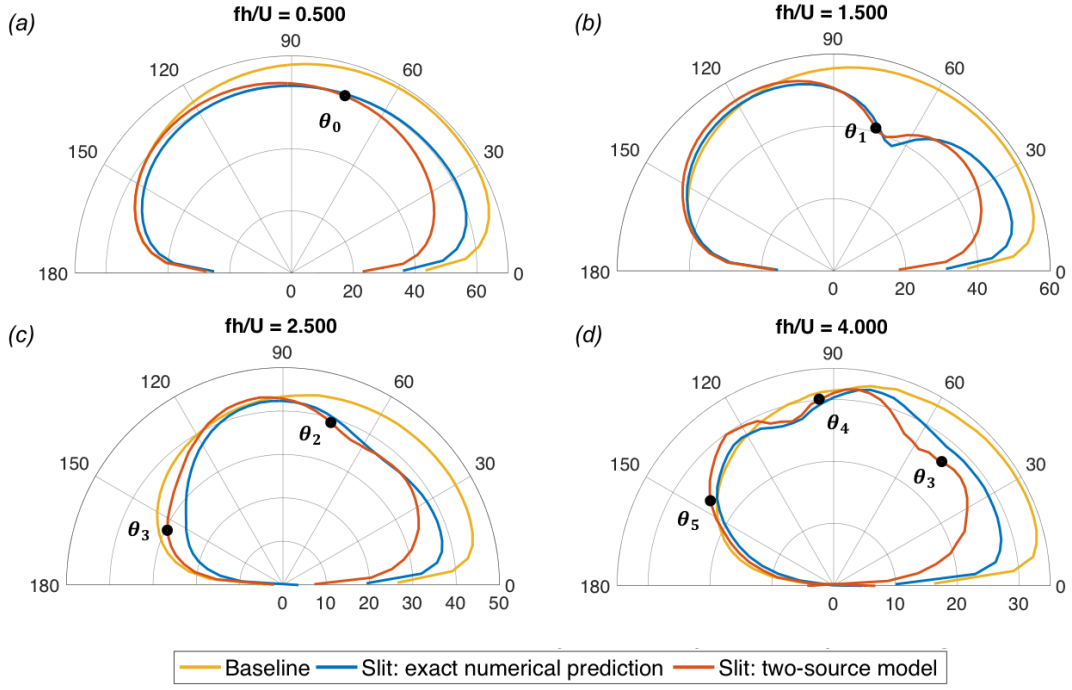

FIGURE 5.6: Far-field directivities at different non-dimensional frequencies: comparison between two-source analytic model and exact numerical predictions

be observed at the lowest frequency of $fh/U = 0.5$ plotted in Fig. 5.6(a). However, a single optimum angle in the directivity can be observed in Fig. 5.6(b) at the higher frequency of $fh/U = 1.5$, and two optimum at $fh/U = 2.5$ and $fh/U = 3.5$ in figures 5.6(c, d).

The presence of these optimum angles of large noise reduction corresponds to the angles θ_n for which the front and back edge radiate with a phase difference equal to odd multiples of 180°. The condition for these observer angles, neglecting the θ-dependence of the factor $\frac{x_2}{4\pi c\sigma^2}$, is therefore given by,

$$\omega\left(\tau_\mathrm{H} + \tau_\mathrm{A}(\theta_\mathrm{n})\right) = (2n+1)\pi \tag{5.19}$$

Substituting the expressions for $\tau_\mathrm{H} = h/U$ and τ_A from Eq. (5.10), the solution for θ_n can be expressed in terms of non-dimensional $f^* = fh/U$ as,

$$\theta_\mathrm{n} = \arctan\left[\frac{1}{\beta}\sqrt{\frac{1}{\left[M+\beta^2\left(\frac{1}{M}-\frac{(2n+1)}{2f^*M}\right)\right]^2}-1}\right] \tag{5.20}$$

The number of distinct solutions θ_n to Eq. (5.20) can be determined from the number of n values for which the expression under the square root is positive. This condition may be shown to reduce to the number of n values for which the frequency f^* lies in the following range,

$$\frac{1}{2}(2n+1)(1-M) \leq f^* \leq \frac{1}{2}(2n+1)(1+M) \tag{5.21}$$

Clearly, therefore, as f^* increases there is a greater number of n values for which this condition is satisfied. There is therefore a threshold frequency $f^*_{\min}$ below which no optimum observer angle exists. This frequency, $f^*_{\min}$ is associated with the lower limit of Eq. (5.21) for $n = 0$,

$$f^*_{\min} = \frac{1}{2}(1 - M) \tag{5.22}$$

From the expression for θ of Eq. (5.20), the minimum frequency $f^*_{\min}$ can be seen to correspond to $\theta = 0°$. As the frequency is increased, Eq. (5.20) suggests that this angle of maximum noise reduction travels from 0° to 180°, corresponding to the upper limit of Eq. (5.21) of $f^* = (1 + M)/2$. As the frequency f^* is increased, there is a larger number of optimum angles that can co-exist at the same frequency. This behaviour is consistent with the directivity plots in Fig. 5.6 where the different solutions are marked as circles. Note the small shift between the predicted and the exact optimum angles, due to the omission of the factor $\frac{x_2}{4\pi c\sigma^2}$ in the estimate of $\theta_{\rm n}$ given by Eq. (5.20).

5.6 Source balance on slitted aerofoils

According to the simple two-source model of Eq. (5.18), the noise radiation from the slitted serration is determined by the two source strengths $S_{\dot{F}\dot{F}}(\omega)$ and $S_{\dot{B}\dot{B}}(\omega)$ at the front and back of the slit. Greatest noise reductions are achieved when these source strengths are equal. The balance of these source strength as a function of frequency is now examined.

Figure 5.7(a) shows the variation in the source strengths $S_{\dot{\rm F}\dot{\rm F}}(\omega)/\Phi_{\rm vv}(\omega)$ and $S_{\dot{\rm B}\dot{\rm B}}(\omega)/\Phi_{\rm vv}(\omega)$ expressed in dB, versus f^*, where $\Phi_{\rm vv}(\omega)$ is the velocity spectrum of the incoming vortex, plotted in Fig. 3.3(b). This normalisation is necessary to remove the oscillations in the noise spectrum due to those in the velocity spectrum to allow the pressure response on the surface of slitted serration to be more clearly identified. Also shown is the corresponding integrated source strength of the baseline aerofoil normalised on $\Phi_{\rm vv}(\omega)$, which may be a misleading indicator of source strength since it is no longer compact in this sharp edge case (see Fig. 4.9) but may provide a useful means with which to compare the source strengths.

The source strength spectra due to the baseline flat plate and the front edge of the slit after normalisation by the highly oscillatory velocity spectrum in Fig. 3.3(b), can be observed to vary smoothly and by less than 12dB over the frequency range. The absence of oscillations in these spectra suggests that these source strengths are closely linked to the incoming velocity spectrum. However, the pressure response due to different vortex dimensions must be calculated to establish whether there is a linear association between the pressure and velocity spectra for this complex slitted geometry. The source spectrum due to the baseline case can be observed to decay very slowly with increasing frequency, consistent with the classical frequency dependence of leading edge interaction noise. The integrated source strength at the front the slit can be seen to generally increase with increasing frequency but never exceeds the baseline source strength. However, the frequency spectrum at the back of the slit, after normalisation by the incoming velocity spectrum, can be observed to exhibit much larger variations with frequency. Sharp peaks in the spectrum can be observed, which coincide with the dips in the velocity spectrum plotted in Fig. 3.3(b). Clearly, therefore, the source spectrum at the back of the slit is not directly related

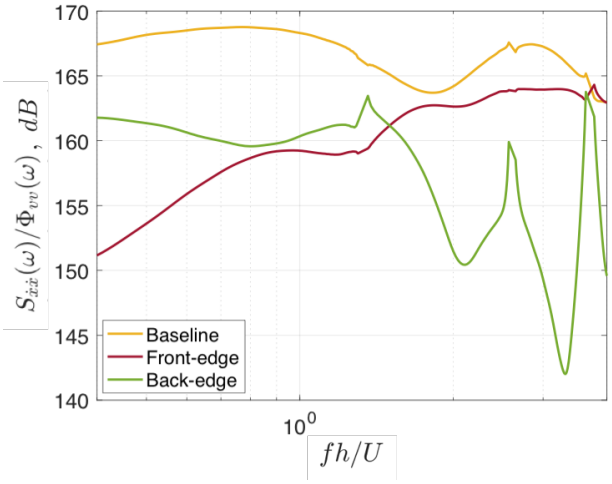

FIGURE 5.7: Source strengths on the aerofoil surface for the baseline case and for the slitted case at the front and back-edge regions

to the incoming velocity spectrum, which is consistent with the presence of strong secondary vorticity.

For this particular choice of slit dimensions (h and w) and choice of vortex size, the front and back edge source strengths can be observed to closely match at $f^* = 1.5$. Maximum levels of noise reduction are therefore predicted at this frequency, as shown in the directivity plot of Fig. 5.6(b), where sound pressure level reductions of up to 20dB are shown at the optimum angle θ_1, where the total phase delay $\omega(\tau_A + \tau_H)$ equals 3π. At the frequency of $f^* = 0.5$, however, the source strengths can be seen to differ by about 8dB, suggesting relatively weak interference effects at this frequency. This prediction is consistent with the directivity plot of Fig. 5.6(a) at $f^* = 0.5$ in which poorer levels of noise reduction of around 10dB are observed and entirely attributed to a direct reduction in source strengths on the plate compared to the baseline case.

It is clear, therefore, that achieving the desired equality between the source strengths at the front and back of the slits is not straightforward. However, further work is needed to determine the exact dependence of these source strengths to the slit dimensions.

5.7 Sound power reduction

In this final section the total sound power reduction due to the slit compared to the baseline case is investigated. The radiated sound power per unit aerofoil span can be estimated by assuming that the aerofoil, whose span is infinitely long, radiates to the far field as a cylindrical wave with negligible spanwise variations in radiated pressure,

$$P(\omega) = \int_0^{2\pi} I_r(r, \theta, \omega)\, r \mathrm{d}\theta \tag{5.23}$$

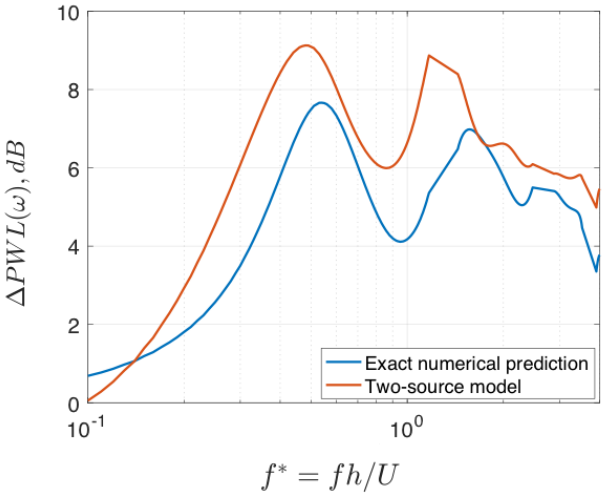

FIGURE 5.8: Sound power predictions for the baseline case and slitted aerofoil, comparing the exact numerical prediction with the two-source model

where $I_r(r, \theta, \omega)$ is the radial component of acoustic intensity transmitted in a uniform mean flow with Mach number M. Following Blandeau ([102]) $I_r(r, \theta, \omega)$ may be determined from the mean square pressure spectrum and the non-dimensional factor $F(\theta, M)$,

$$I_r(r, \theta, \omega) = \frac{S_{pp}(r, \omega, \theta)}{\rho c} F(\theta, M) \tag{5.24}$$

with,

$$F(\theta, M) = \frac{\beta^4 \sqrt{1 - M^2 \sin^2 \theta}}{\left(\sqrt{1 - M^2 \sin^2 \theta} - M \cos \theta\right)^2} \tag{5.25}$$

The predicted sound power reduction is shown in Fig. 5.8 using both the exact surface pressure integration and the radiated pressure obtained from the two-source model.

Agreement between the exact calculation of sound power reduction and that obtained using the simple two-source model are within 2dB over the entire frequency range, thereby supporting the validity of the two source model. Consistent with measurement plotted in Fig. 1.7, negligible noise reductions are predicted in the low frequency limit but increase as frequency increases. Also consistent with the measurements are the peak frequencies of maximum sound power reductions very close to the theoretical frequencies of $f^* = 0.5, 1.5 and 2.5$, with maximum reductions at $f^* =$ 1.5 of 9dB. Even though the detailed pressure directivity functions are complicated functions of frequency and observer angles, Fig. 5.6, after integration over θ, the total sound power reductions are greatest at $f^* = f\tau_H = (2n + 1)/2$. At higher frequencies, however, predicted sound power reductions diminish due to the increasingly large differences between the source strengths at the front and back edges, as shown in Fig. 5.7.

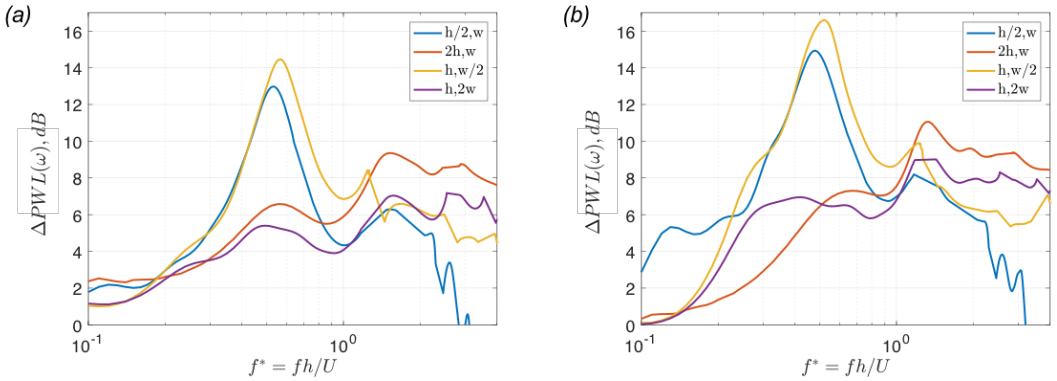

FIGURE 5.9: Sound power predictions for the baseline case and slitted aerofoil, comparing the exact numerical prediction with the two-source model for different slit configurations

5.8 Two-source model results for other slit configurations

In this section, the validity of the two-source model for different combinations of slit lengths and slit widths is investigated. The exact numerical procedure described in Section **??** was repeated for four other slit configurations comprising $(h/2, w)$,$(2h, w)$,$(h, w/2)$ and $(h, 2w)$, where (h, w) corresponds to the original case considered in Sections 4.2 and **??**. Figure 5.9 a) shows the sound power reduction spectra for the different cases plotted against $f^* = fh/U$, computed exactly using Eq. 4.3, while Figure 5.9 b) is the corresponding sound power reduction spectra obtained using the two-source model. The two-source model predictions can be observed to provide reasonable agreement with the exact calculation in all four cases, thereby validating the noise reduction mechanism proposed in this thesis. Of the four cases, the case $(h, w/2)$ gives the largest maximum noise reduction of 14.3dB at $f^* = 0.5$ and the best overall noise reduction of 7dB. Clearly therefore, the noise reduction performance of the slit is highly sensitive to slit length and slit width. A complete parametric study is therefore required to identify the optimum slit parameters.

Chapter 6

Parametric study on slitted leading-edge profiles

This chapter is a numerical study aimed at providing greater insight and understanding into the sensitivity of noise reductions to variations in the slit geometrical parameters h and w. In particular, this chapter investigates the effect on source strength distribution to variations in h and w and elucidates the reason for this effect on source distribution in terms of the fundamental vortex dynamics.

6.1 Scope of the study and normalisation

A flat plate containing leading edge slits interacting with a turbulent flow is completely defined by the four length-scales w, h, λ and turbulence integral length-scale Λ, in addition to the flow Mach number M. As noted above, in this numerical parametric study the impinging vortex is a 2D spanwise vortex that is therefore fully coherent along the span. Finite correlation effects that occur in practice by a fully turbulent flow are therefore absent from these simulations.

In this predominantly numerical study it is therefore chosen, arbitrarily, to normalise the slit length h and width w on the slit wavelength λ. It is emphasised, however, that this choice of normalisation cannot, at present, be justified on physical grounds. Whilst different slit configurations with the same values of h/λ and w/λ are geometrically similar, they will be predicted to produce different noise reductions in this inviscid calculation unless h/Λ is also scaled accordingly.

The parametric study presented in this thesis will focus on the effects on control performance due to variations in h, w and λ but at a constant vortex size Λ as this is the quantity that is determined by external flow conditions.

The slit configurations tested experimentally in Chapter 7 of this thesis are also normalised on λ to allow comparison with the noise reduction predictions obtained numerically. However, it is emphasised that the purpose here is merely to demonstrated that the measured noise reductions follow similar trends with h, w, λ to that obtained numerically. Furthermore, no direct

comparison between the predicted and measured data is possible owing to the very different characteristics of the incoming vortical flows assumed in each study.

6.2 Sensitivity of noise reductions to the slit length

In this section the influence on noise reductions due to variation in slit length is investigated for a fixed width $\lambda/w = 10$. Here, six length were investigated of $h/\lambda = 0.5, 0.83, 1.66, 3.33, 6.66$ and 8.88. Table 6.1 below gives the value of the slit lengths h/λ investigated and their corresponding $h/2\Lambda$ ratio, referring to a normalisation of the slit height by the incoming vortex diameter 2Λ. By way of an overview of the effect of h on source distribution, plots of the RMS surface pressure distribution on the upper side of the flat plate is displayed in Fig. 6.2 for the different lengths and can be compared directly to the pressure distribution on the baseline aerofoil in Fig. 6.1.

TABLE 6.1: Slit configurations with varying height h

h/λ	0.5	0.83	1.66	3.33	6.66	8.88
h/Λ	0.14	0.23	0.46	0.91	1.82	2.4

As noted in Chapter 4 introducing narrow slits has the considerable effect of concentrating the source distribution to the two ends of the slit. The source distribution at the front (leading) edge can be observed to be weaker than at the leading edge of the baseline aerofoil. The RMS surface pressure is observed to strongly decay towards the slit corner, which has been shown to be directly linked to the formation of secondary streamwise vorticity at the slit corner. One of the most important findings from Fig. 6.2 is that the front-edge source distribution appears to be insensitive to variations in slit length h. By contrast, however, the formation of the source at the back edge of the slit is highly dependent on slit length and becomes progressively weaker as the slit height increases. This effect will be discussed in greater detail in Section 6.2.2 below.

Note that the front and back-edge sources for the two shortest slit heights $h/\lambda = 0.5$ and $h/\lambda = 0.83$ cannot be separated and appear as a single source.

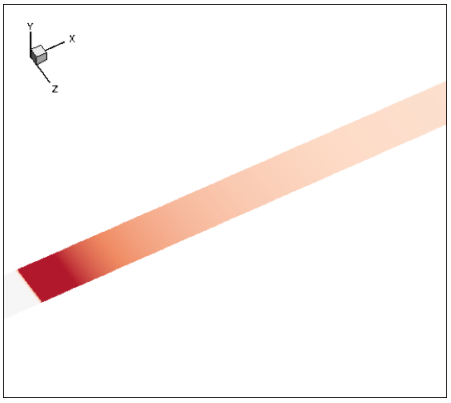

FIGURE 6.1: RMS pressure on the surface: baseline SLE

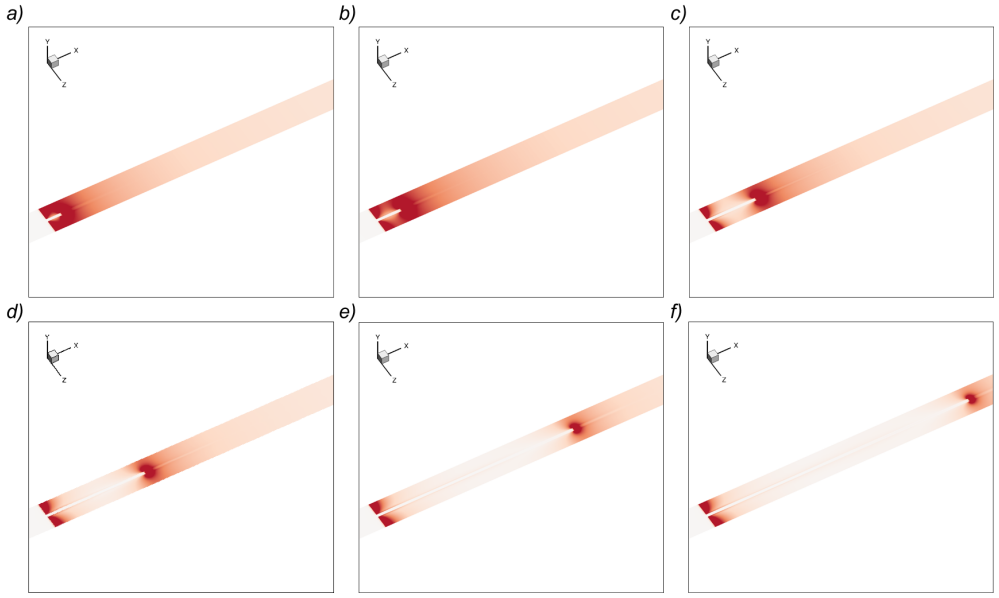

FIGURE 6.2: RMS pressure on the surface: a) $h/\lambda = 0.5$ - b) $h/\lambda = 0.83$ - c) $h/\lambda = 1.66$) - d) $h/\lambda = 3.33$ - e) $h/\lambda = 6.66$ - f) $h/\lambda = 8.88$)

6.2.1 Far field mean square pressure directivity and power reduction

Firstly, an initial assessment of the effect of slit length on control performance is presented by plotting the mean square pressure directivity in Fig. 6.3 for the different slit lengths. Increasing slit length can be observed to provide increasingly greater noise reductions at all angles, particularly in the downstream direction where noise reductions are greatest, where noise reductions can be seen to vary by about 10dB over the range of slit lengths investigated.

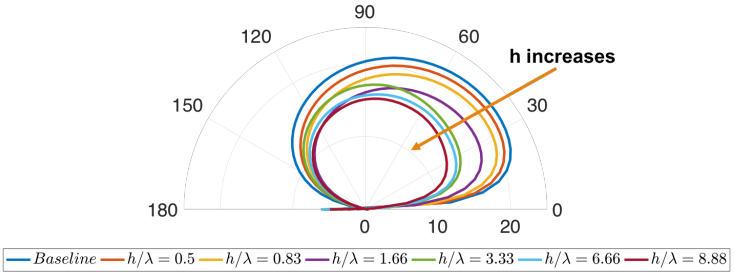

FIGURE 6.3: Mean square pressure directivity for different slit lengths

Using the procedure described in Section 5.7 the total sound power reduction due to the slit compared to the baseline SLE case is shown in Fig. 6.4 for the different slit lengths. The reductions are plotted against non-dimensional frequency fL/c in Fig. 6.4 a), where $L = 1$m and c is the speed of sound and again plotted against non-dimensional frequency fh/U, defined in relation to the slit height and flow speed.

The sound power reduction spectra plotted in Figures. 6.4 a) and b) exhibit a number of peaks at which noise reductions are greatest. By observing that these peaks occurred close to fh/U=(2n-1)/2, Chaitanya et al has speculated, based on measured reduction spectra, that this behaviour is due to the destructive interference between two compact sources at either ends of the slit [4]. This mechanism was confirmed in Chapter 5 in numerical simulations of a single representative test case. Based on the surface pressure distributions plotted in Fig. 6.2, this mechanism appears to be valid for the range of slit lengths investigated. It is noted that even though the two sources cannot be separated in terms of RMS pressure for the two shortest lengths considered, a peak in the noise reduction spectra is well defined. Clearly, therefore the two sources are still well separated for these two short slit cases in a narrow frequency band centred on the spectral peaks.

When plotted against frequency unrelated to h, Fig. 6.4 a) the spectral peaks are observed to shift towards lower frequencies as the slit length h increases.

When re-plotted against fh/U in Fig. 6.4 b) the spectral peaks now all collapse on $fh/U = 0.5$, with the second and third peaks at $fh/U = 1.5$ and 2.5 being less well defined, particularly for the short slit cases where these peaks occur at a relatively high absolute frequency where the mesh resolution is insufficient. Note that at this main peak no clear trend between noise reduction level and slit length can be observed, since these peaks all occur at different frequencies f. However, a simple relationship between slit height and noise reductions integrated across all frequencies is now demonstrated.

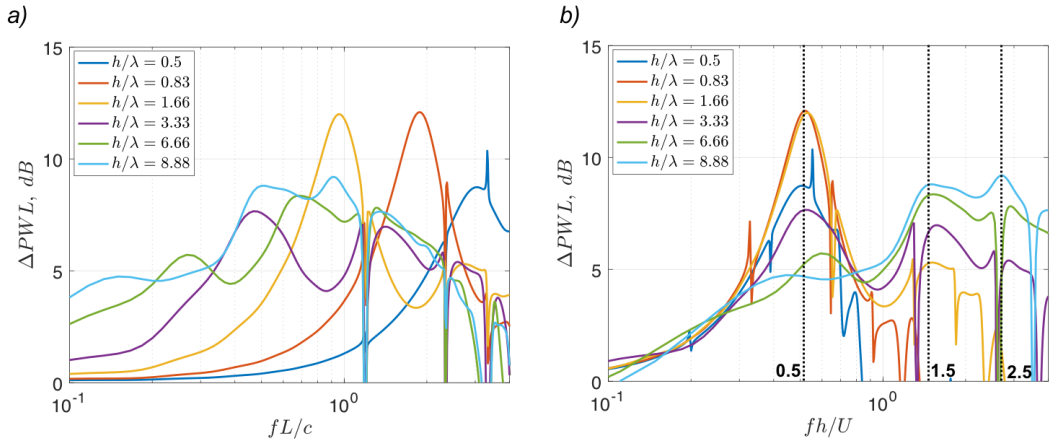

FIGURE 6.4: Power difference spectrum for different slit lengths: a) against non-dimensional frequency fL/c - b) against non-dimensional frequency fh/U

The overall power reduction versus slit length h/λ is plotted in Fig. 6.5 on a logarithmic scale. Whilst the individual noise reduction spectra in Fig. 6.4 exhibits no clear dependence on h, increasing the slit length can be seen to provide increasingly better overall noise reductions. Moreover, overall sound power reductions closely follow straight-line behaviour suggesting a power law h^n dependence. Also shown for comparison is the line $\sqrt{h/\lambda}$, suggesting that, for this choice of w and λ, overall noise reductions varies with h as $h^{1/2}$.

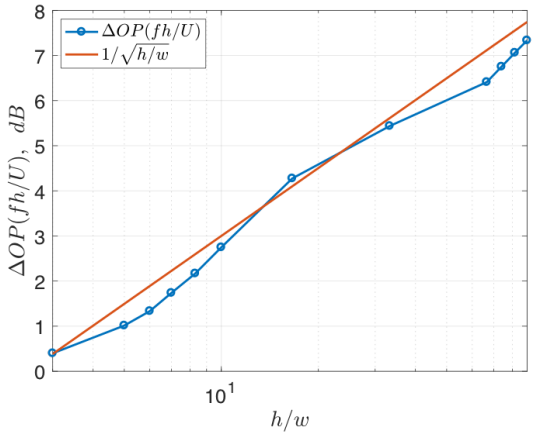

FIGURE 6.5: Overall power reduction against h/λ

6.2.2 Source distribution on the surface

The source distribution over the flat plate surface is now examined for the different slit widths in an attempt to understand the mechanism by which longer slits can provide progressively better noise reductions.

6.2.2.1 Source strength balance

In this section the balance of source strengths at either ends of the slit is examined as h is increased. Figure 6.6 shows the variation of the mean square surface pressure integrated over the front and back regions of the flat plate versus h/λ. The front region is taken to be the area between the leading edge and $2h/3$ from the leading, while the back edge region is taken to be the remaining area further downstream. Also shown for comparison is the sum of integrated mean square pressure at the front and back, together with the mean square pressure integrated over the entire surface of the baseline plate.

The source strength at the front of the slit (blue curve) can be seen to remain roughly constant for $h/\lambda > 3.33$ and to decay for values below this. This behaviour is due to the difficulties in separating the source strengths between the front and back for these short slit cases. The source separation procedure is there inaccurate and only the sum of their source strengths provides useful information.

The total integrated source strength can be observed to decay with increasing h, consistent with the increasing power reduction observed in Fig. 6.5. The breakdown in source strengths indicates that this reduction in total source strength arises only from the reduction in source strength at the back-edge, while that at the front edge remains roughly independent of h.

6.2.2.2 Secondary vortices

Results from Chapter 5 on the mechanisms of noise reduction for slitted leading edges have shown that the source strengths at the back and front of the slit are due to a combination

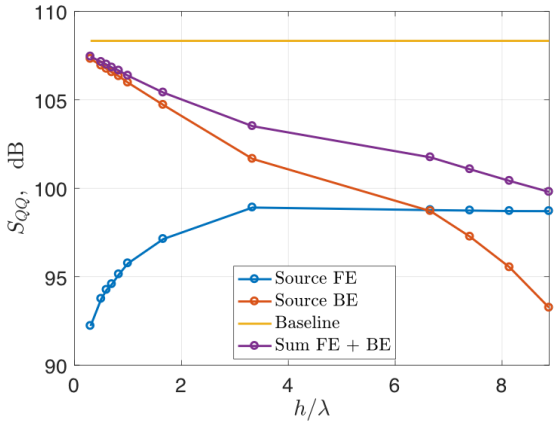

FIGURE 6.6: Integrated source strength over frequencies at the front and back edges against h/λ

of the spanwise vorticity due to the impinging vortex and the secondary streamwise vorticity generated at the slit corners. The spanwise vorticity along the back edge may be assumed to remain independent of slit length since the impinging vortex simple convects unchanged along the plate. The main effect of increasing the slit length is therefore to modify the behaviour of the secondary streamwise vorticity as it reaches the back-edge, causing a reduction in the source strength.

Figure 6.7 shows contour plots of the streamwise vorticity in the $x_2 - x_3$ plane at the back edge streamwise location $x_1 = h$. The figure shows vorticity contour plots as the point A of maximum downwash velocity, shown in Fig. 3.3, reaches the back-edge, for the six different slit lengths.

To understand the behaviour observed in Fig. 6.7 it is noted that the streamwise vorticity at the back edge has two contributions. The first is due to streamwise vorticity generated at the front edge convected with the main vortex towards the back edge. The second contribution is the streamwise vortivity generated directly at the back edge due to the impinging main vortex.

As the slit length is increased the two vortex contributions can be seen to separate whereby the front edge vortex moves increasingly further from the surface. The three longest slits in Fig. 6.7 show this behaviour most clearly. The resultant streamwise vorticity on the surface therefore decreases as the slit length is increased. This observation is consistent with the decrease of source strength at the back-edge.

6.2.3 Role of source interference on the far-field noise reductions

Previous work from [4] and the results from Chapter 5 have identified two main mechanisms responsible for the noise reductions provided by slitted aerofoils. One is due to a reduction in the source strength over the aerofoil surface, the other is due to destructive interference occurring between two compact sources at either ends of the plate. To quantify the relative contributions from the two mechanisms to the overall noise reductions, the radiated power obtained by summing the radiation from the front and back edges coherently, i.e., allowing for interference, was compared against that when summed incoherently in which the effects of interference are

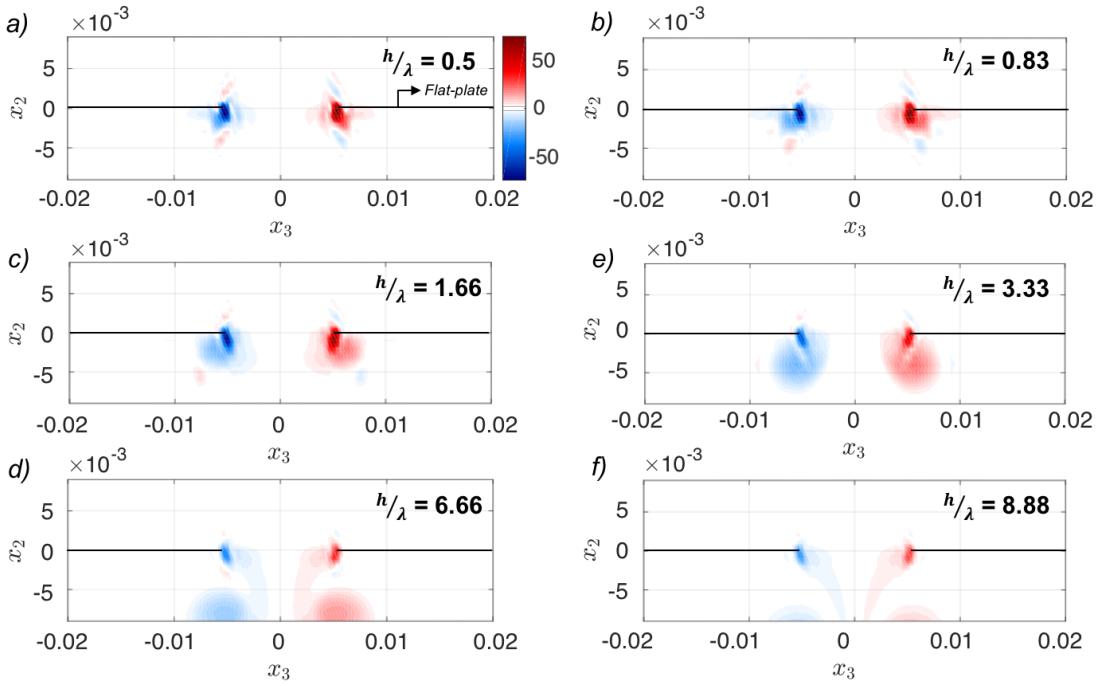

FIGURE 6.7: Contour-plots of the streamwise vorticity in the $x_2 - x_3$ plane as the point A of maximum downwash reaches the back-edge, for different slit lengths

excluded.

A comparison of the overall sound power reduction obtained with and without interference is represented in Fig. 6.8 for all slit lengths. It can be observed that, in general, interference effects on the noise reduction spectrum are weak except for the slit lengths of $h/\lambda = 0.5, 0.83, 1.66$ in which the effects of interference are confined to narrow frequency bands centred on $(fh/U = 0.5)$.

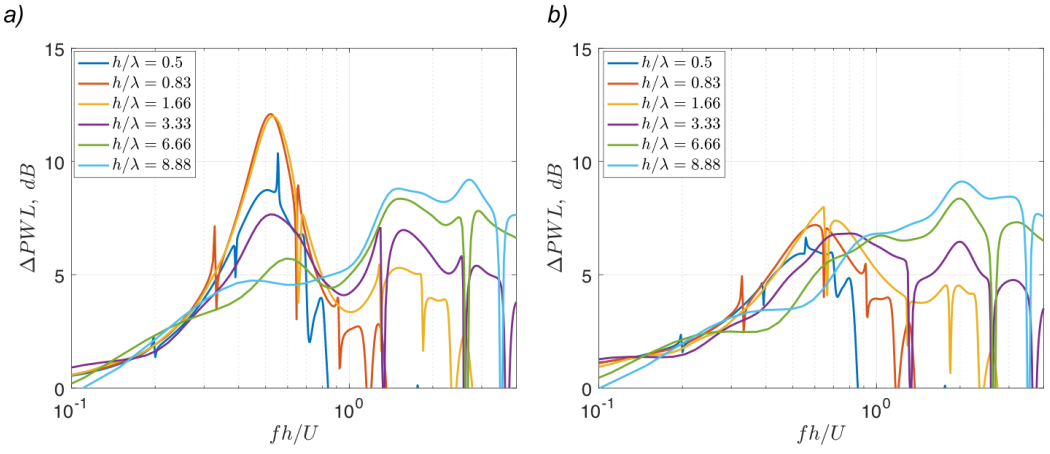

FIGURE 6.8: Sound power reductions with/without interference for different slit lengths plotted against fh/U

However, the effect on overall noise reduction (integrated across frequencies) is significantly less as observed in Fig. 6.9 which shows the overall sound power reduction plotted against h/λ

with and without the inclusion of interference effects. The deviation between these results are generally less than $1dB$ suggesting that reductions in the source strength are the dominant noise reduction mechanisms on slitted leading edges. In order to makes this association more obvious, the sound power reduction with interference effects includes are plotted against h/λ in Fig. 6.10 and compared against the corresponding reduction in total source strength (calculated from Fig. 6.6). Also shown in this figure is the difference in power reductions plotted in Fig. 6.9. Levels of reductions in radiated power and source strength agree to within 2dB providing direct confirmation that the main noise reduction mechanism is due to a reduction in the source strength rather than the effects of source interference. Clearly, the value of h/λ at which the contribution to overall noise reductions due to interference are greatest ($h/\lambda = 1.66$) is also the case for which the difference between power reductions and source strength is greatest.

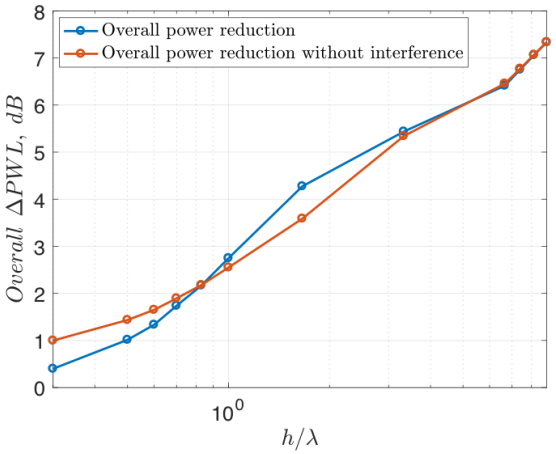

FIGURE 6.9: Overall power reduction against h/λ: front and back-edge propagated separately to exclude any interference between the two source regions

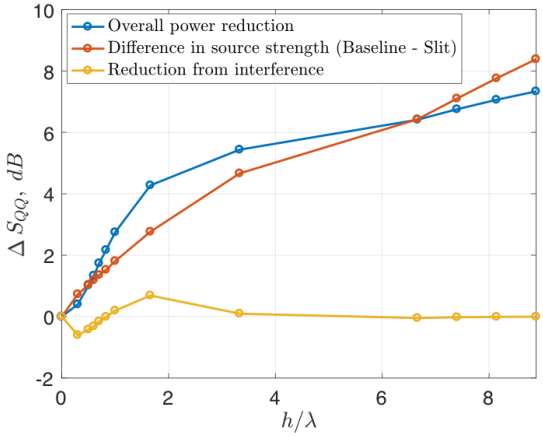

FIGURE 6.10: Comparison between the difference in source strength (baseline - slit), the overall power reduction and the reduction provided by destructive interference - plotted against h/λ

6.2.4 Trends for other slit widths

The variation of sound power reductions with slit length was also investigated for the two different slit widths $w/\lambda = 0.05$ and $w/\lambda = 0.2$. The overall sound power reduction obtained for these cases is shown in Fig. 6.11. Also shown on this figure is the data from Fig. 6.5. As before, increasing the slit length provides monotonically improved overall noise reductions but with the important difference that increasing the width produces a slightly slower variation than $h^{1/2}$ while it varies slightly faster when the slit width is reduced.

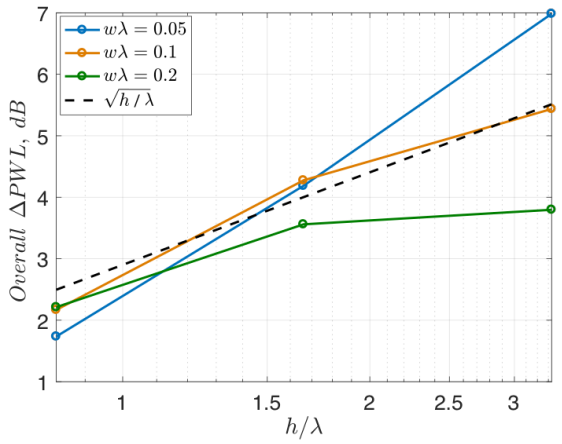

FIGURE 6.11: Overall power reduction against h/λ for different slit widths

6.3 Sensitivity of noise reductions to slit width w

In this section the influence of the slit width on the noise reduction is investigated. The noise prediction procedure described above was repeated for the six slit widths of $w/\lambda = 0.025, 0.05, 0.1, 0.15, 0.2, 0.4$, while maintaining a constant value $h/w = 33.3$. Table 6.2 below gives the value of the slit widths w/λ investigated and their corresponding $w/2\Lambda$ ratio, referring to a normalisation of the slit height by the incoming vortex diameter 2Λ. The sensitivity of the surface pressure fluctuations to slit width is first investigated. Contour plots of the RMS surface pressure for the six cases is displayed in Fig. 6.12. For the narrowest slit $w/\lambda = 0.025$, the sources are most concentrated towards the front of the slit. However, as the slit width is increased the source strength at the front edge becomes weaker while becoming stronger at the back edge.

TABLE 6.2: Slit configurations with varying height w

w/λ	0.025	0.05	0.1	0.15	0.2	0.4
w/Λ	0.0068	0.014	0.027	0.041	0.054	0.11

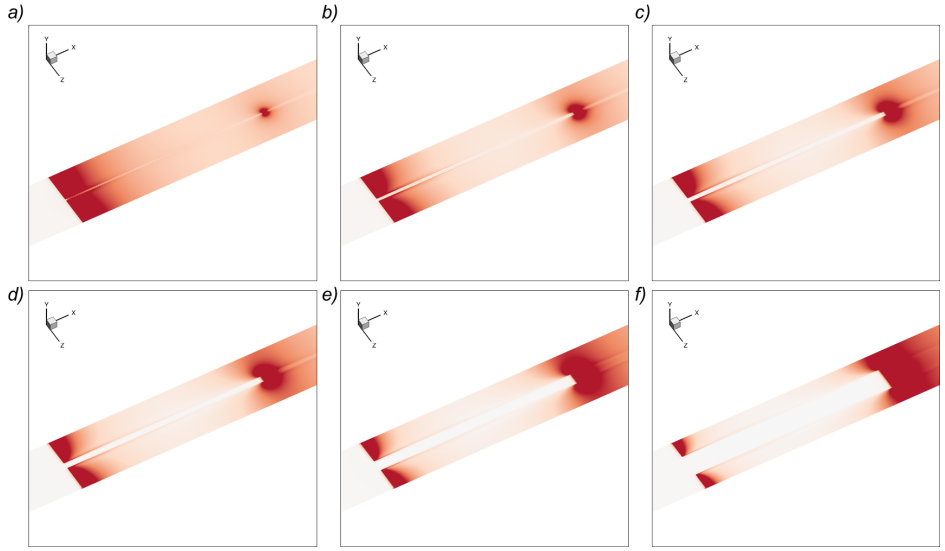

FIGURE 6.12: RMS pressure on the surface: a) $w/\lambda = 0.025$ - b) $w/\lambda = 0.05$ - c) $w/\lambda = 0.1$ - d) $w/\lambda = 0.15$ - e) $w/\lambda = 0.2$ - f) $w/\lambda = 0.4$

6.3.1 Sound power reduction

The sound power reduction versus w/λ is shown in Fig. 6.13 for the six slit widths plotted against fh/U. This figure reveals the large sensitivity of the noise reductions to slit width. An optimum slit width is clearly observed, corresponding to $w/\lambda = 0.05$ where maximum noise reductions of up to 14dB are predicted to close to $fh/U = 0.5$. An optimum value of slit width must exist since there must be zero sound power reductions in the limiting cases of $w/\lambda \to 0$ where the presence of the slit becomes negligible and $w/\lambda \to 1$ where the slit becomes a straight edge shifted downstream at $x_1 = h$.

In order to quantify more carefully the dependence of the noise reductions to slit width, overall sound power reductions are plotted against w/λ in Fig. 6.14. A relatively sharp optimum is observed in which power reductions rapidly increase with increasing w/λ until the optimum value of $w/\lambda = 0.05$ to reach 7dB and then gradually decays towards to 0dB at values of w/λ above this.

6.3.2 Surface source distribution

6.3.2.1 Source strength balance

The previous section has highlighted the existence of a clear optimum slit width at which maximum noise reductions occur. The reason for this optimum slit width is now explored by examining the balance of source strengths at the front and back edge regions following the same procedure described in Section 6.2. The variation in front and back edge source strengths are plotted against w/λ in Fig. 6.15. Also shown in this figure is the sum of the source strengths and the baseline source strength. The front edge source strength can be observed to decay rapidly with increasing w/λ, which must eventually tend towards 0 (i.e., -∞ dB) as $w/\lambda \to 1$. The

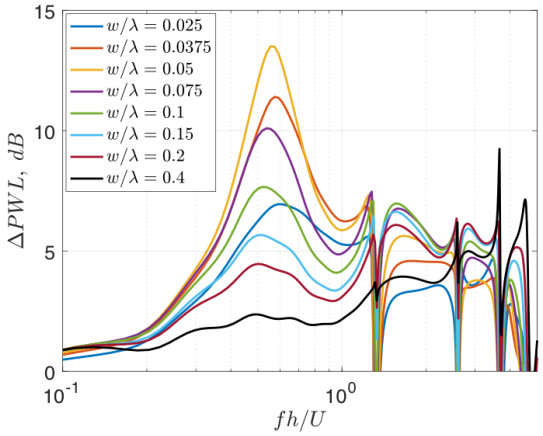

FIGURE 6.13: Power difference spectrum for different slit widths against non-dimensional frequency fh/U

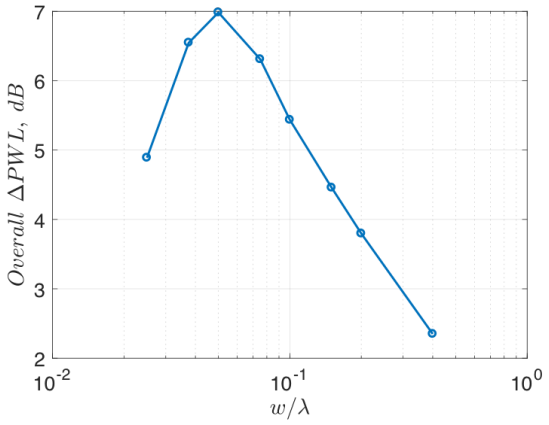

FIGURE 6.14: Overall power reduction against w/λ

back edge source strength, however, increases more slowly with increasing w/λ as it must tend towards the baseline source strength as $w/\lambda \to 1$.

It is noted that the optimum value of $w/\lambda = 0.05$ in overall noise reduction corresponds very closely to the minimum radiation at the back-edge. At this optimum value of $w/\lambda = 0.05$ the front-edge source strength is about 5dB lower than at the back-edge. The existence of an optimum slit width is therefore predominantly due to the variation in back-edge source strength with slit width. The reason for this behaviour will be explored further below.

It is noted that for this geometry the source strength at the front edge appears to vary with w as w^{-1} while it varies as $w^{1/2}$ at the back edge. It is presently unclear how universal this behaviour is for other slit lengths but similar behaviour was previously identified for one other slit length in [106].

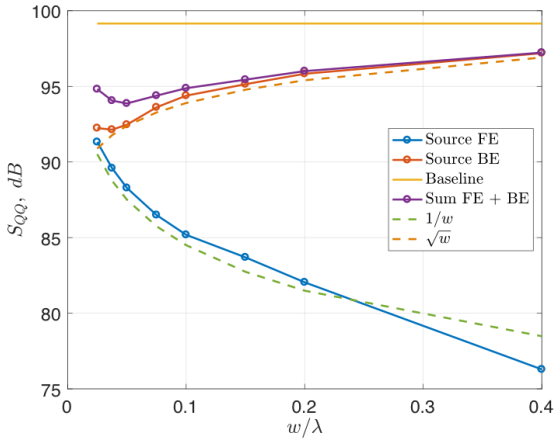

FIGURE 6.15: Integrated source strength over frequencies at the front and back edges against w/λ

6.3.2.2 Influence of secondary vortices on back-edge source strength

In order to understand the variation of back-edge source strength with slit width the pressure generated along the back-edge of the slit is directly compared to the corresponding spanwise vorticity occurring along the back edge at the instance in time when the main vortex impinges the back-edge. The two quantities are plotted in Fig. 6.16 a) and b) for the six slit widths against normalised distance along the back edge x_3/w respectively across the whole computational spanwise domain.

It can be noticed that the level and variation with x_3 of pressure fluctuations at the back edge of the slit are strongly related to the slit width. The pressure fluctuations can be observed to decay sharply at the edges of the slit $x_3/w = \pm 1/2$ due to the formation of localised streamwise vorticity in these regions.

Explanation for these findings can be found in the corresponding variation of spanwise vorticity plotted in Fig. 6.16 b). A direct and close relationship between the variation in pressure and spanwise vorticity is evidently suggested by the almost-identical variations in their respective profiles.

Whilst the overall integrated source strength is simply related to w as shown in Fig. 6.15, pressure and vorticity profiles for individual slits are more complicated and suggest complex behaviour occurring within the vortex system itself, which is described below.

Figure 6.17 shows a sketch of the streamwise vorticity to illustrate its effect on the spanwise vorticity profiles extracted from Fig. 6.16 b) for three different slit widths $w/\lambda = 0.4$, $w = 0.1$ and $w = 0.025$. It can be noticed that for the largest width, the streamwise vortices are more concentrated at the slit corners, which induces an additional downwash on the upper surface, consistent with the increase in spanwise vorticity and pressure profiles at the slit corner. For the middle-size slit width $w/\lambda = 0.1$, the pair of streamwise vortices becomes relatively closer together and therefore both vortices create an additional downwash at around the same location at the middle of the slit, generating the bell-shaped pressure and vorticity profiles of greater

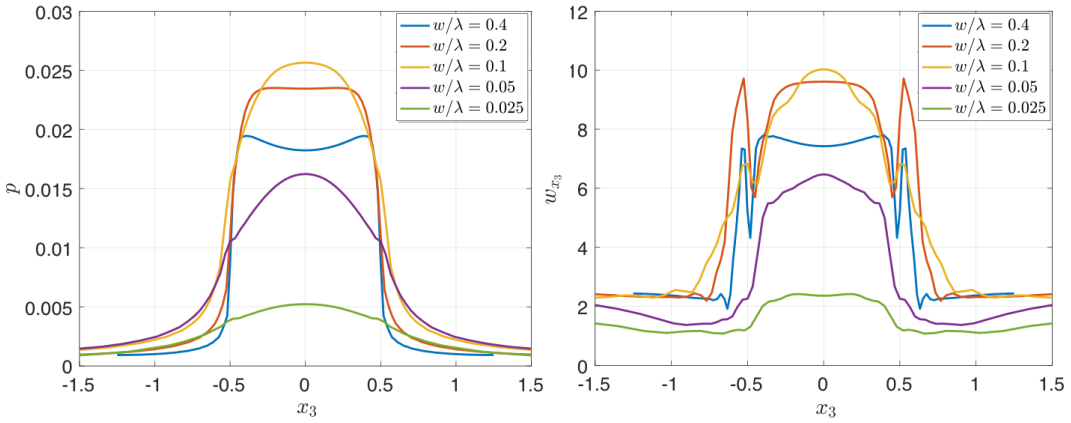

FIGURE 6.16: a) Pressure generated along the back-edge at the instance in time when the main vortex impinges the back-edge, for different slit widths b) Corresponding spanwise vorticity - plotted against normalised distance along the back edge x_3/w across the whole computational spanwise domain.

amplitude. For the smallest slit width under consideration $w/\lambda = 0.025$, the two streamwise vortices rotating in opposite directions superimpose. As a result, the response is lower due to cancellation effects.

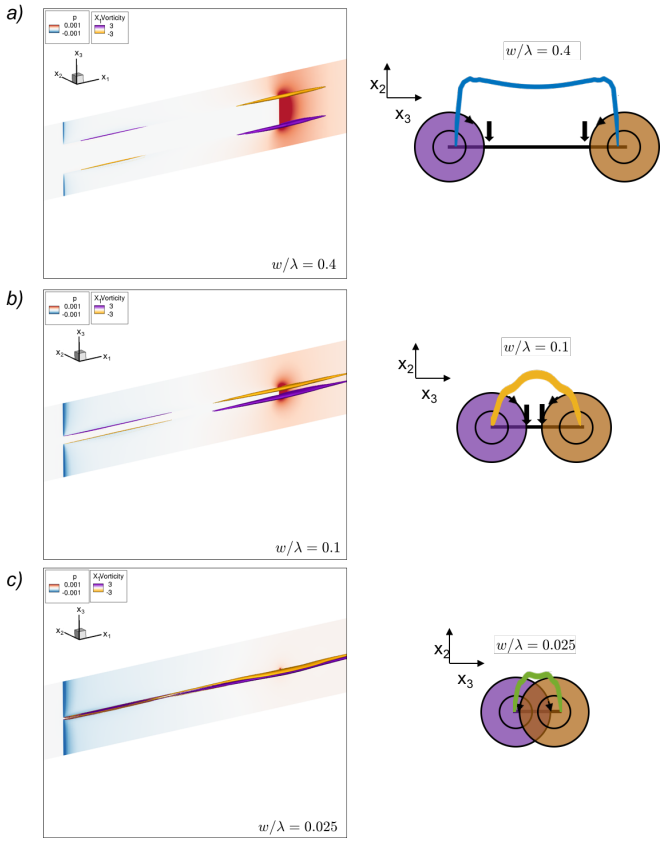

FIGURE 6.17: Sketch of the streamwise vorticity and its effect on the spanwise vorticity profiles extracted from Fig. 6.15 b) for three different slit widths $w/\lambda = 0.4$, $w/\lambda = 0.1$ and $w/\lambda = 0.025$

6.3.3 Role of source interference on the far-field noise reductions

In order to establish the relative contributions to overall noise reductions from reductions in the source strength and the effects of destructive interference, an identical procedure is followed to that presented in Section 6.2.3 for the variation in slit length. Similar to Fig. 6.10, the variation in sound power reduction plotted against w/λ is represented in Fig. 6.18. Also shown is a breakdown of this noise reduction into the effects due only to interference and due only to source reduction.

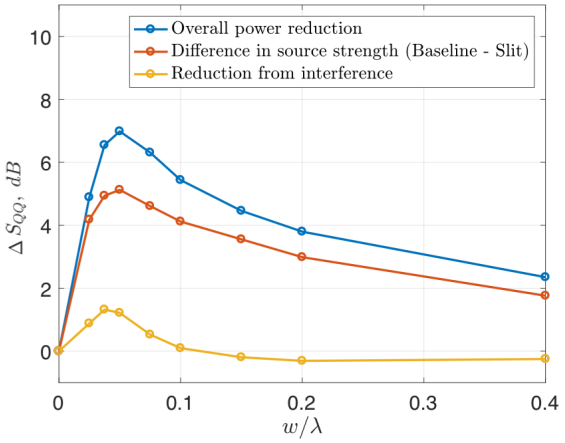

FIGURE 6.18: Comparison between the difference in source strength (baseline - slit), the overall power reduction and the reduction due to destructive interference - plotted against w/λ

As in Section 6.2 in which the variation of noise reduction with h is investigated, it is noted again that overall noise reductions are principally determined by the reductions in overall source strength with the effects of interference contributing no more than about 2dB. Reductions in source strength are therefore maximum at the optimum width $w/\lambda = 0.05$. It is noted that noise reductions due to interference also peak at this slit width implying that the source strengths must match at $fh/U = 2n + 1$ for this particular width. However, this is believed to be coincidental as there is no physical reason why a minimum value in overall source strength should lead to the two source strengths being equal at these discrete frequencies.

6.3.4 Variation with w for other slit lengths

The noise reduction spectra was calculated versus slit for two other slit lengths that are 1/2 and 1/4 of the length in the previous slit geometry investigated above. The overall power reduction versus w/λ for these cases and the original case are compared in Fig. 6.19. The curves for all three slit lengths exhibit an optimum value of w at which maximum noise reductions occur, which appears to decrease as the slit length is increased. The optimum slit geometry therefore has an increasingly large aspect ratio h/w as the slit length is increased. As observed in Section 6.2, for a fixed slit width, noise reduction generally improve as the slit length is increased.

Overall nose reductions become progressively better as the slit length is increased, while a distinct optimum value in slit width is observed, which becomes smaller as the slit length is increased.

To summarise this behaviour, a contour plot of overall noise reductions is plotted in Fig. 7.7 in Chapter 7 against slit width and slit length.

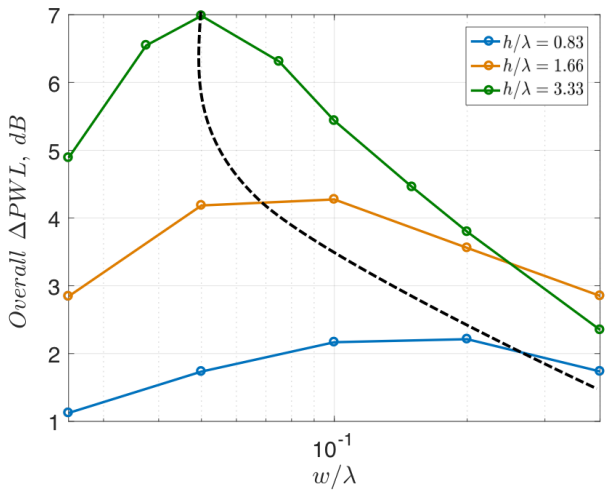

FIGURE 6.19: Overall power reduction against w/λ for different slit lengths

6.4 Sensitivity of noise reductions to slit wavelength λ

This section concerns the sensitivity of the noise reductions to variations in the slit wavelength λ, i.e., the distance between adjacent slits. Clearly, noise reductions will be poor if λ is too large and there are insufficient slits along the span. However, if λ is too small, then effects of mutual interact between adjacent slits may also degrade the noise reduction performance.

The previous section investigating the effects of slit width has suggested the possible existence of an optimum ratio between slit width and wavelength. In this study the slit width is kept constant but the wavelength λ varies such that the ratio w/λ varies between 0.02 and 0.2, which is below and above the optimum value of about 0.1.

A general overview of the effect of slit wavelength to acoustic performance is shown in Fig. 6.20 in which the RMS pressure distribution is plotted over the surface of the flat plate for four wavelengths, corresponding to $w/\lambda = 0.0250, 0.05, 0.1, 0.2$. Note that to allow direct comparison between the four cases the surface pressure are shown for the same area corresponding to the largest wavelength. Also shown in this figure is the baseline case for comparison.

Increasing the serration wavelength can be seen to have the opposite effect to increasing the slit width (Fig. 6.12). A significant reduction in source strength at the front of the slit can be observed for the two smallest wavelengths with relatively larger source strengths at the back. As the wavelength is increased, and the slits become relatively further away from each other, the pressure distribution at the front edge appears to tend towards that of the baseline case.

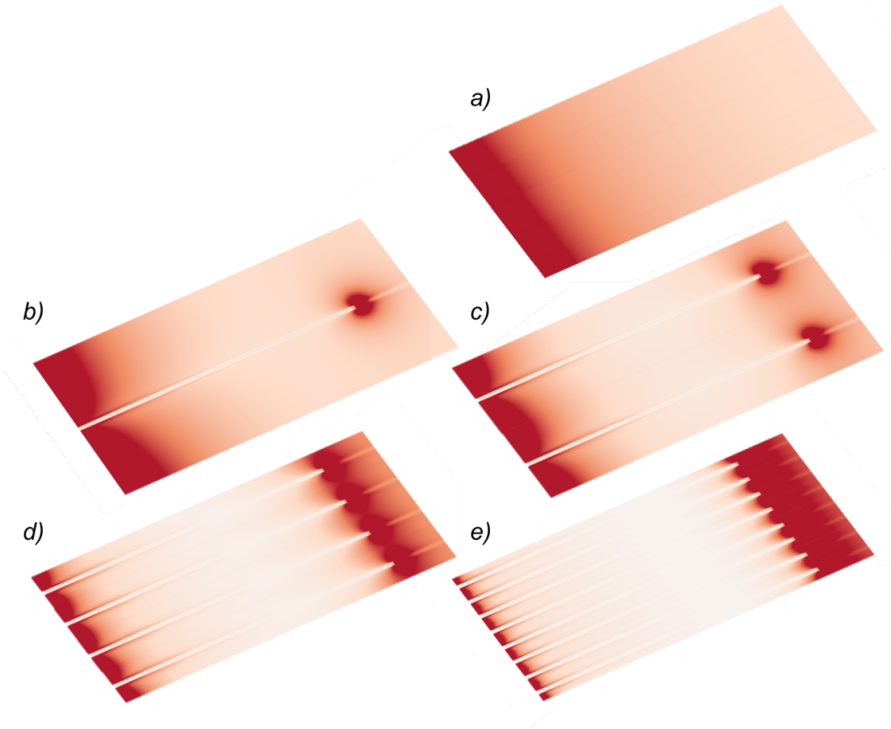

FIGURE 6.20: RMS pressure on the surface: a) baseline - b) $w/\lambda = 0.025$ - c) $w/\lambda = 0.05$ 1.66) - d) $w/\lambda = 0.1$ - e) $w/\lambda = 0.2$

6.4.1 Sound power reduction

The variation in overall sound power level reduction with the wavelength λ at fixed w is plotted in Fig. 6.21 versus w/λ. Also shown for comparison is the sound power level reduction plotted previously in Fig. 6.14 when varying w while keeping λ constant. Note that the two curves at the optimum value of w/λ=0.05 correspond to identical slit dimensions.

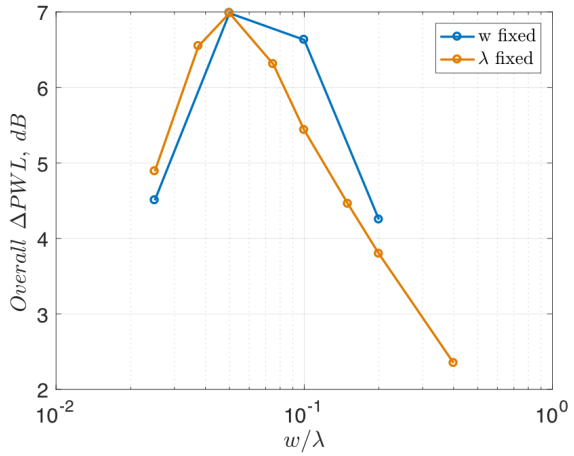

FIGURE 6.21: Variation in overall sound power level reduction with the wavelength λ at fixed w, plotted against w/λ

The curves can be observed to follow very similar behaviour, peaking at $w/\lambda = 0.05$ (to within the resolution limits of the simulations). Clearly, therefore the ratio of slit width to slit wavelength is a critical factor in determining the noise reduction effectiveness of the leading edge slits. Clearly, therefore increasing w has an almost identical effect on noise reductions as decreasing λ in inverse proportions. It is noted that in Fig. 6.21 there are three cases in which the ratio w/λ are identical (0.025, 0.1 and 0.2) but obtained for different values of width and wavelength. Although these case are geometrically similar their noise reductions are not identical. This is because the size of the incoming vortex has been kept constant and therefore these cases of same ratio are not completely geometrically identical. The creation of secondary vorticity along the slit edges, which is likely to be affected by numerical viscosity in the calculation, may also be an additional cause of the difference in noise reductions for the slits of the same w/λ.

6.4.2 Source strength balance

In this section the identical procedure to that outlined in Section 6.3.2 is followed, aimed at exploring the balance of source strength between the front and back of the slit for varying slit wavelengths. Figure 6.22 is a plot of the variation in the integrated source strength at the front and back edges of the slit versus w/λ. Also shown are the baseline case and the sum of source strengths. Superimposed on this figure is the corresponding data plotted previously in Figure 6.15 in which w is varied for constant λ. The two sets of data can be observed to closely agree, except at the large values of w/λ for the front edge in which the levels are very small. This comparison therefore once again confirms that the ratio w/λ is one of the principal factors that governs the noise reduction performance of the slits.

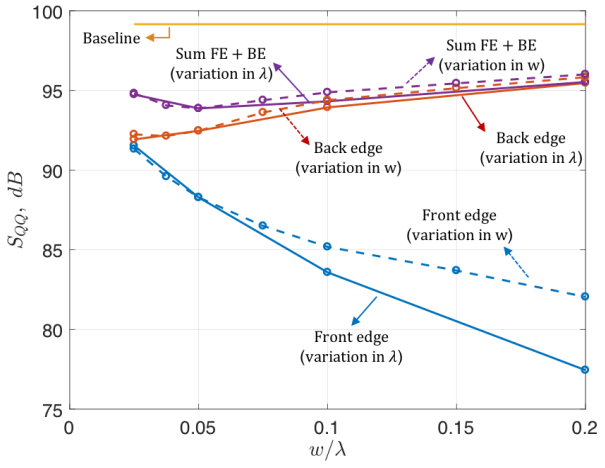

FIGURE 6.22: Integrated source strength over frequencies at the front and back edges against w/λ, for the fixed w cases and the fixed λ cases

Chapter 7

Experimental validation of slitted leading edges profiles

The optimum slit configuration has been implemented on a flat-plate aerofoil and tested in an open jet wind tunnel. The far-field radiation is measured and compared to the numerical predictions presented in Chapter 6.

Previous sections have provided guidelines on the design of slit geometries for the effective reduction of leading edge interaction noise. An optimum value of w/λ of about 0.05 has been identified. Furthermore, noise reductions have been demonstrated to generally improve as the slit length is increased. This section is aimed at providing direct experimental confirmation of these findings in which the radiated noise from a slitted flat plate is located within the turbulent stream of an open jet wind tunnel and compared against the noise due to a baseline flat plate with straight edge.

It is noted that direct comparisons of the predicted and measured noise reductions are not possible owing to the very different spectral characteristics of the incoming vortical flows used in each. The numerical simulations were based on a single idealised 2D spanwise vortex in which adjacent slits are excited coherently. Moreover, the velocity spectrum decays at a rate of $f^{-}10$ at frequencies above $f\ \Lambda/U$, where Λ is the vortex radius, thereby biasing the overall noise reductions towards low frequencies. In the experiment, however, the incoming flow is a close approximation to idealised homogeneous isotropic turbulence in which the decay rate of the velocity spectrum at frequencies above $f\ \Lambda/U$ is much slower at $f^{-5/3}$. Furthermore, the turbulent flow has a finite spanwise correlation length Λ and therefore adjacent slits may be incoherently excited depending on the slit wavelength λ compared to Λ.

7.1 Experimental set-up and wind-tunnel facility

Far-field noise measurements were conducted in the open-jet wind tunnel facility of the ISVR. Figure 7.1 shows a photograph of the facility within the anechoic chamber, of dimension 8 m x 8 m x 8 m. The walls are acoustically treated with glass wool wedges and the lowest cut-off

frequency is 80 Hz. A centrifugal fan is mounted on the ceiling of the chamber, driven by a variable speed 110 kW motor, which provides air for the test facility. Air passes through a series of silencers to ensure a quiet, uniform and low-turbulence flow. The air is then passed through a nozzle of area ratio 25:1 to minimize the lateral velocity fluctuations. The dimensions of the nozzle are 0.15 m and 0.45 m. A detailed sketch of the wind tunnel is presented by [107]. To maintain two-dimensional flow around the aerofoil, side plates are mounted to the nozzle exits which will also support the aerofoil in the flow. Aerofoils are located 0.15 m downstream of the nozzle and the maximum flow speeds performed was 80 m/s. In order to prevent tonal noise generation due to Tollmien–Schlichting waves convecting in the laminar boundary layer, the flow near the leading edge was tripped to force transition to turbulence using a rough band of tape upstream of the trailing edge of the flat plate, on both sides.

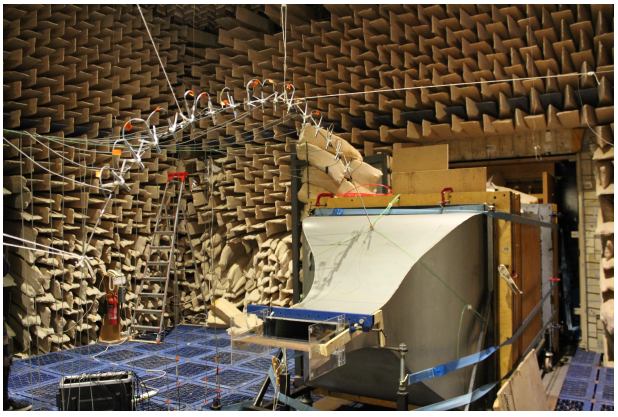

FIGURE 7.1: Open-jet wind tunnel facility of the ISVR

7.1.1 Far-field measurements

Free-field noise measurements were made by using 16, half-inch condenser microphones (BK type 4189) located at a constant radial distance of 1.2 m from the mid-span of the flat plate leading edge. These microphones are placed at emission angles between 40° and 140° measured relative to the downstream jet axis, as shown on Fig. 7.1. The microphones are connected to an amplifier which is manufactured in-house, and then to a National Instruments PXI 1042 chassis. The data acquisition is controlled via laptop which is connected via express card NI 8360. Three NI PXI-4472 Data Acquisition Cards are available which provided 24 channel to acquire the data at the same time. The available sampling rate per each channel is around 102.4 kS/s. Measurements were taken for 10 s duration at a sampling frequency of 50 kHz, and the noise spectra was calculated with a window size of 1024 data points corresponding to a frequency resolution of 48.83 Hz and a BT product of about 500, which is sufficient to ensure negligible variance in the spectral estimate. The acoustic pressure at the microphone was recorded at the mean flow velocities (U) of 20, 40, 60 and 80 m/s. Far- field microphones are calibrated using BK 4231 calibrator to obtain the correct sensitivities. Noise reductions are presented in terms of the sound power level spectra (PWL) calculated by integrating the pressure spectra over the polar array of 16 microphones using the procedure described in [82]. The background noise is at least 10 dB below the airfoil noise, which can be observed on Fig. A.8 in [2].

7.1.2 Turbulence Characterization

A bi-planar rectangular grid with overall dimensions of 630 x 690 mm^2 located in the contraction section of the nozzle was used to generate turbulent that is a close approximation to homogeneous and isotropic turbulence. The spectrum of the hot wire velocity measured at 145 mm from the nozzle exit is in close agreement with the von-Karman spectrum for homogeneous and isotropic turbulence with a 2.5% turbulence intensity and a 7.5 mm integral length scale. The turbulence spectra is given in Fig. 7.2.

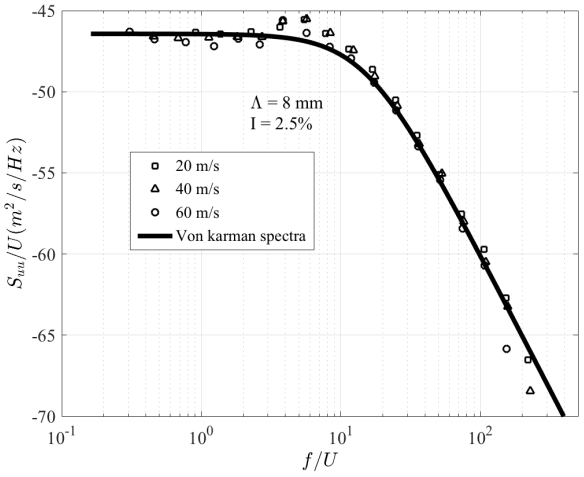

FIGURE 7.2: Spectrum of the hot wire velocity compared with the von-Karman spectrum

7.1.3 Flat plates with slitted leading-edges

The flat plates were constructed from two metallic flat plates of 1mm thickness each that allows an acrylic sheet of 2mm thickness with slitted leading edge to be inserted between them. This arrangement allows for different slit geometries to be tested quickly. The flat-plate has a chord of 150mm and span of 450mm. All corners were rounded and the trailing edge sharpened to eliminate vortex shedding noise. A picture of three flat-plates with different slitted leading-edge profiles is provided in Fig. 7.3 as an illustration, showing from top to bottom: (h = 20mm, w = 8mm, = 30mm) with a ratio $w/\lambda = 0.27$; (h = 20mm, w = 2mm, = 10mm) with a ratio w/λ = 0.2 and (h = 40mm, w = 1.75mm, = 10mm) with a ratio $w/\lambda = 0.175$.

7.2 Overall noise reductions for different slitted configurations

7.2.1 Variation with slit length

Firstly, the effects of slit length on noise reductions are investigated experimentally. In this investigation h was varied between 10mm and 60mm for 5 different slit widths of w=1mm, 3mm,

FIGURE 7.3: Flat plates with different slitted leading-edge profiles fabricated using a 3D printer

5mm, 6mm and 9mm and 2 different wavelengths of =10mm and 30mm. Note that not all possible combinations were tested to avoid those geometries known not to be effective. Figure 7.4a) shows the overall sound power reductions versus h/λ for the different widths corresponding to $w/\lambda = 0.1, 0.2, 0.3$ at the slit wavelength of λ=10mm. Note that these measurements were made at a flow speed of U=40m/s although the noise reduction spectra has been shown to be weakly dependent on U when plotted against fh/U. Figure 7.4b) shows the corresponding results at the larger wavelength of λ=30mm but for all five slit widths of between $w/\lambda = 0.033$ and 0.3.

As observed in the numerical predictions in Fig. 6.5 and 6.11 overall noise reductions generally improve as the slit length is increased at a rate of approximately $h^{-1/2}$ for most cases. This scaling law is indicated as dashed lines in Fig. 7.4, which appears to provide a reasonable approximation to the behaviour of the experimental data.

The noise reductions for the two wavelengths in Fig. 7.4 a) and b) are both greatest for w/λ=0.1 but become progressively worse for ratios w/λ deviating from this optimum value. It is noted that the noise reductions with these same optimum ratios of w/λ=0.1 in figures a and b are different suggesting that the slit wavelength also plays a role in determining control performance. This behaviour will be explored experimentally below.

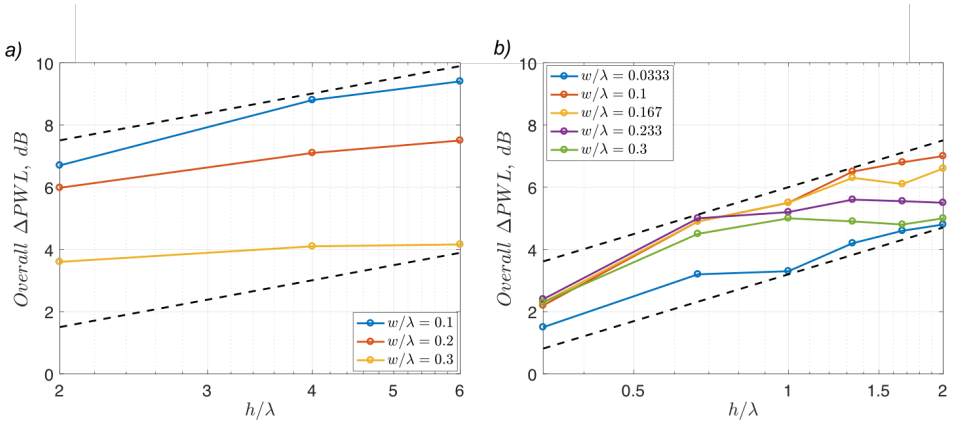

FIGURE 7.4: Overall power reduction against slit length for different slit widths - a) λ =10mm - b) λ =30mm

7.2.2 Variation with slit width

Figure 7.5 a) and b) shows the measured overall power reductions versus normalised slit widths w/λ for two fixed wavelengths λ= 10mm and 30mm, at different slit lengths. As observed in the numerical predictions of Fig. 6.14 an optimum width is observed for which the overall power reduction is a maximum value. As predicted numerically this optimum slit ratio w/λ decreases as the slit length is increased. For the longest and most effective slits the optimum ratio is close to 0.1 but increases towards about 0.15 for smaller slit lengths where the noise reductions are poorer. This is entirely consistent with the numerical predictions which indicate an optimum ratio w/λ ranging from 0.05 for longest slit to 0.15 for the shortest slit. The small discrepancy in optimum ratios between predicted and measurement is likely to be due to the very different velocity spectra of the incoming vortical flows.

It is also noted by comparing the results from Fig. 7.5 a) and b) that noise reductions for two slit geometries of the same optimum ratio $w/ = 0.1$ and longest slit length h=60mm are greatest for the smaller slit wavelength $\lambda = 10mm$ and hence w. It therefore appears that greatest noise reductions are achieved when the optimum ratio is maintained but the slit width is made as small as possible. This behaviour is clearly demonstrated in Fig. 7 of of [3] in which the noise reduction spectra are plotted for similar $w/$ ratio but different slits widths (showing an increasing peak in the noise reduction spectra as the slit width is decreased for ratios w/λ of similar value.)

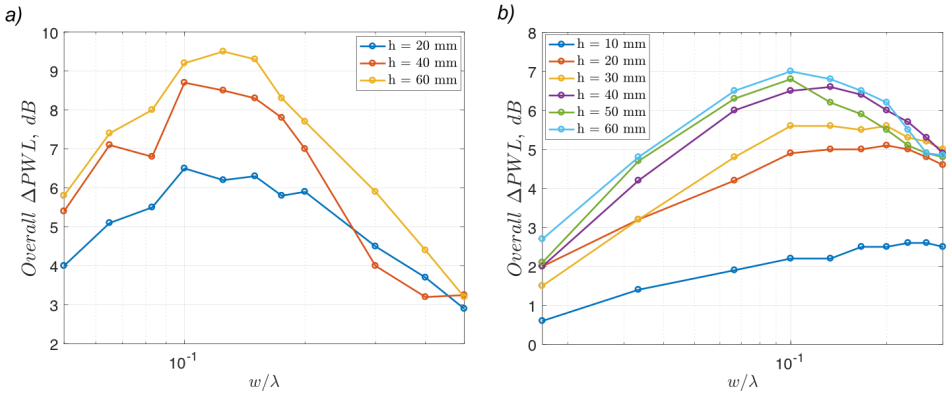

FIGURE 7.5: Overall power reduction against slit width for different slit lengths - a) λ =10mm - b) λ =30mm

7.2.3 Variation with slit wavelength

Figure 7.6 shows the measured overall power reductions for different slit wavelengths λ for a fixed slit length h = 40mm and fixed slit width w = 2mm, plotted against $w\lambda$. Also shown in this figure is the variation of overall power reductions with the slit width at fixed λ = 30mm for the same slit length h = 40mm from Fig. 7.5 b).

Both curves can be observed to have the same optimum ratio w/λ of 0.13, confirming w/λ as an important factor in determining control performance. This figure can be compared directly with Fig. 6.21 showing the same comparison of overall noise reductions obtained numerically,

where a common optimum ratio w/λ is also observed equal to 0.05. It is noted that at this optimum ratio, w and λ were chosen to be identical in the two simulations, while they differ in the measured case and hence produce different overall noise reductions at the optimum ratio w/λ.

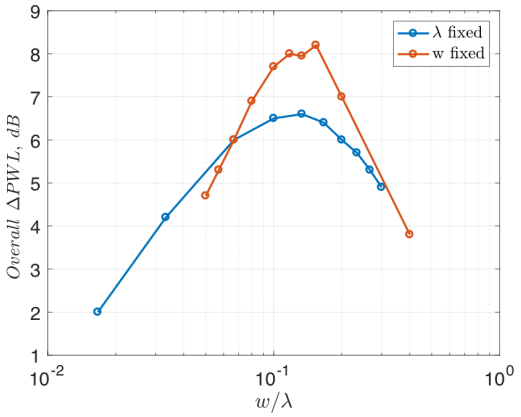

FIGURE 7.6: Overall power reduction against $w\lambda$ for $h/w = 20$ and variation of overall power reductions with the slit width at fixed λ for the same slit length $h = 40$mm from Fig. 7.5 b)

7.2.4 Optimum geometry

By way of a summary of the variation in overall noise reduction with the main geometric slit parameters presented in this investigation, Fig. 7.7 a) and b) show contour plots of the predicted and measured overall power reductions against w/λ and h/λ. Also plotted in Fig. 7.7 b) is the contour plot obtained from the measured overall noise reductions for the slit wavelength $\lambda =$ 10mm. It is noted that Fig. 7.7 is meant only to provide a qualitative comparison between the predicted and measured performance since, not only are the characteristics of the incoming turbulent flow different between prediction and measurement but the range of h/λ was also different. Furthermore, whilst the measurement was made at the absolute value of λ=10mm, no absolute values exist in the simulation since only the non-dimensional quantities of w/λ and h/λ are important in this inviscid calculation.

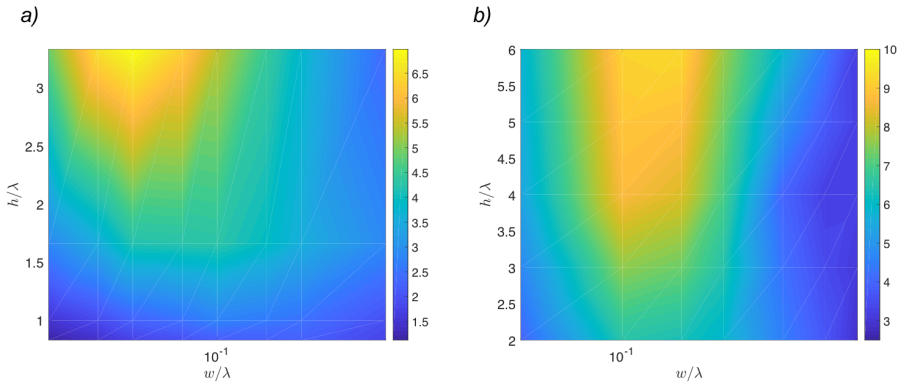

FIGURE 7.7: Contour plots of the overall power reductions against w/λ and h/λ: a) Numerical predictions - b) Experimental measurements for $\lambda = 10$mm

Comparison between the predicted and measured variation in overall noise reductions with w/λ and h/λ show reasonable qualitative agreement given the differences between the two as outlined above. in both cases maximum noise reductions are obtained for $0.05 \leq w/\lambda \leq 0.15$, with noise reduction progressively improving as h is increased.

7.3 Frequency-dependent directivity

In this section the behaviour of the far-field noise reduction directivity as a function of frequency is investigated and compared against predictions. Figure 7.8 shows the directivity of the measured noise reductions at four non-dimensional frequencies of $fh/U = 0.5, 1.5, 2.53.5$. As a means of comparison, Fig. 7.8 also shows the directivities for the predicted noise reductions at those same frequencies, obtained by subtracting the far-field directivities from the baseline and slitted configuration shown in Chapter 5 in Fig. 5.6. Good qualitative agreement between the predicted and measured directivity patterns is obtained. It can be observed that both predicted and measured directivities display optimum angles for which the noise reductions are maximum. In Chapter 5, it has been shown that these optimum angles correspond to the angles θ_n for which the front and back edges radiate with a phase difference equal to an odd multiple of 180°, leading to maximum noise reductions when the sources are of equal strengths ($fh/U = 2n + 1$). An equation for predicting those optimum angles has been derived in Eq. 5.20 which showed that as the frequency fh/U is increased, there is a larger number of optimum angles that co-exist at the same frequency. This behaviour is clearly visible in Fig. 7.8 which displays an identical number of optimum angles for the measured directivities at the same frequencies $fh/U = 2n+1$ as observed in the predicted directivities. This result confirms once again the importance of destructive interference at single frequencies and specific angles.

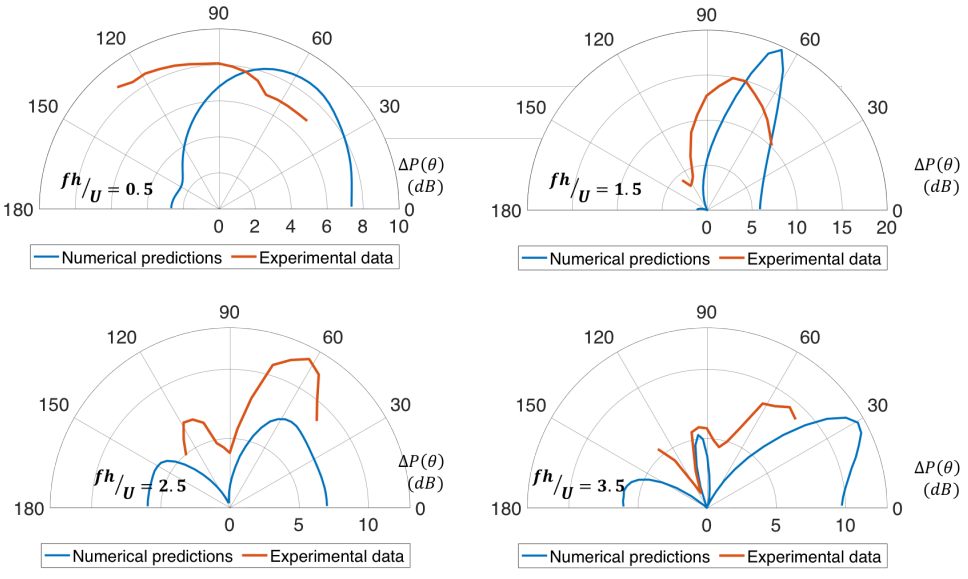

FIGURE 7.8: Far-field directivities of the predicted and measured noise reductions at different non-dimensional frequencies

Chapter 8

Conclusion and future work

8.1 Conclusions

The mechanism and performance of slitted leading edge serrations for reducing turbulence - aerofoil interaction noise has been investigated in detail from numerical solutions of the Euler equations. These predictions have confirmed the hypothesis of Chaitanya et al [4] that the essential noise reduction mechanisms are related to an overall reduction in source strength and through the interference between two sources at either ends of the slit. This thesis has shown that the initial prescribed vortex impinging on the plate generates two acoustic sources at either end of the slits, whose levels are affected by secondary streamwise vortices originated at the slit corners and interacting with the front and back-edges of the slit.

The simple two-source model proposed by Chaitanya et al [4] for the sound power reductions has been extended to include predictions of the pressure directivity. Reasonable agreement between this simple model and the exact calculations have been obtained. The existence of optimum observer angles at each frequency has been identified at which maximum noise reductions are observed. Overall noise reductions integrated over all frequencies has been shown to be related to the degree of anti-correlation between the front and back edge of the slit. This thesis has confirmed that leading edge slits are a promising technology for reducing broadband interaction noise that requires a much smaller modification to the leading edge than conventional serrations in terms of the aerofoil area modification. However, their relative effects on aerodynamic performance and structural integrity remain to be determined.

The experimental study by Chaitanya et al and the present numerical study into the performance and mechanisms of leading edge slits for the reduction of broadband aerofoil interaction noise has also been expanded. The main conclusions from this investigation may be summarised as follows:

1. Overall noise reductions are shown to be a strong function of the slit geometrical parameters of slit length h, width w and wavelength λ.

2. Overall noise reductions are found to be mostly governed by the reduction in source strength on the surface of the flat-plate, with the influence of destructive interference between the two sources limited to a maximum of about 1dB. However, destructive interference has a large impact on the reductions at specific frequencies close to $fh/U = 2n + 1$, where variations of up to 7dB have been observed depending on the slit configurations.

3. Consistent with the experimental work of Chaitanya et al, noise reductions improve as h is increased. In this thesis it is shown that overall noise reductions increase with h as $h^{1/2}$ as an upper limit, with slower variations being observed for increasing w/λ.

4. For a give slit geometry, increasing the slit width has the opposite effect on noise reductions compared to increasing the slit wavelength (Fig. 6.21)

5. The existence of an optimum ratio w/λ of maximum overall noise reductions identified experimentally by Chaitanya et al has been verified through numerical calculations. The optimum ratio w/λ of around 0.12 obtained experimentally for a fixed h is within the range of $0.05 \leq w/\lambda \leq 0.15$ obtained in this thesis both numerically and experimentally.

6. In most slit geometries considered in this thesis the overall source strength at the back of the slit exceeds that at the front (see Fig. 6.15). The optimum ratio w/λ is therefore strongly related to the ratio at which the source at the back edge is a minimum, which has been shown to be directly linked to the interaction of adjacent secondary vortices.

7. Finally, it is noted that following Chaitanya et al, noise reductions generally improve as w is reduced whilst maintaining the optimum ratio w/λ.

In conclusion, therefore, this thesis has confirmed the use of very narrow slits as a high effective strategy for reducing broadband aerofoil - turbulence interaction noise.

8.1.1 Future work

Whilst the effectiveness of this technology has been established, further work is needed to determine its effect on aerodynamic performance. The recommendations are listed below:

1. To extend the conclusions to realistic aerofoils and include the effect of angle of attacks: with a realistic aerofoil, the flow will be forced through the gap from pressure side to suction side due to the mean loading. Additional work is needed to understand the effect of the additional noise source created when the fluctuating pressure is superimposed on a mean pressure.

2. To include viscous effects by the use of LES simulations to understand how the boundary layer affects the secondary vortex generation, particularly at the back-edge of the slit where the boundary layer has grown and might dampen the secondary vortex system.

3. To determine the aerodynamic penalty associated with LE slits by investigating the effect of slitted leading edges on the lift and the drag. More work is needed to come to a conclusion concerning the necessary balance between aerodynamic penalties and noise reduction.

References

[1] R.J. Astley, A. Agarwal, K.R. Holland, P.F. Joseph, R.H. Self, M.G. Smith, R. Sugimoto, and B.J. Tester. Predicting and reducing aircraft noise. *14th International Congress Sound & Vibration, Australia*, 792, 2007.

[2] P. Chaitanya. *Aerofoil geometry effects on turbulence interaction noise*. PhD Thesis, University of Southampton, UK, 2017.

[3] P. Chaitanya, P. Joseph, and L.J. Ayton. Leading-edge profiles for the reduction of airfoil interaction noise. *AIAA Journal*, 58, 2020.

[4] P. Chaitanya and P. Joseph. Slitted leading edge profiles for the reduction of turbulence-aerofoil interaction noise. *The Journal of the Acoustical Society of America*, 123, 2017.

[5] ICAO. *Air Navigation Report*. 2016 Edition.

[6] T. von Karman and W.R. Sears. Airfoil theory for non-uniform motion. *Journal of the Aeronautical Sciences*, 5(10):p. 379–390, 1938.

[7] W.R. Sears. Some aspects of non-stationary airfoil theory and its practical applications. *Journal of the Aeronautical Sciences*, 8:p. 104–108, 1941.

[8] R. Paterson and R. Amiet. Acoustic radiation and surface pressure characteristics of an airfoil due to incident turbulence. *NASA Contractor Report 2733*, 1976.

[9] J.J. Adamczyk. The passage of an infinite swept airfoil through an oblique gust. *NASA Contractor Report 2395*, 1974.

[10] R. K. Amiet. Acoustic radiation from an airfoil in turbulent stream. *Journal of Sound and Vibration*, 41(4):p. 407–420, 1975.

[11] N. Curle. *The influence of solid boundaries upon aerodynamic sound*. Springer, 1955.

[12] K. Kucukcoskun, J. Christophe, C. Schram, and M. Tournour. Broadband scattering of the turbulence-interaction noise of a stationary airfoil: Experimental validation of a semi-analytical model. *International Journal of Aeroacoustics*, 12:83–102, 2013.

[13] S. Moreau, M. Roger, and V. Jurdic. Effect of angle of attack and airfoil shape on turbulence interaction noise. *Proceedings of the 11th AIAA/CEAS Aeroacoustics Conference, Monterey, California*, pages AIAA–2005–2973, 2005.

[14] L. Santana, C. Schram, and W. Desmet. Low-frequency extension of amiets theory for compact airfoil noise predictions. *Journal of Sound and Vibration*, 372, 2016.

[15] M.E. Goldstein. Unsteady vortical and entropic distortions of potential flows round arbitrary obstacles. *Journal of Fluid Mechanics*, 89:433–468, 1978.

[16] S. Glegg. Broadband noise from ducted prop fans. *15th AIAA Aeroacoustics Conference*, pages AIAA 1993–4402, 1993.

[17] H. Atassi and G. Hamad. Sound generated in a cascade by three-dimensional disturbances convected in a subsonic flow. *7th AIAA Aeroacoustics Conference*, pages AIAA 1981–2046, 1981.

[18] S. Kaji and T. Okazaki. Generation of sound by rotor-stator interaction. *Journal of Sound and Vibration*, 13:281–307, 1970.

[19] F. Lane and M. Friedman. Unsteady aerodynamics of vortical flows: Early and recent developments. *Technical Report - NACA-TN-4136*, 1958.

[20] D. Whitehead. Vibration and sound generation in a cascade of flat plates in subsonic flow. *Aeronautical Research Council Reports and Memoranda*, 3685, 1972.

[21] D. Whitehead. Chapter "classical two-dimensional methods". *AGARD Manual on Aeroelasticity in Axial-Flow Turbomachines Volume 1 Unsteady Turbomachinery Aerodynamics*, pages 3.1–3.30, 1987.

[22] S. Smith. Discrete frequency sound generation in axial flow turbomachines. *Aeronautical Research Council Reports and Memoranda*, 3709, 1972.

[23] C. Cheong, P. Joseph, and S. Lee. High frequency formulation for the acoustic power spectrum due to cascade-turbulence interaction. *Journal of the Acoustic Society of America*, 119:108–122, 2006.

[24] R. Mani and G. Horvay. Sound transmission through blade rows. *Journal of Sound and Vibration*, 12:59–83, 1970.

[25] W. Koch. On the transmission of sound waves through a blade row. *Journal of Sound and Vibration*, 18:111–128, 1971.

[26] N. Peake. The interaction between a high-frequency gust and a blade row. *Journal of Fluid Mechanics*, 241:261–289, 1992.

[27] S. Glegg. The response of a swept blade row to a three-dimensional gust. *Journal of Sound and Vibration*, 227:29–64, 1999.

[28] D.B. Hanson and K.P. Horan. Turbulence/cascade interaction: spectra of inflow, cascade response and noise. *Proceedings of the 4th AIAA/CEAS Aeroacoustics Conference*, AIAA-98-2319, 1998.

[29] N. Peake and E. Kerschen. Influence of mean loading on noise generated by the interaction of gust with plate cascade: upstream radiation. *Journal of Fluid mechanics*, 347:315–346, 1997.

[30] I. Evers and N. Peake. On sound generation by the interaction between turbulence and a cascade of airfoils with non-uniform mean flow. *Journal of Fluid mechanics*, 463:25–52, 2022.

[31] T. Colonius and S.K. Lele. Comupational aeroacoustics: Progress on nonlinear problems of sound generation. *Progress in Aerospace Sciences*, 40:p. 345–416, 2008.

[32] R.D. Sandberg and N.D. Sandham. Direct numerical simulation of turbulent flow past a trailing edge and the associated noise generation. *J. Fluid Mech.*, 596:p. 353–385, 2008.

[33] M. Roger and S. Moreau. Extensions and limitations of analytical airfoil broad- band noise models. *International Journal of Aeroacoustics*, 9:p. 273–306, 2010.

[34] M. Billson, L.E. Eriksson, and L. Davidson. Jet noise prediction using stochas- tic turbulence modelling. *9th AIAA/CEAS Aeroacoustics Conference, No. 3282, Hilton Head, South California*, 2003.

[35] J. Scott. Single airfoil gust response problem, category 3, problem 1. *Fourth computational aeroacoustics, workshop on benchmark problems*, NASA CP-2004- 212954:p. 45–58, 2004.

[36] J. Scott and H. Atassi. Numerical solution of periodic vortical flows about a thin airfoil. *24th AIAA Thermophysics Conference*, pages AIAA 89–1691, 1989.

[37] H. Atassi, S. Subramaniam, and J. Scott. Acoustic radiation from lifting airfoils in compressible subsonic flows. *13th AIAA Aeroacoustic Conference*, pages AIAA 90–3911, 1990.

[38] D. Lockard and P. Morris. A parallel implementation of a computational aeroa- coustic algorith for airfoil noise. *2nd AIAA/CEAS Aeroacoustics Conference*, pages AIAA–96–1754, 1996.

[39] D. Lockard and P. Morris. Radiated noise from airfoils in realistic mean flows. *AIAA Journal*, 36(6):p. 907–914, 1998.

[40] R. Hixon, J. Scott, S. Sawyer, and M. Nalasamy. Application of a nonlinear computational aeroacoustics code to the gust-airfoil problem. *AIAA Journal*, 44(2):p. 323– 328, 2006.

[41] V. Golubev, R. Mankbadi, and J. Scott. Numerical inviscid analysis of nonlinear airfoil response to impinging high-intensity high-frequency gust. *10th AIAA/CEAS Aeroacoustics Conference*, pages AIAA 2004–3002, 2004.

[42] V. Golubev, R. Mankbadi, M. Visbal, J. Scott, and R. Hixon. A parametric study of nonlinear gust-airfoil interaction. *10th AIAA/CEAS Aeroacoustics Conference*, pages AIAA 2006–2426, 2006.

[43] R. Kraichnan. Diffusion by a random velocity field. *Physics of Fluids*, 13(1):p. 22–31, 1970.

[44] M. Karweit, P. Blanc-Benon, D. Juve, and G. Comte-Bellot. Simulation of the propagation of an acoustic wave through a turbulent velocity field: a study of phase variance. *Journal of the Acoustical Society of America*, 89(1):p. 52–62, 1991.

[45] C. Bailly and D. Juve. A stochastic approach to compute subsonic noise using linearized euler's equations. *5th AIAA/CEAS Aeroacoustics Conference*, pages AIAA 99–1872, 1999.

[46] M. Billson, L. Eriksson, and L. Davidson. Jet noise prediction using stochastic turbulence modeling. *9th AIAA/CEAS Aeroacoustics Conference*, pages AIAA 2003–3282, 2003.

[47] M. Billson, L. Eriksson, L. Davidson, and P. Jordan. Modeling of synthetic anisotropic turbulence and its sound emission. *10th AIAA/CEAS Aeroacoustics Conference, Manchester, England*, pages AIAA 2004–2858, 2004.

[48] V. Clair. *Calcul numerique de la reponse acoustique d'un aubage soumis a un sillage turbulent*. PhD Thesis, Universite Claude Bernard, Lyon 1, France, 2013.

[49] J.R. Gill. *Broadband Noise Generation of a Contra-Rotating Open Rotor Blade*. PhD Thesis, Univeristy of Southampton, UK, 2015.

[50] N. Jarrin, S. Benhamadouche, D. Laurence, and R. Prosser. A synthetic-eddy method for generating inflow conditions for large-eddy simualtions. *International Journal of Heat and Fluid Flow*, 27:p. 585–593, 2006.

[51] A. Sescu and R. Hixon. Toward low-noise synthetic turbulent inflow conditions for aeroacoustic calculations. *International Journal of Numerical Methods in Fluids*, 73:p. 1001–1010, 2013.

[52] J. W. Kim and S. Haeri. An advanced synthetic eddy method for the computation of aerofoil-turbulence interaction noise. *International Journal of Numerical Methods in Fluids*, 287:p. 1–17, 2015.

[53] R. Ewert and W. Schroder. Acoustic perturbation equations based on flow decomposition via source filtering. *J. Comput. Phys.*, 188:p. 365–398, 2003.

[54] M. Dieste and G. Gabard. Broadband fan interaction noise using synthetic inhomogeneous non-stationary turbulence. *17th AIAA/CEAS Aeroacoustics Conference*, pages AIAA 2009–3267, 2011.

[55] M. Dieste and G. Gabard. Random particle methods applied to broadband fan interaction noise. *Journal of Computational Physics*, 231:p. 8133–8151, 2012.

[56] F. Gea-Aguilera, X. Zhang, X. Chen, , and J. Gill. Synthetic turbulence methods for leading edge noise predictions. *21st AIAA/CEAS Aeroacoustics Conference Dallas, TX*, 2015.

[57] V. Golubev and H.M. Atassi. Unsteady swirling flows in annular cascades, part 1: Evolution of incident disturbances. *AIAA Journal*, 38:1142–1149, 2000.

[58] V. Golubev and H.M. Atassi. Unsteady swirling flows in annular cascades, part 2: Aerodynamic blade response. *AIAA Journal*, 38:1150–1158, 2000.

[59] R. Hixon, A. Sescu, M. Nallasamy, and S. Sawyer. Prediction of noise from realistic rotor-wake/stator-row interaction using caa. *15th AIAA/CEAS Aeroacoustics Conference*, AIAA-2009-3339, 2009.

[60] C. Polacsek, V. Clair, T. Le Garrec, G. Reboul, and M.C. Jacob. Numerical predictions of turbulence/cascade-interaction noise using computational aeroacoustics with stochastic model. *AIAA Journal*, 53:3551–3566, 2015.

[61] Y. Rozenberg. *Modelisation analytique du bruit aerodynamique a large bande des machines tournantes : utilisation de calculs moyennes de mecanique des fluides*. PhD Thesis, Ecole Centrale de Lyon, Lyon, France, 2012.

[62] S. Oerlemans and P .Migliore. Aeroacoustic wind tunnel tests of wind turbine airfoils. *Proceedings of the 10th AIAA/CEAS Aeroacoustics Conference, Manchester, UK*, pages AIAA–2004–3042, 2004.

[63] W. Olsen and J. Wagner. Effect of thickness on airfoil surface noise. *AIAA Journal*, page p. 437–439, 1982.

[64] J. Devenport, J. K. Staubs, and S. A. L. Glegg. Sound radiation from real airfoils in turbulence. *Journal of Sound and Vibration*, 329:p. 437–439, 2010.

[65] A. M. Hall, O. V. Atassi, and J. Gilson. Effects of leading-edge thickness on high-speed airfoil-turbulence interaction noise. *17th AIAA/CEAS Aeroacoustics Conference, Portland, Oregon*, pages AAIA 2011–2861, 2011.

[66] J. Gershfeld. Leading edge noise from thick foils in turbulent flows. *Journal of acoustical society of America*, 116:p. 1416–1426, 2004.

[67] Peter D. Lysak, Dean E. Capone, and Michael L. Jonson. Prediction of high frequency gust response with airofoil thickness effects. *Journal of Fluids and Structures*, 39:p. 258–274, 2013.

[68] P.J. Moriarty, G. Guidati, and P. Migliore. Prediction of turbulent inflow and trailing-edge noise for wind turbines. *11th AIAA/CEAS Aeroacoustics Conference*, 2005.

[69] T. Hainaut, G. Gabard, and V. Clair. A caa study of turbulence distorsion in broadband fan interaction noise. *22nd AIAA/CEAS Aeroacoustics Conference, Manchester*, AIAA 2016-2839, 2016.

[70] L.J. Hayton. An analytic solution for gust-aerofoil interaction noise including effects of geometry. *IMA Journal of Applied Mathematics*, 82:280–304, 2016.

[71] P.T. Soderman. Aerodynamic effects of leading-edge serrations on a two-dimensional airfoil. *Technical Report - NASA TM X-2643*, 1972.

[72] A. Skillen, A. Revell, A. Pinelli, U. Piomelli, and J. Favier. Flow over a wing with leading-edge undulations. *AIAA Journal*, 53:464–472, 2015.

[73] M.M. Zhang, G.F. Wang, and J.Z. Xu. Aerodynamic control of low-reylnolds-number airfoil with leading-edge protuberances. *AIAA Journal*, 51:1960–1971, 2013.

[74] D.S. Miklosovic, M.M. Murray, L.E. Howle, and F.E. Fish. Leading-edge tubercles delay stall on humpback whale (megaptera novaeangliae) flippers. *Physics of Fluids*, 16, 2004.

[75] H. Johari, C. Henoch, D. Custodio, and A. Levshin. Effects of leading-edge protuberances on airfoil performance. *AIAA Journal*, 45:2634–2642, 2007.

[76] J. Favier, A. Pinelli, and U. Piomelli. Control of the separated flow around an airfoil using a wavy leading edge inspired by humpback whale flippers. *Comptes Rendus Mecanique*, 340:107–114, 2012.

[77] K. Hansen, R. Kelso, and B. Dally. Performance variations of leading-edges tubercles for distinct airfoil profiles. *AIAA Journal*, 49:185–194, 2011.

[78] T.P. Chong, A. Vathylakis, A. McEwen, F. Kemsley, C. Muhammad, and S. Siddiqi. Aeroacoustic and aerodynamic performance of an airfoil subjected to sinusoidal leading edges. *21th AIAA/CEAS Aeroacoustics Conference*, AIAA-2015-2200, 2015.

[79] M. Roger, C. Schram, and L. De Santana. Reduction of airfoil turbulence-impingement noise by means of leading-edge serrations and/or porous material. *19th AIAA/CEAS Aeroacoustics Conference*, AIAA 2013-2108, 2013.

[80] V. Clair, C. Polacsek, T. Le Garrec, G. Reboul, M. Gruber, and P. Joseph. Experimental and numerical investigation of turbulence-airfoil noise reduction using wavy edges. *AIAA Journal*, 51:2695–2713, 2013.

[81] A.S.H. Lau, S. Haeri, and J.W. Kim. The effect of wavy leading edges on aerofoil–gust interaction noise. *Journal of Sound and Vibration*, 332:6234–6253, 2013.

[82] S. Narayanan, P. Chaitanya, S. Haeri, P. Joseph, J.W. Kim, and C. Polacsek. Airfoil noise reductions through leading edge serrations. *Physics of Fluid*, 27(025109):AIAA 2015–2202, 2015.

[83] J.W. Kim, S. Haeri, and P.F. Joseph. On the reduction of aerofoil-turbulenceinteraction noise associated with wavy leading edges. *Journal of Fluid Mechanics*, 792:p. 26–552, 2016.

[84] P. Chaitanya, S. Narayanan, P. Joseph, C. Vanderwel, J. Turner, J.W. Kim, and B. Ganapathisubramani. Broadband noise reduction through leading edge serrations on realistic aerofoils. *21st AIAA/CEAS Aeroacoustics Conference*, pages AIAA 2015–2202, 2015.

[85] B. Lyu, M. Azarpeyvand, and S. Sinayoko. Noise prediction for serrated leading-edges. *22nd AIAA/CEAS Aeroacoustics Conference*, AIAA-2016-2740, 2016.

[86] P. Chaitanya, S. Narayanan, P. Joseph, and J. W. Kim. Leading edge serration geometries for significantly enhanced leading edge noise reductions. *American Institute of Aeronautics and Astronautics*, pages AIAA 2016–2736, 2016.

[87] J. Turner, J.W. Kim, P. Chaitanya, and P. Joseph. Towards understanding aerofoils with dual-frequency wavy leading edges interacting with vortical disturbances. *22nd AIAA/CEAS Aeroacoustics Conference*, AIAA-2016-2951, 2016.

[88] J.M. Turner and J.W. Kim. Aeroacoustic source mechanisms of a wavy leading edge undergoing vortical disturbances. *Journal of Fluid Mechanics*, 811:p. 582–611, 2017.

[89] T.P. Chong, T. Biedermann, O. Koster, and SM. Hasheminejad. On the effect of leading edge serrations on aerofoil noise production. *19th AIAA/CEAS Aeroacoustics Conference*, AIAA 2018-3289, 2018.

[90] J.W. Kim, S. Haeri, and P.F. Joseph. On the mechanisms of noise reduction in aerofoil-turbulence interaction by using wavy leading edges. *21st AIAA/CEAS Aeroacoustics Conference*, pages AIAA 2015–3269, 2015.

[91] V. Clair, C. Polacsek, G. Reboul, and T. Le Garrec. Numerical simulation of turbulence interaction noise applied to a serrated airfoil. *Proceedings of the Acoustics 2012 Nantes Conference*, pages p. 3763–3768, 2012.

[92] F. Gea-Aguilera, J. Gill, and D. Angland. Wavy leading edge airfoils interacting with anisotropic turbulence. *23rd AIAA/CEAS Aeroacoustics Conference*, pages AIAA 2017–3370, 2017.

[93] M.R. Visbal and D.V. Gaitonde. On the use of higher-order finite-difference schemes on curvilinear and deforming meshes. *Journal of Computational Physics*, 181:p. 155–185, 2002.

[94] T. Baker. Mesh generation: art or science? *Prog. Aerosp. Sci.*, 41(1):p. 29–63, 2005.

[95] J.W. Kim. Optimised boundary compact finite difference schemes for computational aeroacoustics. *Journal of Computational Physics*, 225:p. 995–1019, 2007.

[96] J.W. Kim. High-order compact filters with variable cut-off wavenumber and stable boundary treatment. *Computers and Fluids*, 39:p. 1168–1182, 2010.

[97] Christopher K.W. TAM. *Computational aeroacoustics - A wave number approach.* Cambridge University Press, 2012.

[98] J.W. Kim. Quasi-disjoint pentadiagonal matrix systems for the parallelization of compact finite-difference schemes and filters. *Journal of Computational Physics*, 241:p. 168–194, 2013.

[99] J.W. Kim and D.J. Lee. Generalised characteristic boundary conditions for computational aeroacoustics. *AIAA Journal*, 38:p. 2040–2049, 2000.

[100] J.W. Kim and D.J. Lee. Generalized characteristic boundary conditions for computational aeroacoustics, part 2. *AIAA Journal*, 42:p. 47–55, 2004.

[101] J.W. Kim, A.S.H. Lau, and N.D. Sandham. Proposed boundary conditions for gust-airfoil interaction noise. *AIAA Journal*, 39:p. 2705–2709, 2010.

[102] V.P. Blandeau, P. Joseph, G. Jenkins, and C. J. Powles. Comparison of sound power radiation from isolated airfoils and cascades in a turbulent flow. *The Journal of the Acoustical Society of America*, 129(6):p. 3521–3530, 2011.

[103] G. Reboul. *Modélisation du bruit à large bande de soufflante de turboréacteur.* PhD Thesis, Ecole Centrale de Lyon, France, 2017.

[104] Jae Wook Kim. An advanced synthetic eddy method for the computation of aerofoil turbulence interaction noise. *Journal of Computational Physics*, 287:1–17, 2015.

[105] Jae Wook Kim, S. Haeri, and P. Joseph. On the reduction of aerofoil-turbulence interaction noise associated with wavy leading edges. *Journal of Fluid Mechanics*, 792:526–552, 2016.

[106] M. Cannard, P. Joseph, J.W. Kim, and P. Chaitanya. Numerical investigation into slitted leading-edge profiles for reducing interaction noise. *25th International Congress on Sound and Vibration 2018, Hiroshima, Japan*, 3:1366–1373, 2018.

[107] T.P. Chong, P. Joseph, and P.O.A.L. Davies. A parametric study of passive flow control for a short, high area ratio 90 deg curved diffuser. *Journal of Fluids Engineering*, 130, 2008.